A Study of Eta Photoproduction on the Proton at MAMI

Joseph Mancell

A thesis presented for the degree of
Doctor of Philosophy

Nuclear Physics Group
School of Physics and Astronomy
University of Glasgow

April 2012

A Study of Eta Photoproduction on the Proton at MAMI

Joseph Mancell

Submitted for the degree of Doctor of Philosophy

April 2012

Abstract

In recent years, there has been much interest in the possible existence of the N*(1685) narrow nucleon resonance, as predicted by the chiral soliton model. Several η photoproduction experiments have been performed that rely on extracting neutron observables from deuteron target data. These have shown some evidence of narrow structure, however, no structure was observed in cross section measurements on the proton channel. Within the A2 collaboration at the MAMI accelerator in Mainz, Germany, a more detailed study has been undertaken using η photoproduction on a liquid H_2 target, and is the subject for this thesis. The study utilised the high resolution and high precision possible with the A2 detector setup, in an attempt to overcome the predicted low photocoupling between the N*(1685) and the proton.

The MAMI electron beam was used to produce bremsstrahlung photons, the energies of which are determined by detecting the recoil electrons in the Glasgow-Mainz Tagged Photon Spectrometer. The reaction products from the interaction of the photon beam and liquid H_2 were detected by the Crystal Ball and TAPS calorimeters. The $\gamma p \rightarrow \eta p$ reaction channel was identified via the $\eta \rightarrow 3\pi^0 \rightarrow 6\gamma$ decay branch. The reaction cross section was measured between $E_\gamma = 707$ and 1477 MeV. Both differential and total cross sections have been presented with a particular em-

phasis on the centre of mass energy range around 1685 MeV. The peak structure seen on the neutron channel is not observed in the case of the proton. However, a dip in the cross section is observed, which is more prominent at forward polar angles. The leading models are not fully able to reproduce the data in this energy region. As such, given the high energy resolution of the measurement the results can be used to constrain future models and in doing so aid the understanding of the nucleon's resonance spectrum.

Declaration

The work in this thesis is based on research carried out at the Nuclear Physics Group, School of Physics & Astronomy, University of Glasgow, UK. No part of this thesis has been submitted elsewhere for any other degree or qualification and it all my own work unless referenced to the contrary in the text.

Contents

List of Figures

List of Tables

Chapter 1

Introduction

1.1 Hadrons

The atomic nucleus is composed of protons and neutrons, which are the two most common hadrons and are held together by the strong force. Hadrons account for the majority of known mass in the universe, and their study provides an excellent means to investigate the fundamental nature of matter. The field of hadron physics is primarily concerned with understanding protons and neutrons, which are collectively known as nucleons. This can be done by directly accessing the sub-nucleonic degrees of freedom at high energies or by studying the nucleon's resonance spectrum at lower energies.

An early theory to describe the strong force was proposed by Yukawa in 1935 [1]. He stated that a field caused the attraction between nucleons and that this field should have an exchange particle to act as a mediator, as the photon does for the electromagnetic field. However, it was not until 1947 with the conclusive discovery of the π meson (pion) [2] that a particle was found which fitted Yukawa's predictions. Eventually three variations of pion were discovered: π^+, π^0 and π^-. Over the next three decades experimental physicists reported the discovery of many more particles including the η, ρ and ω mesons and heavier baryons such as the Σ, Λ and Ξ. Some of these particles exhibited "strange" behaviour in the manner in which they

were created and decayed. These particles gave rise to a new property known as strangeness, the value of which is conserved in strong interactions.

In 1961 a classification scheme for particles named the "Eightfold Way" was proposed by Murray Gell-Mann, whilst a similar scheme was independently suggested by Ne'eman [3]. The scheme arranged the baryons and mesons into multiplets based on their quantum numbers. A diagram of the meson octet, the baryon octet and the baryon decuplet is shown in figure 1.1. The horizontal lines group together particles of the same strangeness whilst the particles on the same top left to bottom right diagonal have identical charge. The bottom particle on the baryon decuplet, the Ω^-, had yet to be detected, though its mass and lifetime were predicted by Gell-Mann. So when the Ω^- was discovered [4] and the quantum numbers matched the prediction, the Eightfold Way was shown to be an important milestone in the development of hadron physics.

1.2 Quantum ChromoDynamics

The Eightfold Way gave an organisational structure to the classification of hadrons but it did not explain the underlying physics of the arrangement. An explanation was proposed independently by both Gell-Mann and Zweig in 1964. They suggested that hadrons were not elementary particles but in fact comprised of more fundamental particles named quarks. Initially it was proposed that three flavours of quark exist: up, down and strange, the properties of which are given in table 1.1. Each quark has an associated antiparticle partner with opposite quantum numbers. The quark model stated that baryons are comprised of three quarks, antibaryons three antiquarks and that mesons are comprised of a quark and an antiquark pair. The isospin of hadrons, a concept originally devised to account for the similarities between the proton and neutron, was now understood to originate from the up and down quark content.

However, the introduction of quarks posed a new problem: the quark arrangements needed to form several of the baryons, such as the Δ^{++} and the Ω^-, were in violation

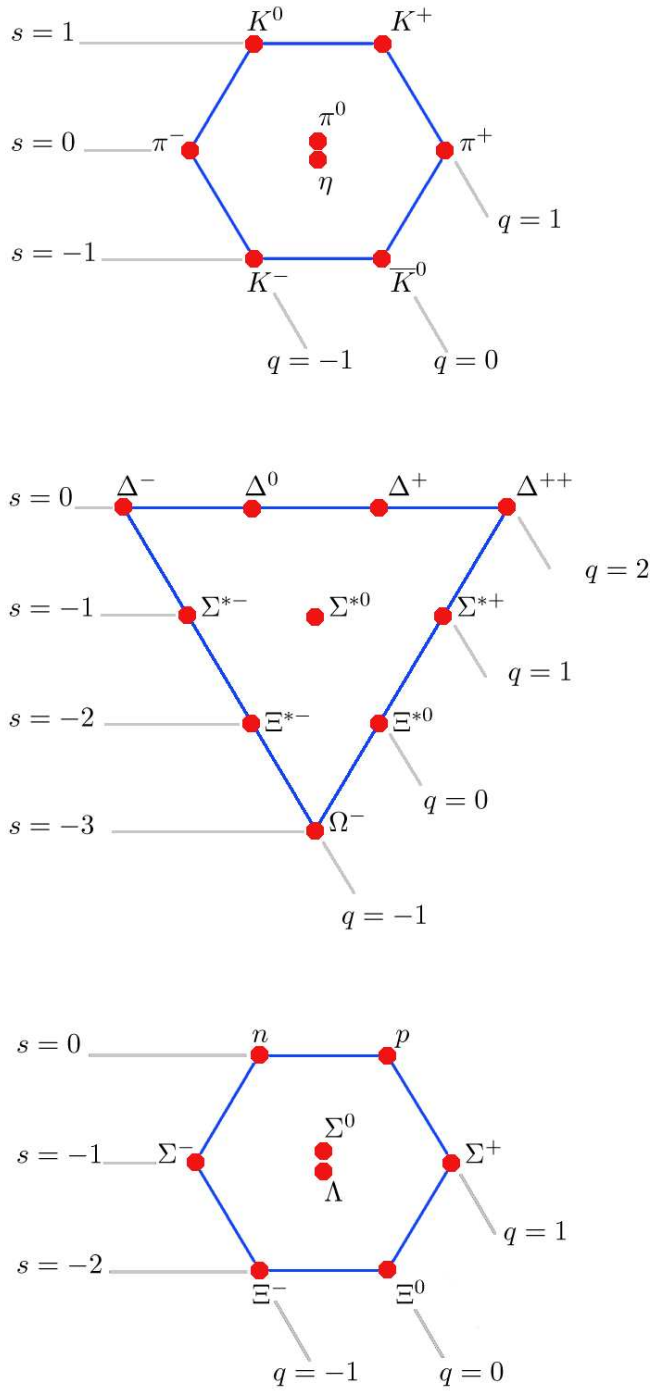

Figure 1.1: Diagram of the Eightfold Way hadron organisational scheme. Horizontal lines represent particles of like strangeness and to left to bottom right diagonals represent like charge. Top: meson octet. Middle: baryon decuplet. Bottom: baryon octet.

flavour	Q	B	I	I_3	S
up	+2/3	1/3	1/2	+1/2	0
down	-1/3	1/3	1/2	-1/2	0
strange	-1/3	1/3	0	0	-1

Table 1.1: Table of quark properties showing charge (Q), baryon number (B), strangeness (S), isospin (I) and isospin projection (I_3)

of the Pauli exclusion principle. This inferred that fermions with identical quantum numbers cannot occupy the same state. A solution was proposed by Greenberg in 1964 [5] who introduced a new quantum number, later termed "colour". There are three types of colour charge, red, blue and green. Antiquarks have anticolour quantum numbers. All hadrons are colour neutral, which means that for mesons the colour charge must be balanced out by the relevant anticolour and that for baryons and antibaryons all three colours or anticolours must be present.

The quark model was further developed into what is now known as Quantum ChromoDynamics (QCD). QCD is a gauge field theory which describes the interactions between quarks where gluons are the mediator exchange particle of the colour charge field. There are eight types of gluon which carry various combinations of colour charge, so unlike the photon in the electromagnetic field which is neutral, the gluon is self-interacting. The strength of the interaction between quarks and gluons is known as the coupling constant (α_s). In QCD, this coupling constant is not in fact constant but varies with the energy of the system. When experimentalists study quarks and gluons inside hadrons using a high energy probe with a large associated momentum transfer, the strength of the coupling is small. This feature, which is responsible for the force between quarks decreasing as the distance between them decreases, is known as asymptotic freedom and was discovered in 1974 [6,7]. However, at larger distances and lower energies such as those associated with the quarks inside the nucleon, the strength of the coupling is large. As the quarks move further apart the binding between them increases, eventually leading to a new quark-antiquark pair being formed. It is therefore not possible for a single unbound quark to exist,

leading to another basic concept of QCD: quark confinement. Although QCD fully describes the interactions between quarks and gluons, an exact solution is not possible. In the high energy regime it is possible to make calculations using perturbation theory. This is because the value of the coupling constant in this regime is much less than one, meaning that the resulting perturbative expansion will converge and is therefore solvable.

In the low energy regime when the coupling constant is large the expansion diverges and a calculation of this type is not possible. In order to describe interactions within the nucleon, which lies in this low energy regime, it is necessary to develop quark models and effective field theories that are based on the symmetries and conservation rules of QCD. One such model is chiral perturbation theory [8], in which the quarks are initially considered to be massless and the quark field is split into two parallel and anti-parallel quark helicity states. Since the quarks are massless their helicity states are strictly conserved. However, when the quarks acquire mass the chiral symmetry is spontaneously broken, leading to a low energy description of QCD based on the resultant effective pion field. An alternative low energy approach is that of constituent quark models in which the effective degrees of freedom of QCD are modelled by three heavier (approximately 200-300 MeV/c^2) quarks interacting in an effective potential. For a summary of quark models see reference [9].

A key factor in the advancement of these models is the experimental study of nucleon and baryon resonances via the measurement of their properties, such as mass, width, production and decay modes, spin and parities. One experimental program to access this information involves the photoproduction of mesons from a nucleon target via the intermediate excitation of one or more baryon resonances.

1.3 Scattering Theory

The scattering of an incident beam of particles from an object of interest in order to investigate the properties of the object is a fundamental technique in experimental physics. This section introduces the basic formalism of such scattering processes,

cross sections and the concept of partial waves. The cross section for a scattering process between two particles is a measure of the probability of interaction. An enhancement in the cross section is an indication of an intermediate resonant state. The angular and energy dependence of the cross section can give an indication of the spin, parity and energy of the particles involved. The differential cross section $\frac{d\sigma}{d\Omega}$, shown in equation 1.1 is the ratio between the number of scattered particles dS detected in a given solid angle $d\Omega$ and the product of the incoming flux J and number of scattering centres n.

$$\frac{d\sigma}{d\Omega} = \frac{dS/d\Omega}{Jn} \tag{1.1}$$

The differential cross section can also be described as the square of the scattering amplitude, which is measured in units of length and describes the characteristics of the scattering interaction as a function of the polar angle of the scattered particle.

$$\frac{d\sigma}{d\Omega} = \mid f(\theta) \mid^2 \tag{1.2}$$

The total cross section can be calculated by integrating the differential cross section over all angles.

$$\sigma = \int_0^{2\pi} \int_0^{\pi} \mid f(\theta) \mid^2 \sin(\theta) d\theta d\phi \tag{1.3}$$

1.3.1 Partial Waves

Figure 1.2 shows a basic scattering setup: the incoming particle is treated as a plane wave approaching in the z-direction and the scattered particle is treated as a spherical wave. If the scattering centre is spherically symmetric then angular momentum is conserved. The total wave function at the detector, which is considered to be far from the scattering centre, is given by equation 1.4.

$$\psi(r, \theta, \phi) = e^{ikrcos\theta} + f(\theta, \phi)\frac{e^{ikr}}{r} \tag{1.4}$$

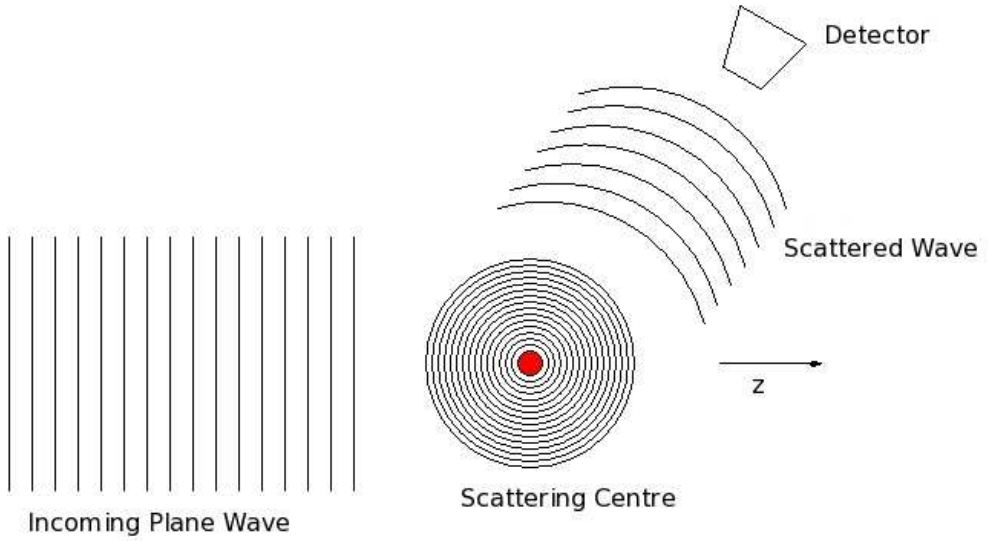

Figure 1.2: Scattering of a plane wave from a spherically symmetric potential.

It is possible to rewrite the incoming plane wave as a sum of angular momentum dependent spherical waves

$$e^{ikrcos\theta} = \sum_l i^l (2l+1) j_l(kr) P_l(cos\theta) \tag{1.5}$$

where j_l are spherical Bessel functions and $P_l(cos\theta)$ are Legendre polynomials. The scattering potential then introduces a phase shift (δ_l) in each partial wave. This is incorporated into the scattering matrix

$$S_l(k) = e^{2i\delta_l(k)} \tag{1.6}$$

The scattering amplitude can now be expressed in terms of phase shifted partial waves

$$f(\theta) = \sum_l (2l+1) \frac{(S_l(k)-1)}{2ik} P_l(cos\theta) \tag{1.7}$$

Finally, using equations 1.3 and 1.7 the elastic scattering cross section can now be re-written using partial waves.

$$\sigma = \frac{4\pi}{k^2} \sum_l^{\infty} (2l+1) sin^2\delta_l \tag{1.8}$$

This approach has led to partial wave analysis (PWA) becoming a common and powerful technique for interpreting experimental data. The magnitude and angular

dependence of different partial wave contributions helps determine which resonances contribute to a particular cross section. Two models specifically developed for nucleon resonance studies, SAID and MAID, are discussed in section 1.5.

1.4 Meson Photoproduction

It was stated in the previous section that a cross section enhancement is an indication of an intermediate resonant state. In the case of the photoexcitation of a proton or neutron target it is possible to induce nucleon resonances. As the resonances decay back to the ground state the study of the decay products allows access to the resonance properties. The resonances are labelled using the spectroscopic notation $L_{2I2J}(W)$, where L is the orbital angular momentum (using the standard s, p, d classification), I is the isospin, J is the total angular momentum and W is the mass in MeV/c^2.

During the 1950s and 60s the study of meson photoproduction was of limited interest due to the low duty factor of the available electron beams. The combination of low duty factor pulsed beams inducing a large random background and insufficient detector timing resolution meant that only inclusive measurements could be performed, in which only one of the final state particles were detected. This limited the amount of reaction information which could be extracted. During the 1970s continuous-wave beams began to be developed, such as the MAMI accelerator used in the current experiment (see section 3.2). By the 1990s high quality, high intensity beams were in operation at several laboratories. This coupled with 4π solid angle coverage for detecting the reaction products and improvements in beam and target polarisation technologies has led to the use of meson photoproduction in many hadronic physics experiments that seek to better understand the nucleon's resonance spectrum.

As a photon interacts with a nucleon it couples to the nucleon electromagnetic current. This can cause the production of mesons via the decay of an intermediate resonant state of the nucleon. The electromagnetic current contains two parts:

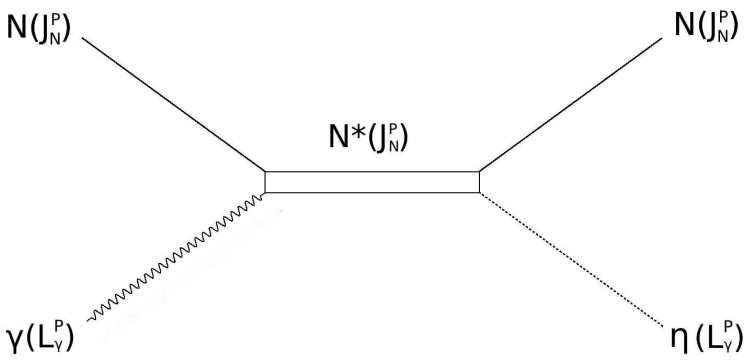

Figure 1.3: η photoproduction via the intermediate excitation of an N* resonance.

isovector and isoscalar. The isovector component allows isospin to vary by one whereas the isoscalar component conserves isospin. The most common meson photoproduction experiments are those involving the pseudoscalar mesons; π, η and K. Pions are isovector particles which can couple to both isospin 1/2 and 3/2 resonances, whereas the η is an isoscalar particle which only couples to isospin 1/2 resonances. The s-channel photoproduction of an η from the decay of an N* resonance is shown in figure 1.3.

1.5 Model Analyses

Partial wave analyses use a transition matrix to describe the conversion between an initial and final state of a photoproduction reaction. This matrix is split into a resonant component and a non-resonant background part and is then decomposed into a set of partial waves each with a specific angular momentum. This framework allows a fit to be performed to the experimental data in order to extract resonance properties. The two main models used to interpret η photoproduction data are ETA-MAID [10] developed by the University of Mainz, and SAID [11, 12] developed by the CNS Data Analysis Centre at George Washington University.

The ETA-MAID model is based on the unitary isobar model MAID [13]. The key difference between the models is the use of additional information from pion nucleon

scattering in MAID, whereas this is not possible in ETA-MAID due to the lack of η nucleon scattering data. In ETA-MAID the non-resonant background of Born terms and vector meson ($\omega\rho$) exchanges are treated using an effective Lagrangian. The nucleon resonances with 4* PDG [14] ratings between 1520-1720 MeV are included in the model and are assumed to have a Breit Wigner energy dependence. It is possible to switch on and off each individual resonance contribution, allowing different predictions to be made using only certain resonances. The SAID model is similar to MAID but does not make any assumptions on the resonances included in the fit. Instead the fit is constrained by the world data-set of pion nucleon scattering and meson photoproduction results.

1.6 Summary

The work undertaken for this thesis is part of a broader worldwide program involving several experimental facilities including JLab, MaxLab and MAMI as well as theoretical groups, such as those responsible for SAID and MAID. The goal of the program is to explore the nucleon resonance spectrum in order to better understand the structure and properties of the nucleon. The current document presents a measurement of the η photoproduction ($\gamma p \rightarrow N^* \rightarrow \eta p$) cross section on a proton target. The primary aim of the work is to provide experimental data which will help to verify the existence or otherwise of the N*(1685) nucleon resonance.

Chapter 2 discusses the previous measurements of relevance and provides an overview of the motivation behind the current measurement. The accelerator facility and experimental detectors used in the present work are described in chapter 3. Chapter 4 describes the corresponding detector calibrations needed to convert raw signals into meaningful physics data, as well as the data analysis steps required to select the $\gamma p \rightarrow N^* \rightarrow \eta p$ reactions. The process of converting reaction channel yields into a full η photoproduction cross section is then discussed in chapter 5. Finally, chapter 6 presents the results, with a focus on the energy region of the N*(1685), as well as a discussion and interpretation of these results.

Chapter 2

Previous Measurements and Motivation

During the past decade there has been much interest in the search for the N*(1685) nucleon resonance. The GRAAL [15, 16, 17], CBELSA/TAPS [18] and LNS [19] collaborations have all produced data which could indicate its excitation from the neutron in a deuteron target. This chapter reviews and presents these results before discussing the motivation for the present measurement on the proton target. The theoretical model which predicts a narrow N* resonance with a mass of 1685 MeV is introduced, as are the resonance's predicted properties and how these manifest themselves experimentally. Other potential explanations for the experimental evidence that do not require the existence of a new resonance, are also presented. Finally, the reasons for performing the current experiment are explained, along with how this work can contribute to the debate over the existence of the N*(1685).

2.1 Previous Measurements

The previous measurements which have focused on the search for the N*(1685) resonance have relied on the processes of η photoproduction and Compton scattering, both of which require a photon beam. There are two commonly used methods of

converting electron beams for use in photo-hadronic physics experiments: Compton backscattering of laser photons on high energy electrons and tagged bremsstrahlung from a radiator. Each of the following experiments employ a very similar setup. A photon beam impacts a cryogenic hydrogen or deuterium target and excites a proton or neutron into a resonant state which then decays. In order to detect and measure the properties of the resulting decay products, the target is surrounded by an electromagnetic calorimeter and a scintillation hodoscope that is used to perform charged and neutral particle identification.

2.1.1 GRAAL Experimental Setup

Several relevant experiments have been performed by the GRAAL collaboration based at the European Synchrotron Radiation Facility (ESRF) in Grenoble, France, all of which have produced results which indicate structure around the 1685 MeV energy region. The GRAAL setup uses the Compton backscattering technique in which a silicon microstrip detector determines the energy and timing signature of the recoil electron, and thus the energy and timing of the scattered photon. The photon polarisation ranges from nearly 100% at the maximum beam energy to 60% at the η production threshold. Both the polarisation and photon energy vary depending on the scattering angle. A schematic diagram of the detector system in the experimental area is shown in figure 2.1. A 4 cm diameter, 6 cm long target cell, able to hold liquid hydrogen or deuterium, is surrounded by the central detectors. The 4π LAγRANGE calorimeter is capable of detecting both charged and neutral particles and consists of 480 BGO crystals, covering the 25° - 155° polar angle range. Charged particles in the BGO ball are identified by an energy and angular comparison of signals produced by the plastic scintillator barrel surrounding the target. Charged particle tracks can also be reconstructed from two sets of multi-wire proportional counters (MWPCs): one cylindrical module surrounding the target and two planar modules downstream from the target. Finally, to detect particles in the forward angle region, a Time-of-Flight (TOF) wall consisting of a plastic scintillator hodoscope and a lead scintillator shower detector is situated 3 metres downstream from the target.

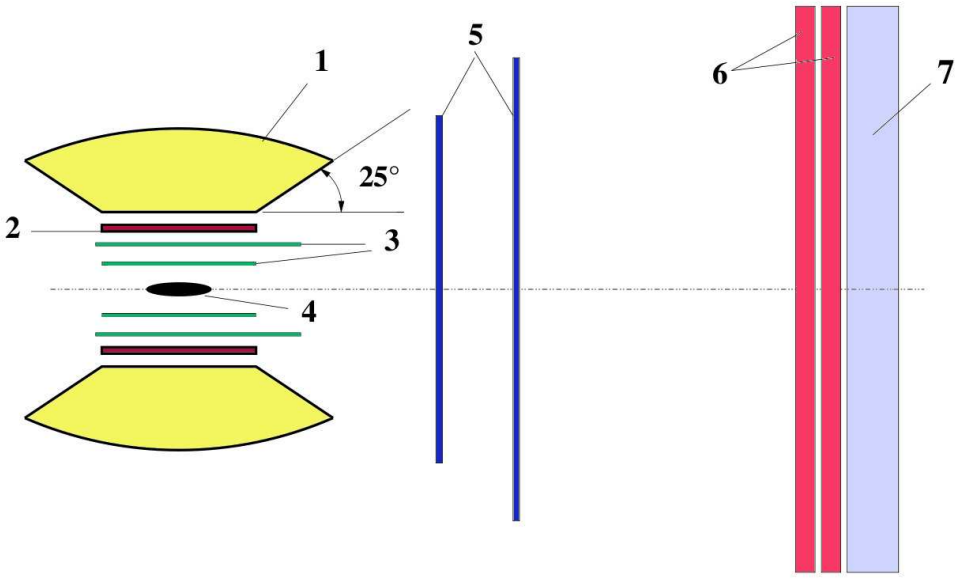

Figure 2.1: The GRAAL experimental setup: (1) BGO Ball, (2) Plastic Scintillators, (3) Cylindrical MWPCs, (4) Target, (5) Planar MWPCs, (6) Plastic Scintillator Hodoscope, (7) Pb Scintillator Shower Detector. Modified from reference [20].

2.1.2 GRAAL Cross Section Measurement

The GRAAL collaboration published the quasi-free cross section for the $\gamma d \rightarrow \eta p$ and $\gamma d \rightarrow \eta n$ reaction channels using a deuterium target [15]. The analysis was designed to select the 2γ decay branch of the η, with the invariant mass [1] of the two photons detected in the BGO ball being reconstructed to identify η mesons. The recoil nucleons were identified by comparing the measured and expected kinematic information under the assumption that the nucleon interacted with the incoming photon as a quasi-free particle, with the other nucleon bound in the deuteron acting purely as a spectator. Cuts were made to the nucleon missing mass, TOF and meson polar angle values in order to reduce events which contained re-scattering and final state interactions with the spectator nucleon.

For the $\gamma d \rightarrow \eta n$ reaction the combined invariant mass of the η and neutron was

[1] Invariant mass of two photons is defined as $m_{2\gamma} = \sqrt{2E_1E_2(1 - cos\theta_{12})}$, where E_1,E_2 are the photon energies and θ_{12} the opening angle.

calculated and is shown in the lower right pane of figure 2.2. This shows a peak on the shoulder of the dominant S_{11} resonance. The peak was enhanced by reducing the width of the cuts on the kinematic properties and only accepting events where the neutron is detected in the forward wall detector. The top two and bottom left panes of figure 2.2 show the corresponding cross sections in different angular regions over the same energy range. As with the ηn invariant mass, a peak structure around W = 1680 MeV/c^2 is seen in all three cross section plots, although the cross section magnitude of the peak increases at forward angles. No such structure was seen on the $\gamma d \rightarrow \eta p$ channel. The authors of reference [15] suggest that the enhancement in the ηn cross section which is not present in ηp is caused by a narrow nucleon resonance. They have therefore included in the cross section plots a simulated peak with a mass of 1680 MeV/c^2 and a width of 10 MeV/c^2. The reason for the width of the peak being much larger than 10 MeV/c^2 is due to it being smeared by the Fermi motion of the target neutron within the deuteron. This is one of the major limitations in searching for narrow resonant structures with deuterium targets.

2.1.3 GRAAL Compton Studies

In 2011 Kuznetsov et al. published the results of an investigation into quasi-free Compton scattering off the deuteron [17]. Simultaneous measurements were performed for both $\gamma d \rightarrow \eta p$ and $\gamma d \rightarrow \eta n$ channels. The γN final states were selected by a series of cuts on the nucleon missing mass, the TOF values and the angle of the recoil nucleon. A major source of background for Compton scattering is π^0 photoproduction. A cut on the total missing energy of the system was used to differentiate between these two types of event, although the authors note there is still some degree of π^0 contamination. The results of the study are shown in figure 2.3, with the left pane showing Compton yields for the quasi-free proton and the right pane for the quasi-free neutron. There is evidence for a narrow peak on the $\gamma d \rightarrow \eta n$ channel. The position of the peak was found to be 1686 $\pm$ 12 MeV/c^2 with a width of 28 $\pm$ 12 MeV/c^2.

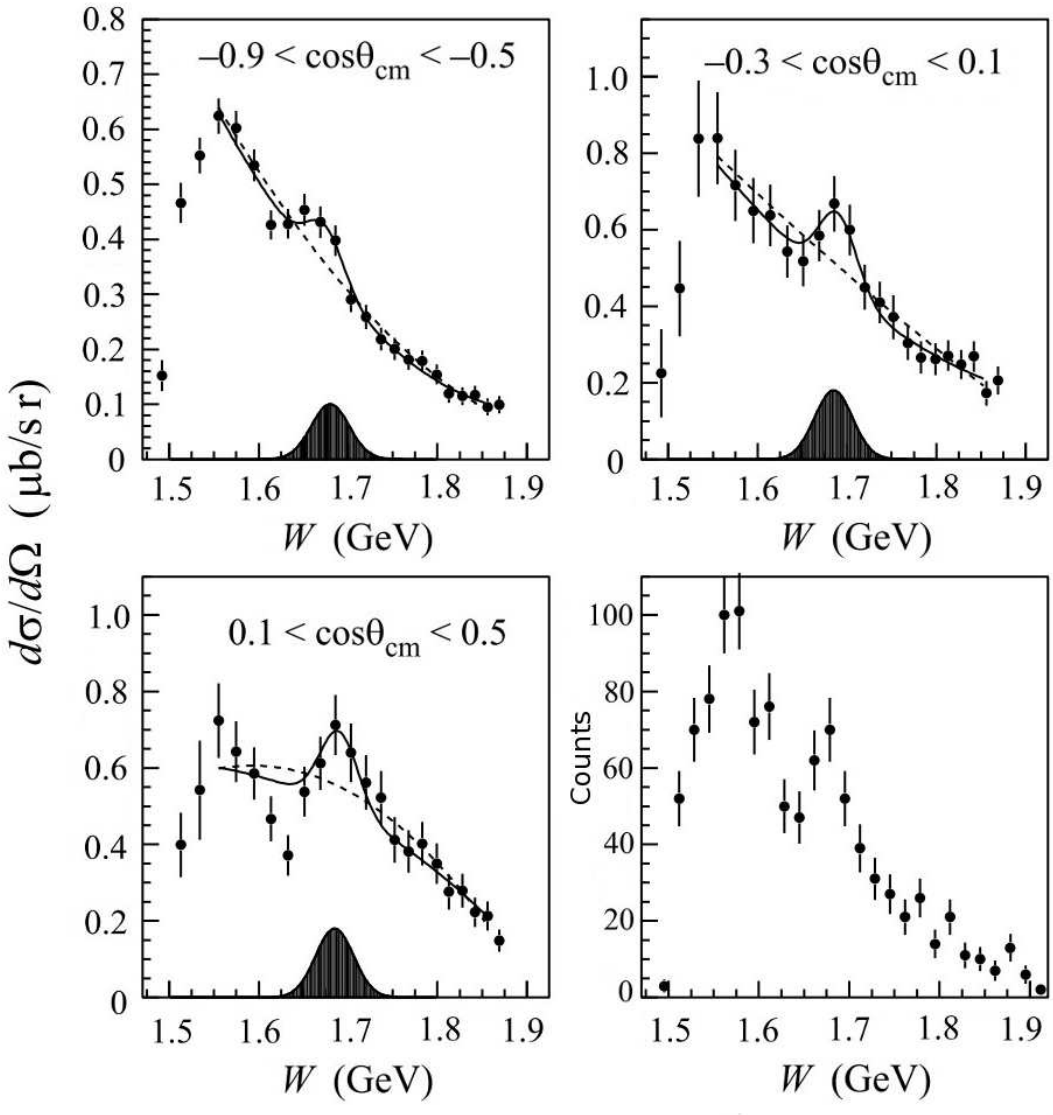

Figure 2.2: Upper left and right and lower left: Differential $\gamma d \rightarrow \eta n$ cross section from GRAAL as a function of centre of mass energy for three different η polar angle ranges. The solid line is a fit to a narrow resonance on a 3rd order polynomial background. The dashed line is a fit without any narrow resonance. The shaded peak is a simulation of a narrow resonance. Bottom right: ηn invariant mass over all angular bins. Taken from reference [21].

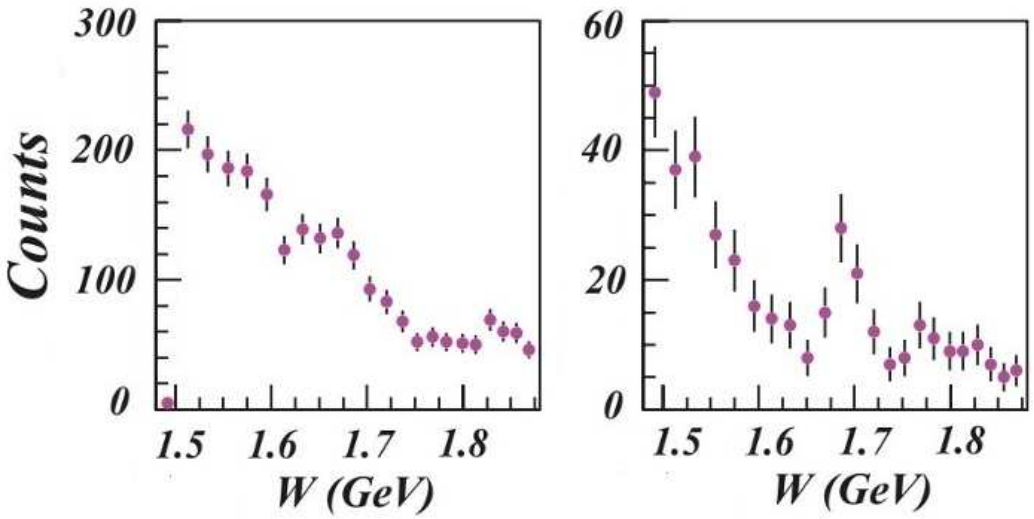

Figure 2.3: GRAAL Compton scattering results. Left: quasi-free proton data. Right: quasi-free neutron data. Modified from reference [17].

2.1.4 GRAAL Beam Asymmetry Measurement

In 2008 Kuznetsov et al. [16] published a re-analysis of photon beam asymmetry (Σ) data for the $\gamma p \rightarrow \eta p$ reaction, originally collected by GRAAL in 1998 and 1999 using a liquid hydrogen target. Two types of events were analysed: in the first type the η was reconstructed from the invariant mass of two photons detected in the BGO ball. In the second type, in which one photon was detected in the forward wall, the η was then reconstructed from the detected proton. A kinematic fit was applied to both types of events to determine the azimuthal angle between the ηp reaction plane and the plane of the photon beam's linear polarisation (P_γ). The resulting Σ beam asymmetries, as defined by equation 2.1, are obtained from forming an asymmetry from these azimuthal angular distributions of orthogonal beam polarisation states ($\sigma_\parallel$ and $\sigma_\perp$). These are shown in figure 2.4 for five different η polar angles.

$$\frac{\sigma_\parallel + \sigma_\perp}{\sigma_\parallel - \sigma_\perp} = P_\gamma \Sigma cos(2\theta) \tag{2.1}$$

The $\theta_{cm} = 43°$ bin exhibits a peak in the asymmetry at $E_\gamma = 1040$ MeV (W = 1680 MeV), with evidence for some structure around this beam energy in all θ_{CM} bins.

These structures are believed to arise from an interference pattern created between overlapping resonances which may be a sign of a narrow nucleon resonance.

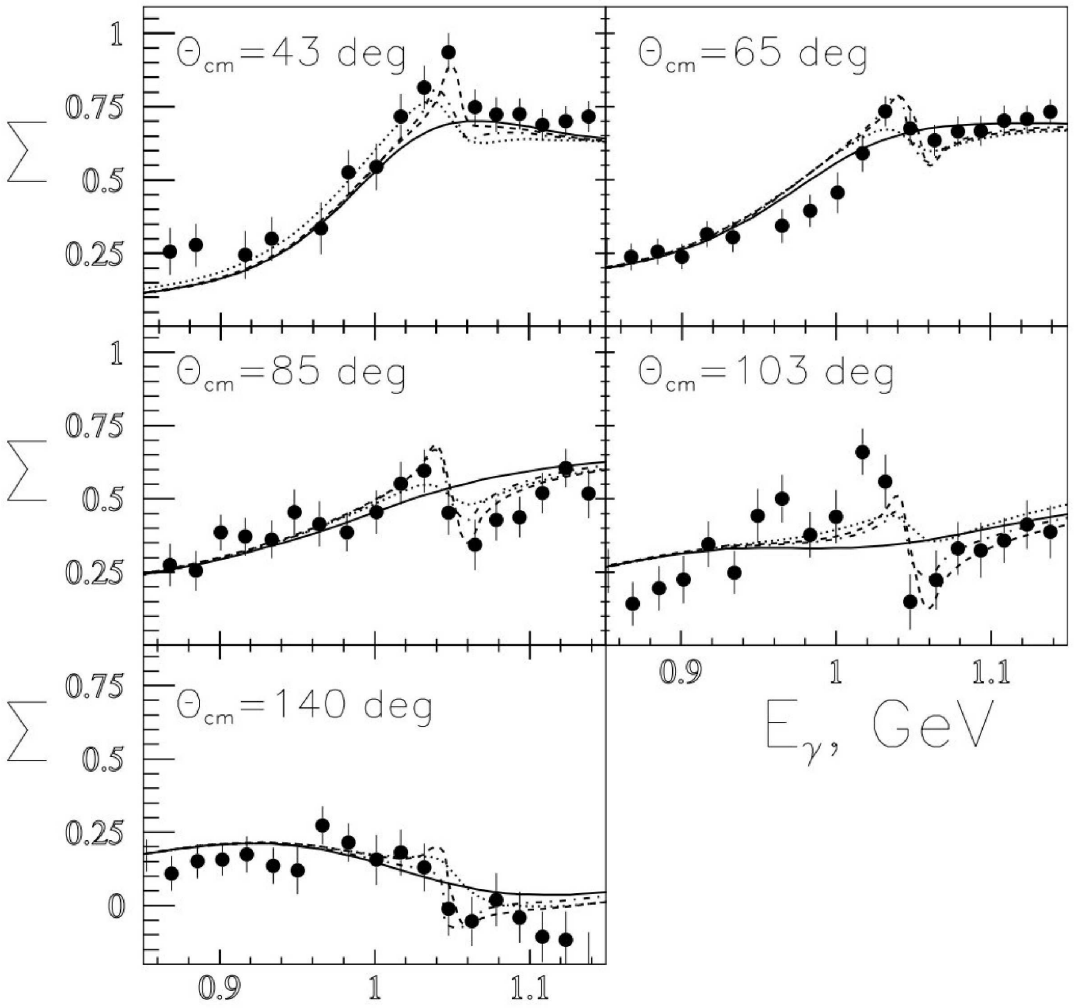

Figure 2.4: η photoproduction photon beam asymmetry (Σ) results from GRAAL. The lines show SAID predictions for different resonance assumptions, with the solid line showing the standard SAID predictions and the various dotted and dashed lines each including an additional narrow D or P wave resonance. Dotted: P_{11}. Dashed: P_{13}. Dot-dash: D_{13}. Modified from reference [21].

2.1.5 ELSA Experimental Setup

The CBELSA/TAPS collaboration based at the ELectron Stretcher Accelerator (ELSA) in the University of Bonn, Germany, uses electrons extracted from a stretcher ring to produce photons using the tagged bremsstrahlung technique. Figure 2.5 shows the experimental detector setup. The centrally positioned target is filled with either LH_2 or LD_2 and is surrounded by the SciFi (Scintillating Fibre) and Crystal Barrel detectors. The Crystal Barrel consists of 1380 CsI(Tl) scintillators and covers a 12° to 168° range in polar angle. Charged particles are identified by angular and energy correlations between the Sci-Fi detector and the Crystal Barrel. To cover the missing acceptance at forward angles TAPS, a highly segmented BaF_2 calorimeter, is used as a forward wall. This is a very similar detector to the TAPS arrangement used in the current experiment and is described in section 3.7.

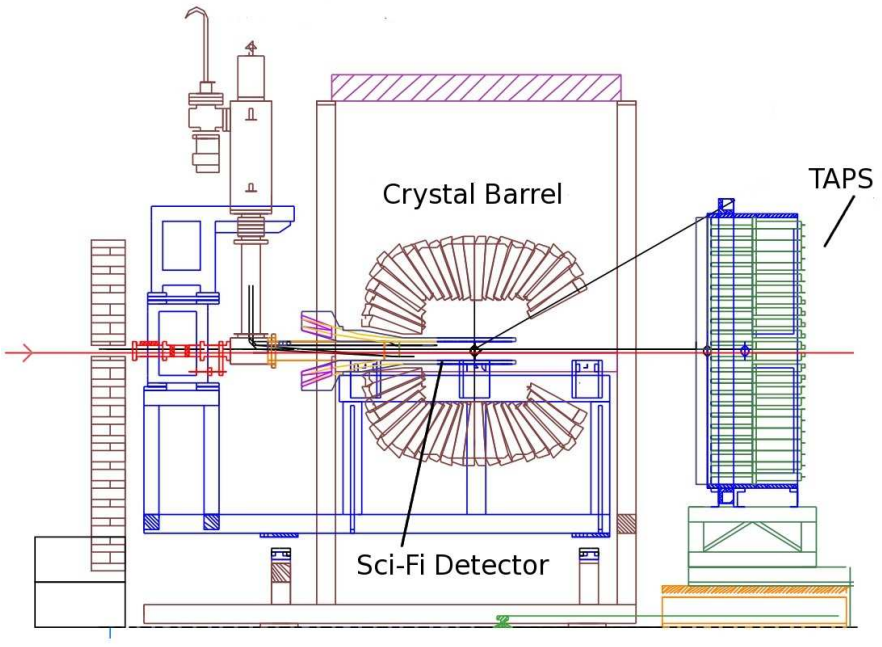

Figure 2.5: CBELSA/TAPS experimental setup. Modified from reference [22].

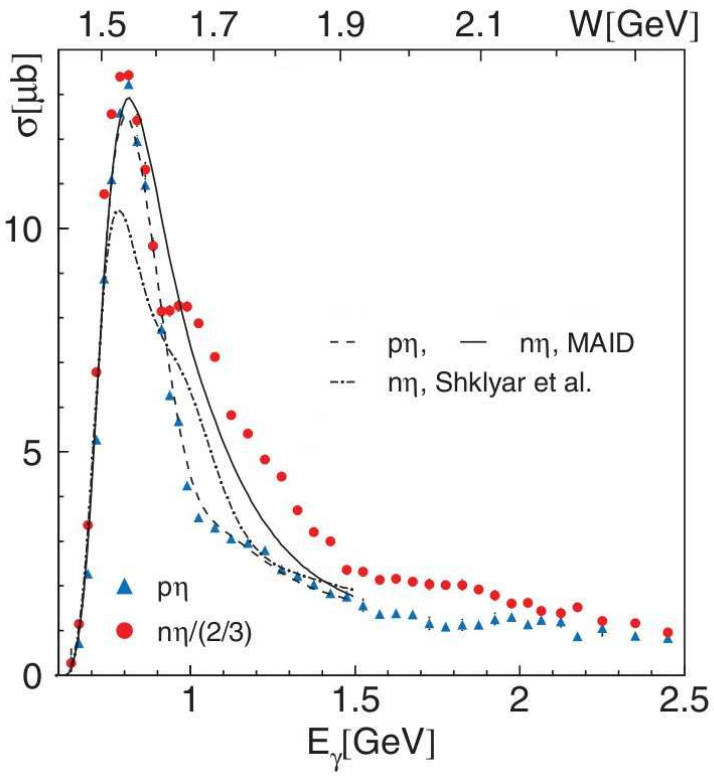

Figure 2.6: CBELSA/TAPS total η photoproduction cross section. Shklyar et al curve uses the model from reference [23]. Figure taken from reference [18].

2.1.6 CBELSA/TAPS Cross Section Measurement

The CBELSA/TAPS collaboration published cross section measurements of quasi-free η photoproduction from a liquid D_2 in 2008 [18]. Both proton and neutron channels were analysed with two incident beam energies of 2.6 and 3.2 GeV. The analysis relied on the detection and reconstruction of the $\eta \rightarrow 3\pi^0 \rightarrow 6\gamma$ decay branch, with events only being accepted if six photons could be reconstructed to three pions. The $3\pi^0$ combined invariant mass was then determined to identify events corresponding to η mesons. The recoil nucleons were selected using the missing mass technique to differentiate between η and $\pi\eta$ events.

The total cross sections for both proton and neutron channels are shown in figure 2.6. The neutron data exhibits a peak around W = 1680 MeV/c^2 which is not seen in the corresponding proton results. The Fermi motion of the target can be corrected on an

event-by-event basis if the kinematic information of the recoil nucleon is determined. The cross section results for this are shown in figure 2.7. This correction was only possible with events in which the neutron energy was determined in TAPS via TOF, which corresponds to η mesons with $\cos(\theta_\eta) <$ -0.1. The effect of the correction is a narrowing of the anomalous peak structure on the neutron channel, the mean position of which is 1683 MeV/c^2 with an upper limit of its width of 60 $\pm$ 20 MeV/c^2.

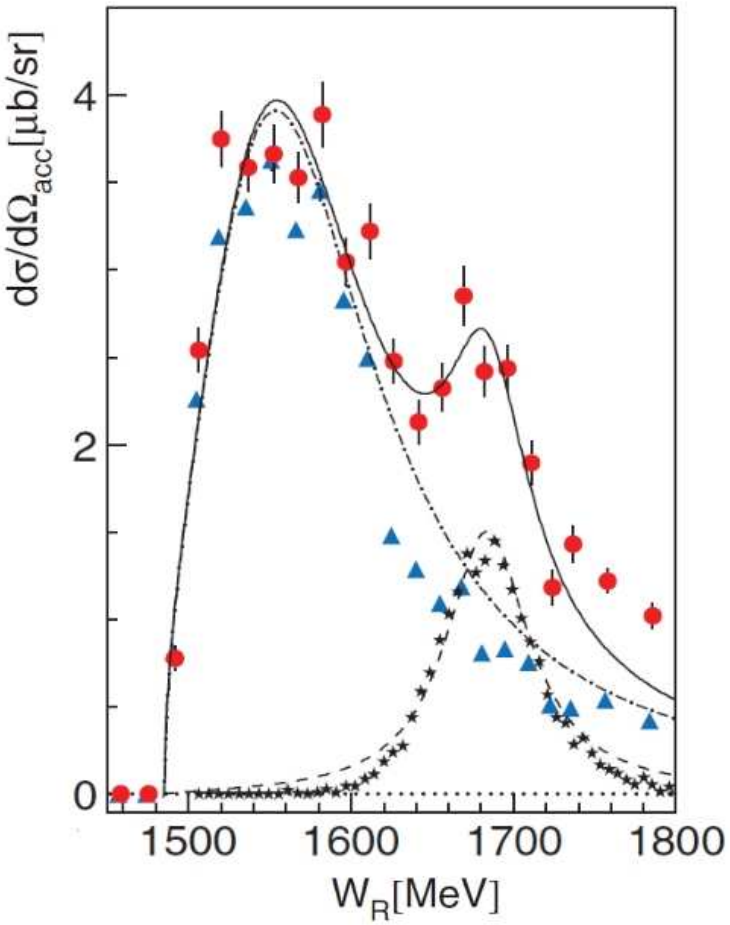

Figure 2.7: η photoproduction cross section results ($\cos(\theta_\eta) <$ -0.1) as a function of invariant mass from measurements at CBELSA/TAPS. The circles are neutron data ($\gamma d \rightarrow \eta n$) and the triangles are proton data ($\gamma d \rightarrow \eta p$). Stars: simulation of delta function smeared by energy resolution. Solid curve: full fit to neutron points. Dash-dot curve: Breit-Wigner fit to $S_{11}(1535)$. Dashed curve: fit to second structure. Taken from reference [18].

2.1.7 LNS Experimental Setup

The GeV-γ experimental hall is situated in the Laboratory of Nuclear Science (LNS) at Tohoku University, Japan [24]. LNS is similar in design to ELSA and the Mainz setup (described in chapter 4) and uses the tagged bremsstrahlung technique to produce a photon beam with an energy range of 580 - 1160 MeV. The experimental setup of the GeV-γ hall is shown in figure 2.8. 206 pure CsI crystals are arranged into four blocks and comprise the primary calorimeter. The two forward blocks cover polar angles between 15° to 75°, whilst the two backward angle blocks cover 95° to 125°. To facilitate the detection of charged particles each crystal is covered by an individual 5 mm thick plastic scintillator.

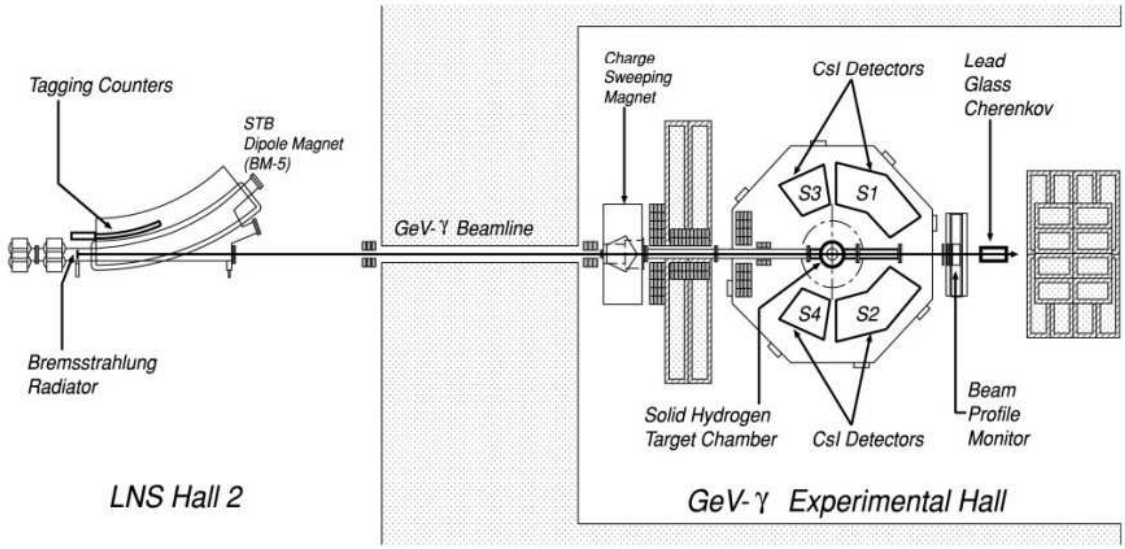

Figure 2.8: LNS experimental setup. Taken from reference [24].

2.1.8 LNS Cross Section Measurement

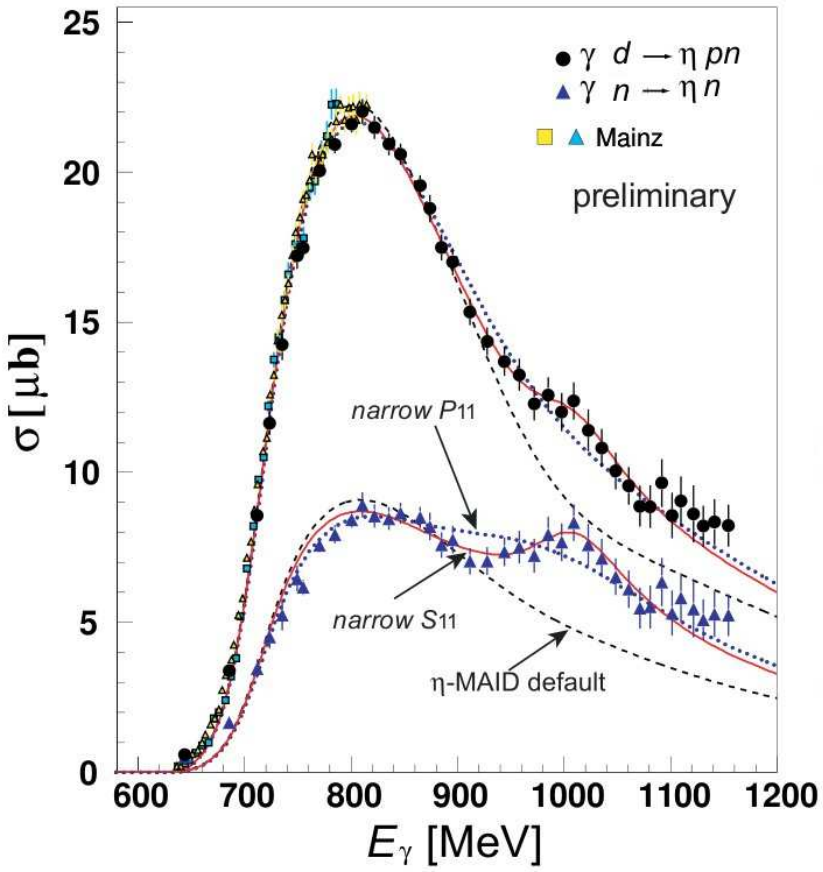

Figure 2.9: LNS deuteron and neutron total η photoproduction cross sections. Dashed line: prediction from the standard ETA-MAID model. Dotted line: ETA-MAID model including additional P_{11} resonance. Solid line: ETA-MAID model including additional S_{11} resonance. Taken from reference [19].

Cross section measurements of η photoproduction on the deuteron performed at LNS were published in 2007 [19]. The analysis relied on the $\eta \rightarrow 2\gamma$ decay branch to identify η mesons from the reconstructed invariant mass spectrum. A background subtraction was performed to account for the unwanted π^0 contribution. The η yield was then converted to the cross section shown in figure 2.9. Both deuteron and neutron channels have been analysed with each of the cross sections showing a peak structure with a mass of W = 1666 $\pm$ 5 MeV/c^2 (E_γ = 1010 MeV) and a width of approximately 40 MeV/c^2.

2.2 Chiral Soliton Model

Some of the experimentalists responsible for the results shown in the previous sections argue that the anomalous peak structure may be evidence for a new exotic baryon as predicted by the chiral soliton model. The theory of chiral solitons is based on a model developed by Skyrme in the 1960s. Skyrme states that light baryons can be described as a symmetrically spherical soliton solution to the chiral (pion) field [25]. The model states that the space rotation of the field is equivalent to that of isospin space. If the soliton rotation is quantised, each isospin value results in a multiplet of degenerate nucleon states. This suggests that baryon resonances can be treated as rotational excitations of the classical nucleon, without recourse to subnucleonic degrees of freedom as in the quark model [26]. The chiral soliton model was largely ignored for the subsequent twenty years before being expanded upon by Witten in 1983. Two important modifications were made to include both the baryon number [27] and colour charge symmetries [28]. There was much success in predicting the masses of the baryon octet to within a few percent, with the mass splitting of the octet being determined purely from symmetry relations [29].

The Skyrme model was refined into the more physical chiral quark soliton model, which included quantisation based upon valence quarks [30, 31]. This resulted in selection rules which state that the first rotational excitation is an octet with spin 1/2; the second, a decuplet with spin 3/2; and the third, an antidecuplet with spin 1/2 [29,32,33]. One might then reasonably expect the third excitation to be spin 5/2. However, this causes centrifugal forces to contort the spherically symmetric nature of the soliton solution and is therefore not possible [34,35]. The antidecuplet is said to be exotic as the quantum numbers of several of the predicted states can only result from the combination of more than three quarks. A diagram of the antidecuplet, as produced by Arndt et al. [36], is shown in figure 2.10. The estimated width of the N* member of the antidecuplet is ≤ 30 MeV/c^2 [36]. Calculations of the electromagnetic transition moments by Polyakov and Rathke [37] show that the photoexcitation of the antidecuplet should in general not be possible from a proton target and will

only occur due to isospin symmetry breaking effects. This leads to the neutron photocoupling to the antidecuplet being stronger by a factor of between 50 - 250 than that of the proton [21]. The chiral soliton model is therefore often relied upon in cases where anomalous structure is observed in neutron cross section results but not in the equivalent proton results. The problem remains that, in spite of several recent controversial results of this nature [15,16,18,19], no definitive evidence exists for a member of the exotic baryon antidecuplet.

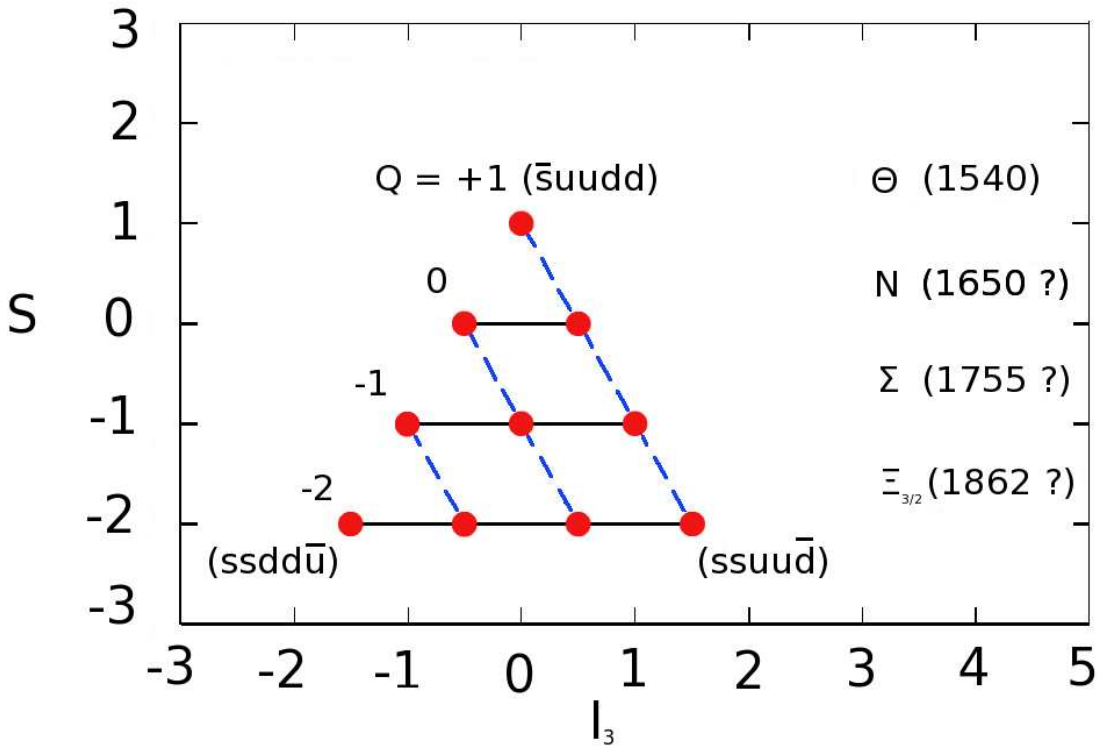

Figure 2.10: Spin 1/2 baryon antidecuplet as predicted by the chiral soliton model (S = strangeness, I_3 = projection of isospin). Modified from reference [36].

2.3 Interpretation of Evidence for the N*(1685)

All of the previous measurements presented in section 2.1 showed evidence for anomalous structure in the region of 1685 MeV/c^2 in η photoproduction and Comp-

ton scattering on the deuteron on the quasi-free neutron channel. Attempts have been made to explain this structure in terms of a new nucleon resonance, which many claim is the non-strange member of the antidecuplet predicted by the chiral soliton model described above [26, 36, 38].

The authors of the GRAAL cross section measurement argue that the neutron peak is a sign of the N*(1685) resonance. The results shown in figure 2.2 include a narrow $P_{11}(1675)$ resonance (using the parameters predicted from the chiral soliton model in reference [39]) within the ETA-MAID model in an attempt to replicate the data. This resulted in a narrow structure on the neutron cross section whilst leaving a smooth proton cross section. They also suggested an alternative candidate which is a well known 4* PDG resonance and has strong photocoupling to the neutron in the energy range of interest: the $D_{15}(1675)$ [40, 41]. Assuming this resonance decays to an η with a branching ratio of 17% the ETA-MAID solution can reproduce the neutron data. However, it must be noted that the PDG value for this branching ratio is close to zero. The authors of reference [18] also note that this ETA-MAID solution can reproduce the neutron peak in the CBELSA/TAPS cross section.

Analytical models have been fitted to the GRAAL beam asymmetry (Σ) measurement to analyse the shape of the data for any signs of a nucleon resonance. Firstly the SAID E429 solution for the Σ observable on η photoproduction was plotted on top of the data in figure 2.4. An additional narrow resonance was added to the solution in a attempt to improve the fit. This was performed for several L_{2I2J} values including, P_{11}, P_{13}, D_{13} and S_{11}. The first three of these all improve the fit to the data, although the S_{11} does not. The P_{11} solution produced the best fit with a resonance mass of 1688±9 MeV/c^2 and a width of approximately 19 MeV/c^2.

Interestingly, the authors of reference [19] have also attempted to fit the peak in the LNS cross section measurement in order to assign spin and parity to a possible resonance. The standard ETA-MAID solution was plotted on top of the data in figure 2.9, but does not account for the peak structure. When an additional resonance is included in the ETA-MAID solution the resonance L_{2I2J} value which best fits is S_{11}. This is contrary to the results from GRAAL [15], highlighting the difficulty

in assigning L_{2I2J} values to anomalous structure by relying on partial wave model fits.

Since the publication of the experimental evidence of anomalous structure on the neutron channel there has been much endeavour to explain this structure using known resonances without recourse to the chiral soliton model. Anisovich et al. [42] and Zhong and Zhao [43] suggest that the structure is a result of the interference between the $S_{11}(1535)$ and $S_{11}(1650)$ resonances. Shklyar et al. [23], as well as Shyam and Scholten [44], have produced results based on a coupled-channel approach which takes into account meson-baryon interactions via nucleon intermediate states. The former concludes that the neutron anomaly is a result of interference between the $S_{11}(1650)$ and $P_{11}(1710)$ resonances, whilst the latter explains the peak as a interference effect between the $S_{11}(1535)$, $S_{11}(1650)$, $P_{11}(1710)$ and $P_{13}(1720)$ resonances. Doring and Nakayama [45] state that the observed enhancement in the neutron cross section compared to the proton is due to the production of intermediate strangeness states, specifically the opening of the $K\Sigma$ channel.

2.4 Motivation

It is clear from the results and various interpretations presented in the previous sections that the peak observed in the $\gamma d \rightarrow \eta n$ channel has proven to be a topical and controversial issue. A consensus on the source of the peak has yet to be formed. This leaves open the question of whether the peak is evidence for the non-strange member of the exotic antidecuplet or if it can be explained using more conventional means; either through the interference of known resonances or the effects from the opening of other reaction channels.

Cross section measurements using the $\gamma p \rightarrow \eta p$ reaction channel have previously been performed [46, 47, 48]. However, unlike these previous measurements, the focus of the current experiment is to investigate the energy region around W = 1685 MeV to search for signs of the existence of the N*(1685) resonance. As the predicted proton photocoupling for the N*(1685) is low [21] a higher precision, higher resolu-

tion study is needed. The detector and data acquisition systems available at the A2 collaboration at MAMI offer the potential for just such a measurement.

The relevant A2 detector systems of the Crystal Ball, the Photon Tagger and the Microscope have associated with them an energy resolution which is nearly an order of magnitude better than previous experiments. This high resolution would allow for a detailed measurement of the shape and width of any peaks observed in the cross section. As no free neutron targets exist, the target used in previously mentioned neutron cross section measurements is deuterium. This causes additional nuclear effects that must be modelled and well understood in order to extract meaningful physics data. Firstly, the binding of the neutron and proton within the deuteron causes uncertainty in the initial state momentum of the target nucleon due to their relative Fermi momenta. Secondly, when an η is emitted from the nucleon it may interact with the other spectator nucleon via final state interactions (FSIs). By performing measurements on the free proton there are no complications from initial Fermi motion or FSIs. Given the high resolution and statistical precision achieved in the current experiment, it is hoped that a significant contribution can be made to the understanding of the $\gamma p \rightarrow \eta p$ cross section in the W = 1685 MeV energy region.

Chapter 3

Experimental Setup

3.1 Overview

The dataset for the current experiment was taken as part of the A2 collaboration's experimental program during a three week beamtime in April 2009 at the Johannes Gutenberg Universität, Mainz, Germany. This chapter presents the design and operation of the equipment used to study the $\gamma p \rightarrow \eta p$ reaction. An overview of the experimental hall is shown in figure 3.1. A mono-energetic electron beam is delivered to the experimental hall by the MAinzer MIcrotron (MAMI), as described in section 3.2. This electron beam interacts with a copper radiator to produce photons, the energies of which are then determined by detecting the recoil electrons in the Glasgow-Mainz Tagged Photon Spectrometer (section 3.1). The photons continue towards the experimental area where they interact with the liquid hydrogen target (section 3.4), with the reaction products detected by the Crystal Ball (CB), TAPS and PID detectors (sections 3.5, 3.6 and 3.7 respectively). The PID is positioned between the CB and target and provides the ability to detect and differentiate between charged particles in the CB. A similar veto detector performs the same task for TAPS. Finally, a Pb-Glass detector is situated downstream from the target for use in tagging efficiency measurements.

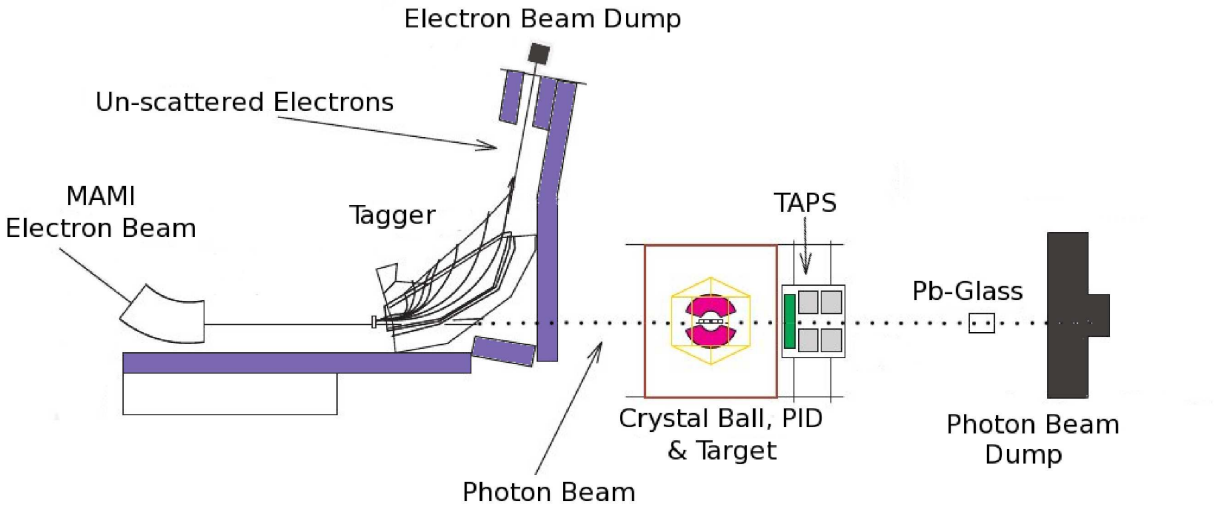

Figure 3.1: Schematics overview of the A2 hall. The MAMI electron beam is used to produce bremsstrahlung photons, whose energy and time is determined by the photon tagger. Photons continue to the target and induce a reaction, the products of which are detected by the PID, Crystal Ball and TAPS. Modified from reference [49].

3.2 The Mainz Microtron

The MAinzer MIcrotron (MAMI) [50] is a 1.5 GeV electron accelerator based at the Institut für Kernphysik, Mainz University, Germany. MAMI is used to produce a continuous-wave electron beam, which can be fed into one of the three experiment halls: A1, A2 or A4 (Figure 3.2). A2 is the tagged photon hall and is the location for the present experiment. MAMI is split into three sections (A, B and C) and uses three Race Track Microtrons (RTMs) and one Harmonic Double Sided Microtron (HDSM).

During the 1970s there was a demand in the nuclear and particle physics community for continuous-wave electron accelerators. Up until this point most measurements performed had detected only one final state particle. Pulsed linear accelerators (linacs) were used to provide electrons in bunches, where a high number of electrons

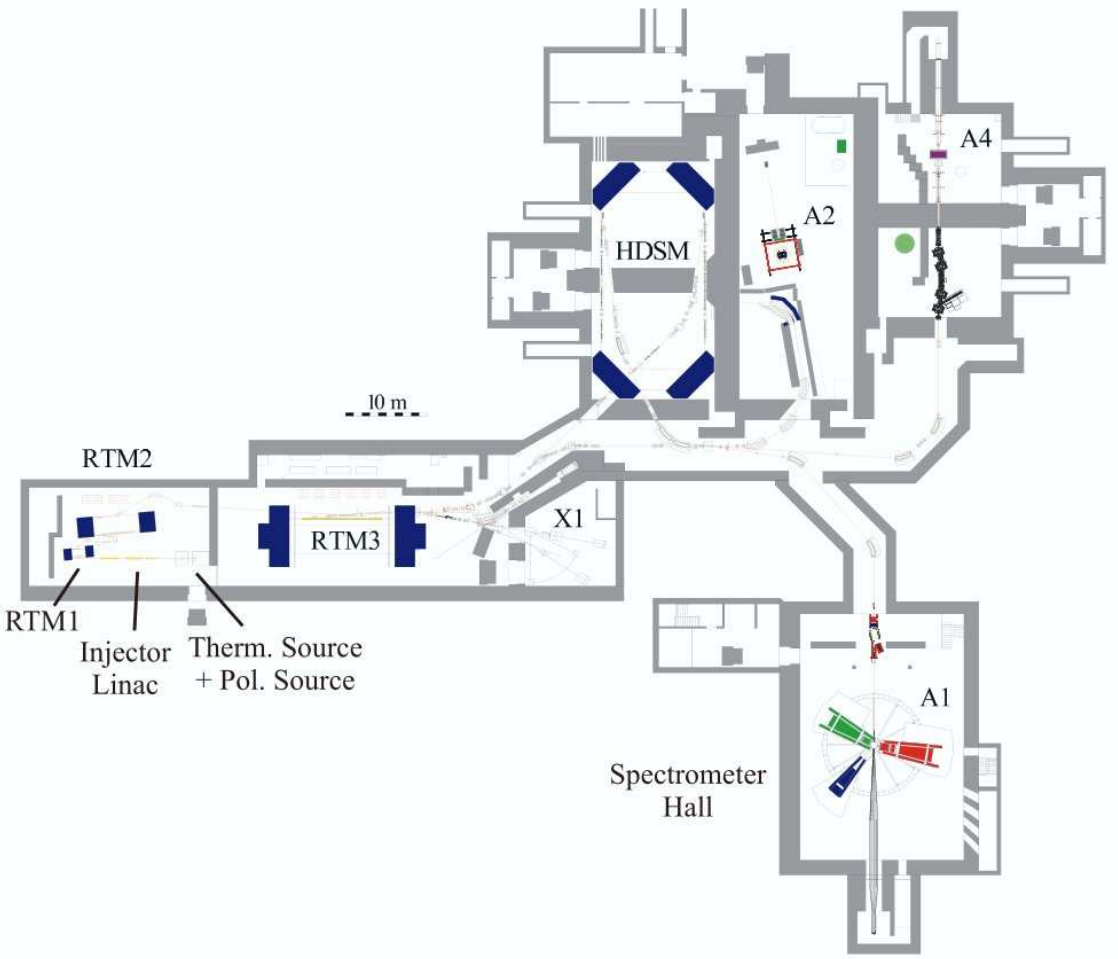

Figure 3.2: Floor plan of the MAMI electron beam accelerator facility [50]. The electron beam can be fed into one of three experimental halls: A1, A2 or A4.

are delivered in a small time period. This made the detection of more than one particle from a final state difficult. This was due to background coincidences from uncorrelated particles from a separate reaction which occurred within the timing resolution of the detector systems. The solution to this problem was to increase the amount of time between electron bunches, which can be achieved by using a continuous-wave electron beam rather than a pulsed beam. One method of producing a continuous-wave beam is to use a race track microtron.

3.2.1 Race Track Microtrons

The design of a typical RTM is shown in figure 3.3. It features two 180° magnets separated by a linac. Electrons are injected into the linac where they pass though standing wave cavities that are powered by radio frequency klystrons. The alternating electric field repels the electron from one cavity and attracts it to the next. As the electrons leave the linac the two magnets each bend the electron path by 180°. The electrons are then focused back into the entrance of the linac. This recirculation is repeated, with the radius of the electron path through the magnets increasing with each turn. Once the required energy has been achieved the electrons are extracted from the RTM. An RTM provides an excellent energy resolution, as electrons with excess energy will re-enter the linac out-of-phase, resulting in a smaller acceleration for that turn. This continues until the phase difference and energy discrepancy is eliminated. The MAMI linacs produce acceleration gradients of around 1 MeV/m. As this gradient is relatively small, the associated power consumption is smaller than that of a pulsed linac. This allows the RTM to operate with a 100% duty factor.

The initial MAMI proposal was published in 1976 [51]. The design included a linac to pre-accelerate the electrons prior to a cascade of three RTMs giving a final electron energy of approximately 800 MeV. These three RTMs make up what is now known as MAMI-B. Electrons are initially produced via photo emission from a GaAs crystal [52]. By using a circularly polarised Ti:Sapphire laser to induce the photo-emission, longitudinally polarised electrons can be produced. The electrons are then pre-accelerated in the linac to an energy of 3.5 MeV. RTM1, RTM2 and RTM3 then accelerate the electrons to 14 MeV, 180 MeV and 855 MeV respectively.

3.2.2 Harmonic Double Sided Microtron

In 1999 a fourth stage of MAMI was approved in order to increase the electron energy to approximately 1.5 GeV [53]. This would allow the study of additional reaction channels as the energy would be above the strangeness production threshold. In

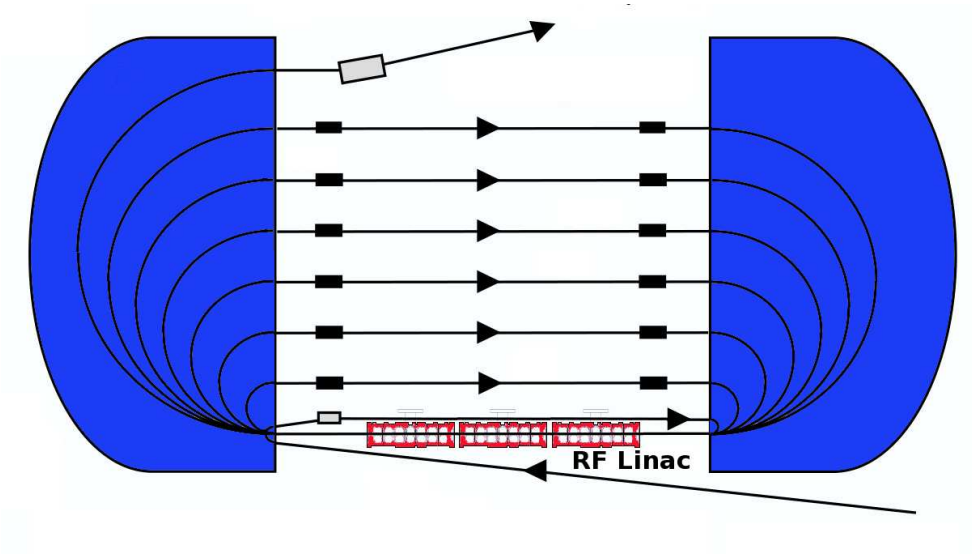

Figure 3.3: A racetrack microtron [50]. The electrons undergo multiple accelerations through the linac, where the number of turns is dependent on the dipole magnetic field strength. The electrons are extracted once the required energy is reached.

order to have an RTM produce a 1.5 GeV beam the weight of each of the two 180° magnets would be in excess of 2000 tonnes, as the weight of the magnets scales with E^3 [54]. A solution to this problem is to use a higher order microtron such as a Harmonic Double Sided Microtron (HDSM). Each 180° magnet is replaced by two 90° magnets, resulting in twice the electron energy for the same total magnet mass when compared to an RTM. The HDSM operates in a similar manner to an RTM, but with two linacs instead of one (see figure 3.4). In order to maintain longitudinal stability linac I is operated at 4.9 GHz, whilst linac II operates at the first sub-harmonic of 4.9 GHz (for more detail see reference [53]). The addition of the HDSM to the RTM cascade is known as MAMI-C, which provides a maximum electron beam energy of 1557 MeV. A summary table of the beam energies and energy resolutions for each stage of MAMI is shown in table 3.1

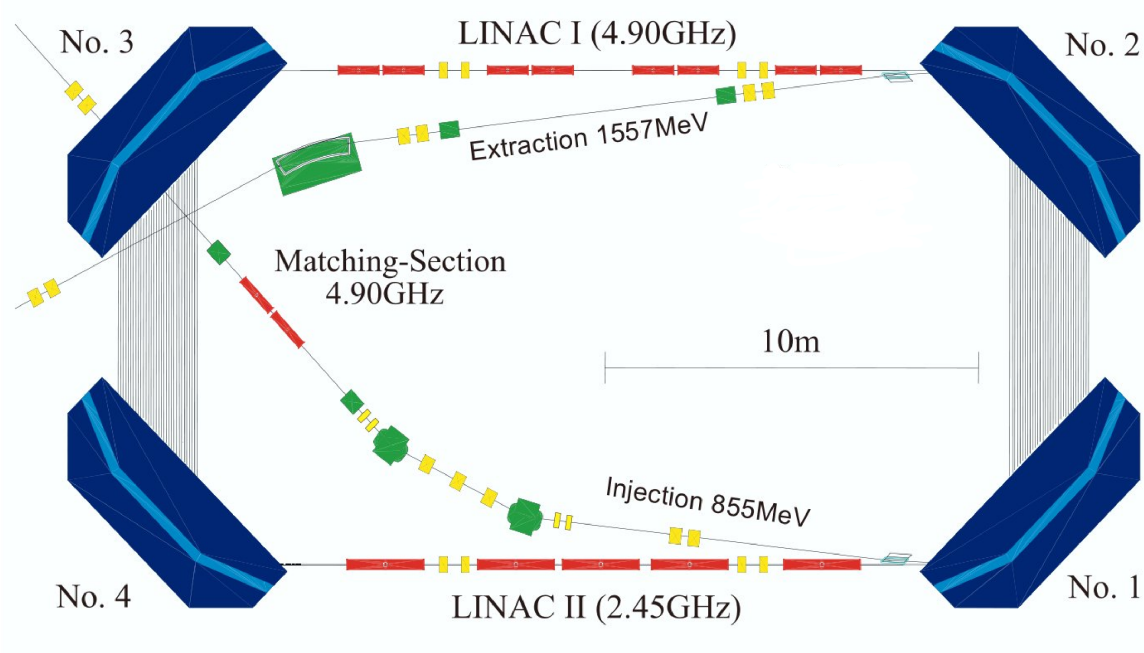

Figure 3.4: The MAMI C Harmonic Double Sided Microtron [50]. The four magnets and two linac design reduces the materials and space needed when compared to an equivalent electron energy RTM.

		RTM1	RTM2	RTM3	HDSM
Injection Energy	MeV	3.97	14.86	180	855
Extraction Energy	MeV	14.86	180	855	1557
Recirculations		18	51	90	43
Energy Resolution (1σ)	keV	1.2	2.8	13	110

Table 3.1: MAMI Beam Parameters.

3.3 Glasgow-Mainz Tagged Photon Spectrometer

The most crucial piece of equipment in the A2 hall is the recently upgraded Glasgow-Mainz Tagged Photon Spectrometer (Tagger) [55], which consists of a goniometer, dipole magnet [56] and focal plane detector (FPD) [57]. The goniometer contains several amorphous and crystalline bremsstrahlung radiators which can be rotated

into the beamline. It is also possible to rotate a Møller coil into the beamline for Møller scattering measurements of electron beam polarisation. As the monoenergetic electron beam impinges on one of these radiators, electrons interact with the nuclei producing a continuous bremsstrahlung spectrum which follows the typical $1/E_\gamma$ shape. The radiator used in the present experiment was a 10 μm Cu wafer. The photons continue down the beamline through a collimator towards the target, whilst the electrons are bent by the dipole magnet towards the FPD. Electrons which do not interact with the radiator are directed into the beam dump (Figure 3.5). A Faraday cup is placed in the beam dump in order to measure the electron beam intensity.

3.3.1 Focal Plane Detector

The degree to which the electrons are deflected in the dipole magnet depends on the energy loss in the interaction at the radiator, thereby correlating the position of impact on the FPD to a particular electron energy. Once the FPD electron energy is known, one can determine the corresponding photon energy:

$$E_\gamma = E_0 - E_{e^-} \tag{3.1}$$

Where E_0 is the MAMI beam energy and the energy lost to the recoil nuclei in the radiator can be considered negligible. A timing coincidence between the Tagger and Crystal Ball is used to establish the incoming beam photon responsible for inducing a given reaction in the target. This determination of energy and timing information for the incoming beam photons is known as 'tagging'.

The FPD and spectrometer magnet were upgraded in 2007 to coincide with the increase in the MAMI beam energy to 1.5 GeV [58]. A Raytrace simulation was performed in order to model the electron optics of the spectrometer. This determines the position at which electrons with the same energy but different opening angles from the radiator are focused, known as the focal plane. The FPD is positioned 50 mm back from the focal plane, to allow a small higher resolution detector known as the microscope (see section 3.3.2) to be optionally inserted in the fo-

cal plane position. The intrinsic resolution of the spectrometer from the magnetic optics is approximately 0.1 MeV, much smaller than the resolution of the FPD elements, therefore the small defocusing from the 50 mm gap does not effect the FPD resolution.

The FPD comprises of 353 plastic scintillators, each with a length of 80 mm, thickness of 2 mm and ranging between 9 and 32 mm in width. The change in width across the detector array keeps the corresponding electron energy width of each channel roughly similar. Each scintillator overlaps its two neighbours by just over half its width; the overlap regions define the 352 tagger channels. The FPD detects electrons in the range of 5 - 93 % of the MAMI beam energy, at an electron beam of 1557 MeV the energy width for the channels is 2 MeV at the highest photon energy and 8 MeV at the lowest, with an average of around 4 MeV. The tagger scintillators are made from the plastic EJ200, which was chosen as it is less susceptible to radiation damage than other scintillators and the scintillation spectrum better matches the response of the photomultiplier tubes (PMTs) [58]. In order to reduce any optical cross-talk between channels the scintillators are wrapped in double sided Mylar. Each scintillator is connected to a Hamamatsu R1635 PMT by a lucite light guide. These PMTs are affected by stray magnetic fields above 0.01 T [59]. Therefore each PMT has a 0.7 mm steel plate fitted to either side. The maximum electron count rate for each channel is 1 MHz.

3.3.2 Tagger Microscope

In addition to the main FPD, the tagger microscope [60] can be used to increase the energy resolution of the tagged photons. The microscope is similar in design to the main FPD, as shown in figure 3.6, but covers a smaller energy region and sits at the actual focal plane in the 50 mm gap between the exit window and the FPD. The microscope consists of 96 plastic scintillator (BCF10) fibres. Each fibre is 235 mm in length with a 3×2 mm^2 cross section. Groups of 16 fibres are connected to multi-anode Hamamatsu 6568 PMTs, with the cathode divided into 16 4x4 mm pixels. This increased segmentation results in an improved energy resolution by a

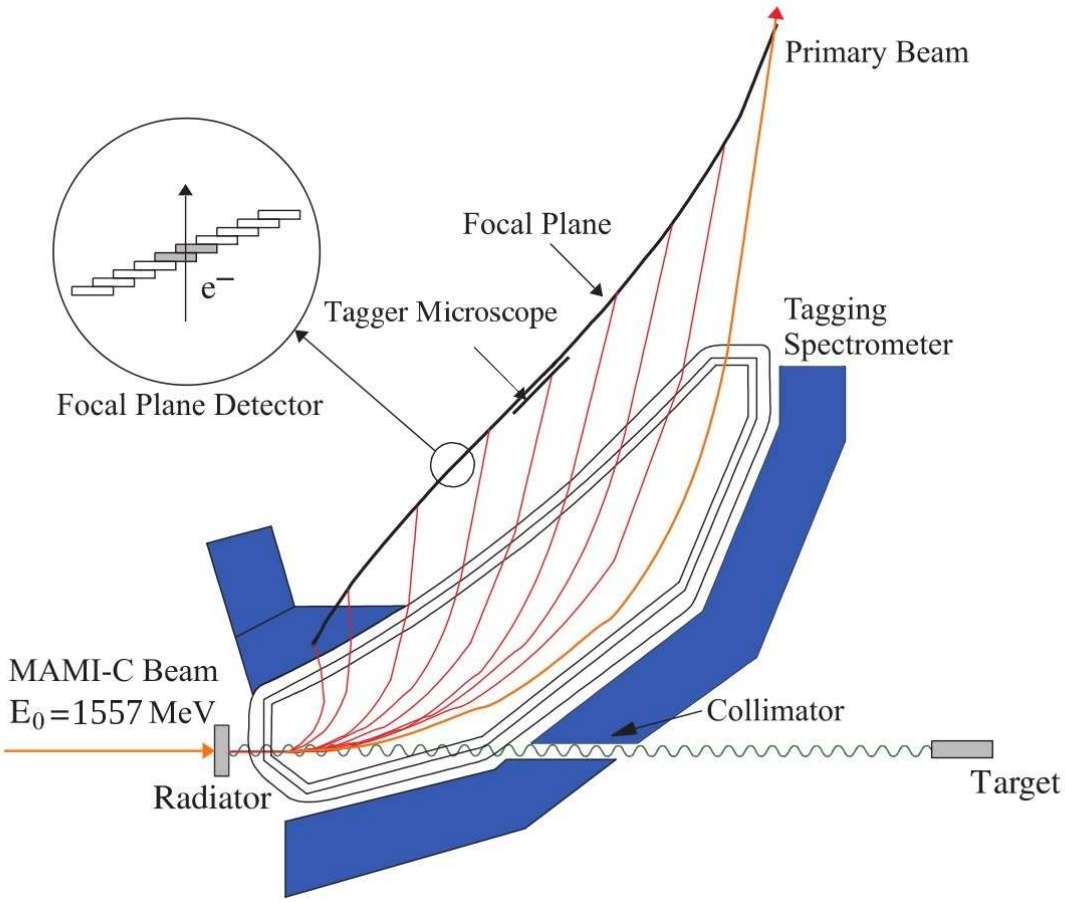

Figure 3.5: Schematic diagram of the photon tagger showing the electron focal plane detector, tagger microscope detector, magnetic spectrometer and radiator. The magnified area shows the overlapping positioning of the focal place scintillators. Not to scale.

factor of 2-6 depending on the incident beam energy, albeit with a much reduced energy acceptance. In the current experiment, the microscope was positioned with the central point at an electron energy corresponding to a centre-of-mass energy of 1685 MeV (E_γ = 1045 MeV).

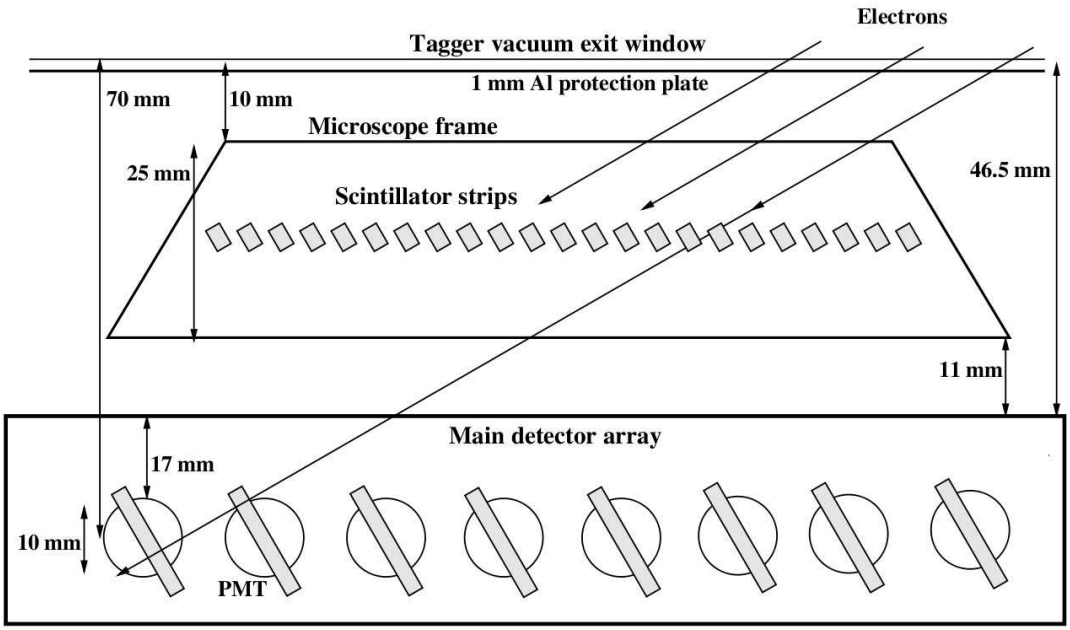

Figure 3.6: Schematic diagram of the tagger microscope detector situated between the tagger vacuum exit window and the focal plane detector.

3.3.3 Photon Collimation and Tagging Efficiency

In order to accurately determine the reaction vertex and keep counting rates to a manageable level, the beam spot size which impinges on the target must be small. To achieve this, the photon beam passes through a collimator before leaving the tagger area. The collimator used in the current experiment was a series of four lead cylinders each with a central 4 mm diameter hole. An ionising chamber was placed downstream from the experimental area, the readings from which were used to aid alignment of the photon beam through the centre of the collimator.

Cross section measurements need an accurate determination of the photon flux. Due primarily to the effects of the collimator the number of electrons detected in the FPD is not equal to the number of photons impinging on the target. This loss must be corrected for by measuring the tagging efficiency. During tagging efficiency runs a Pb-glass detector is placed into the beamline downstream of the CB, and replaces the CB as the trigger for the DAQ. A low beam current is used as this avoids damage to the Pb-glass detector and allows it to operate at approximately

100% efficiency. It also reduces the possibility of multiple hits in the FPD TDCs. The tagging efficiency is defined as:

$$\varepsilon_{tagg} = \frac{N_\gamma}{N_e - N_{e_{bg}}} \tag{3.2}$$

where N_γ is the number of photons that pass the collimation process and impinge on the Pb-glass, these are detected in coincidence with an electron in the FPD. N_e is the total number of electrons detected in the FPD. Background measurements are taken whilst the beam is off, before and after the main tagging efficiency runs. $N_{e_{bg}}$ is the number of background tagger hits, and is subtracted from N_e to correct for any activation which may have built up along the FPD. The tagging efficiency is calculated individually for each FPD channel.

3.4 Cryogenic Target

During the current experiment liquid hydrogen (LH_2) was used as a proton target [61]. The target setup in the A2 hall is located within the beamline vacuum pressure system at a pressure of 3×10^{-7} mBar. This consists of: a hydrogen gas storage tank, gas compressor, liquefier, supply line and target cell. The gas storage tank has a volume of 1 m^3 and before operation the hydrogen in the tank is kept at 1400 mBar. The hydrogen is then passed through a compressor and liquifier down a supply line to the target cell located in the centre of the CB. The target cell, shown in figure 3.7, is a cylinder of kapton with the following dimensions: 125 μm thick, 10.03 cm long with a diameter of 4 cm.

The cell is positioned symmetrically around the beam axis (although there was a small 0.3 cm deviation from the centre of the CB in the current experiment). A 1 mm carbon fibre polymer (CFK) tube surrounds the target cell in order to maintain the beamline pressure. This tube is wrapped in thermally isolating foil of 8 μm of mylar and 2 μm of aluminium. The respective pressure and temperature of 1080 mBar and 20.5 K is monitored and adjusted using a computer control system. The values are kept constant by a balance of adding hydrogen from the storage supply and the operation of two 4 W heaters, one on the storage tank and one placed on

Figure 3.7: The liquid hydrogen target cell, consisting of a 10.03 cm cylinder of kapton surrounded by a 1 mm thick CFK tube. [61]

the target cell. An evacuated target is also used in order to record empty target background runs. These are analysed to help determine the number of reactions produced in the kapton cell and surrounding material.

3.5 Crystal Ball

The Crystal Ball [62, 63] (CB) was first commissioned as a high acceptance photon detector for use in e^-e^+ annihilation experiments at SLAC in the 1970s and used in early measurements of the J/Ψ particle. Since then the CB has been used to study both b-quarks at DESY in Germany and baryon resonances at Brookhaven National Lab (BNL), before being installed in the A2 hall in Mainz in 2002.

3.5.1 Crystal Ball Design

The CB is a highly segmented electromagnetic calorimeter comprising of 672 scintillators. The scintillators are arranged in the shape of an icosahedron, as shown in figure 3.8. The 20 major triangles are divided into 4 minor triangles, each holding 9 truncated triangular pyramids of NaI(Tl) scintillator. Due to the beam entry and exit holes there is a 4.6% loss of angular acceptance of the detector. The inner and

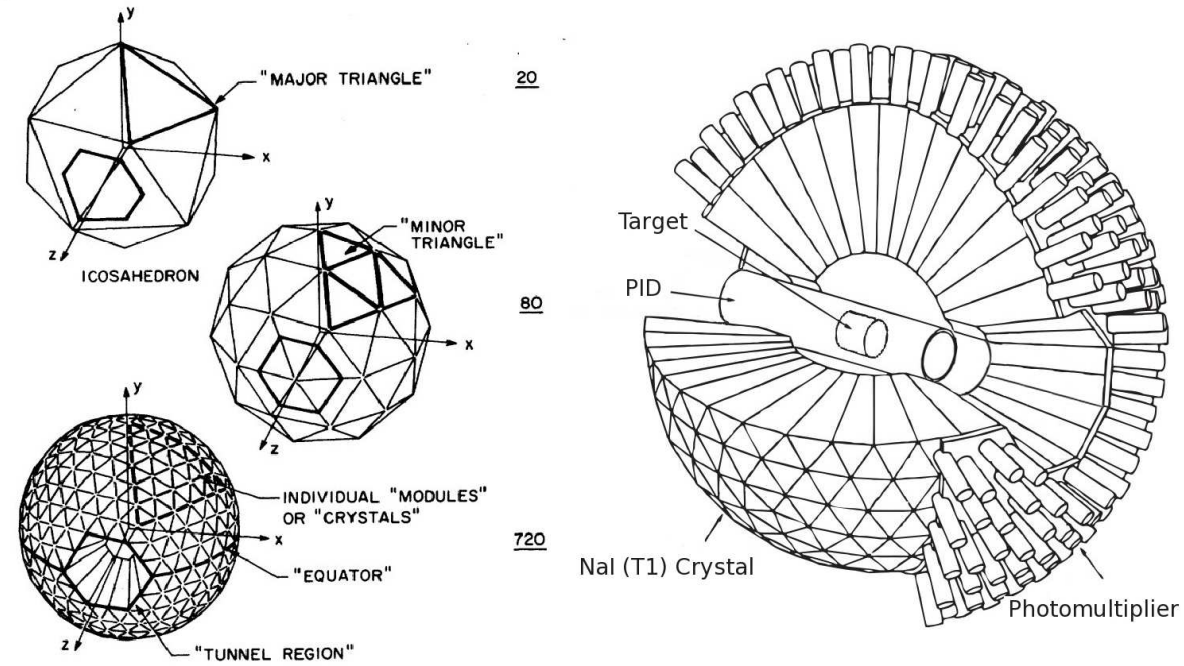

Figure 3.8: Sketch showing the Crystal Ball geometry. The entry and exit tunnel regions reduce the number of scintillators from 720 to 672. Right: taken from reference [62]. Left: taken from reference [63].

outer radii of the CB are 25.4 cm and 66 cm respectively, thus leaving space in the inner cavity for the target and supplementary detectors. Figure 3.9 shows a single crystal. The sides of the inner triangle are 5.1 cm with the outer sides measuring 12.7 cm. Each crystal is 40.6 cm in length, which corresponds to approximately 16 radiation lengths, 0.95 nuclear interaction lengths and 0.8 charged pion interaction lengths. In order to reduce optical cross talk between neighbouring crystals each crystal is wrapped in reflective paper and aluminised mylar. The scintillation light produced travels through a 5 cm air gap and glass window to reach an SRC L50 B01 photomultiplier tube, the signal from which is processed by the electronics described in section 3.8.1. NaI(Tl) crystals are hygroscopic and any water absorbed from the atmosphere can cause damage. Therefore, the crystals are hermetically sealed by steel plates into two individual hemispheres (see figure 3.10). There is a 0.8 cm equator region between the two hemispheres, which comprises a 5 mm air gap and two 1.5 mm steel plates. The equator region gives rise to a 1.4 % loss in

angular coverage, which along with the entry and exit holes leaves the CB with an acceptance of 94 % of 4π steradians. Table 3.2 summarises the angular resolutions and coverage along with the energy resolution for photons.

When a particle interacts with the NaI scintillator crystals an electromagnetic shower is induced, primarily through pair production, bremsstrahlung and annihilation. In the case of incident photons each shower typically deposits its energy in a cluster of several crystals. A cluster reconstruction algorithm is used to establish the energy and position information for the incident particle (see section 4.5 for a detailed description). Although the primary design goal of the CB was detection of neutral particles, i.e. photons from meson decays, it can be supplemented by other detectors such as the PID (see section 3.6) in order to provide charged particle detection capability.

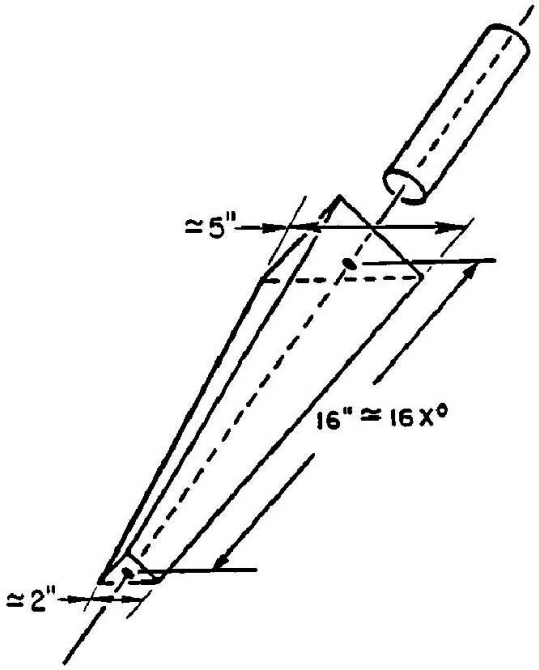

Figure 3.9: Sketch of a NaI crystal and PMT. Crystals are approximately 16 radiation lengths long. Taken from reference [64].

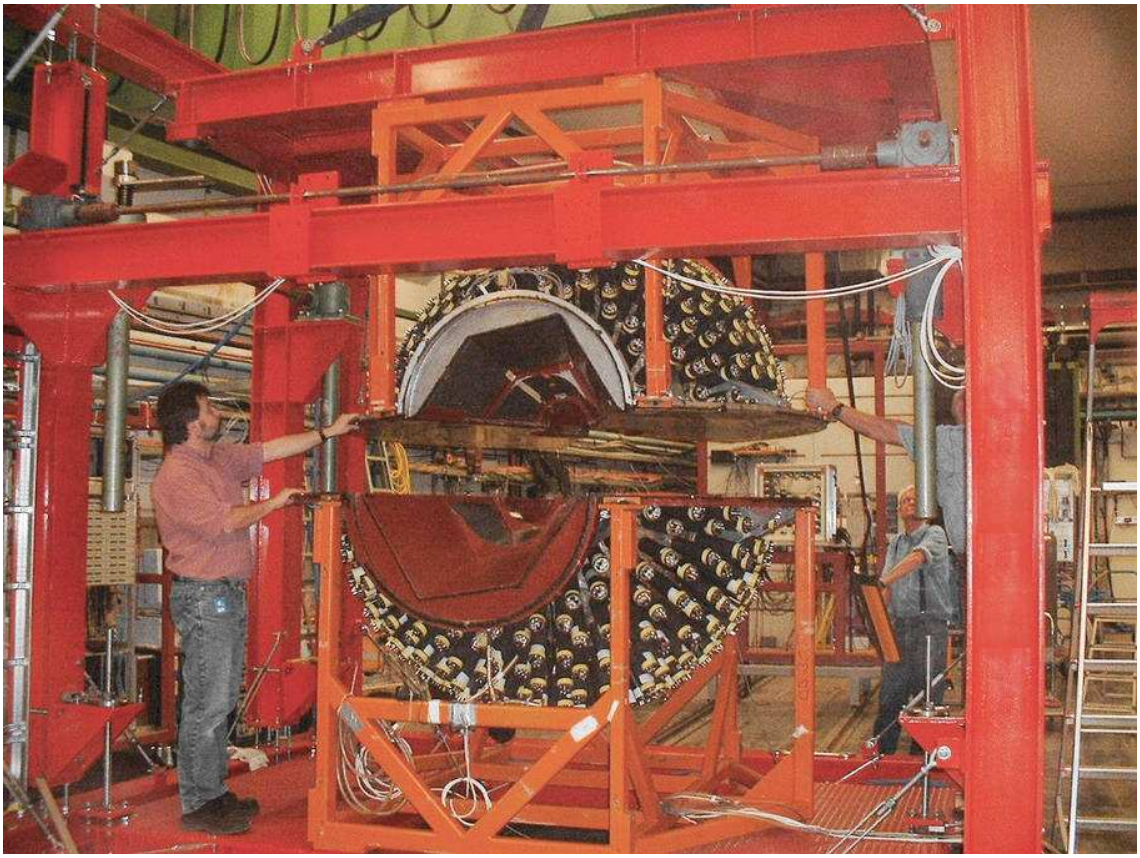

Figure 3.10: Photograph of Crystal Ball assembly in the A2 hall. The red steel plates hermetically seal off the two hemispheres. Taken from reference [65].

Angular Coverage	$0° \leq \phi \leq 360°$	(Azimuthal)
	$20° \leq \theta \leq 160°$	(Polar)
Angular Resolution	$\frac{2°}{\sin\theta}$	(Azimuthal)
	$\sim 2 - 3°$	(Polar)
Photon Energy Resolution	$\frac{\sigma}{E_\gamma}$	$\sim 1.7\%/\mathrm{E}_\gamma(\mathrm{GeV})^{0.4}$

Table 3.2: Crystal Ball parameters.

3.6 Particle Identification Detector

The Particle Identification Detector (PID), shown in figure 3.11, is a barrel of 24 EJ204 plastic scintillators which sits between the Crystal Ball and the target. Each scintillator is approximately 4mm thick, 13 mm wide, 50 cm in length and covers a

range of 15° in azimuthal angle (ϕ). The cross section of an individual scintillator is a trapezoid thus minimising the gap between scintillators when they are arranged together to form a 10 cm diameter barrel. The barrel covers 360° in ϕ and 20° - 160° in the polar angle (θ), which matches the angular acceptance of the CB. All scintillators are wrapped in a thin layer of aluminium foil in order to maintain optical isolation and a layer of black Tedlar (PVF) which light-proofs the whole of the barrel. A lucite light guide connects each scintillator to an individual photomultiplier tube (Hamamatsu H3164-10), the output from which is fed into electronics to record the charge and timing information.

As the distance between the PID and the CB is comparably small and the NaI crystals have relatively poor timing resolution, it is not possible to use Time-of-Flight (TOF) techniques for particle ID. Instead, charged particles are identified by comparing the energy deposited in the PID (ΔE) with the total energy deposited in the corresponding CB cluster (E). An example of a typical E-ΔE plot is shown in figure 3.12, the two regions of protons and charged pions can be clearly seen.

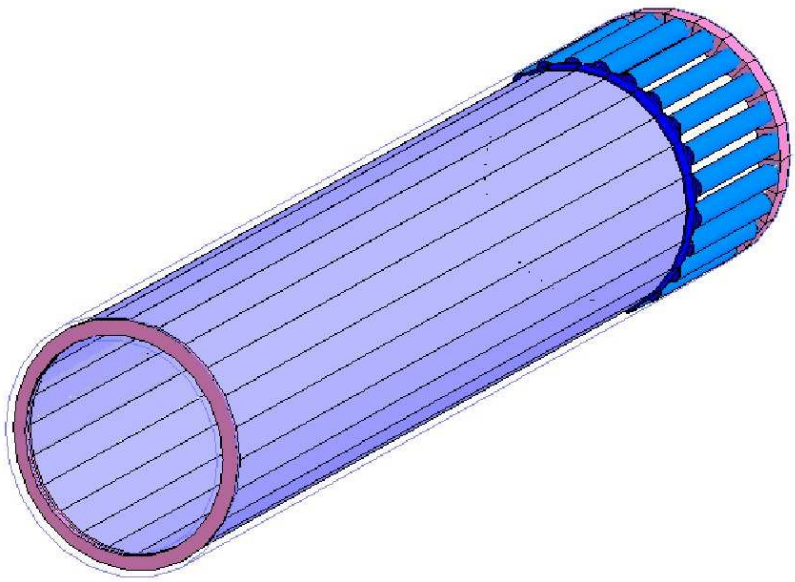

Figure 3.11: Geant 4 representation of the PID, showing the 24 plastic scintillators which comprise the 10 cm barrel, and the individual PMT connected to each scintillator.

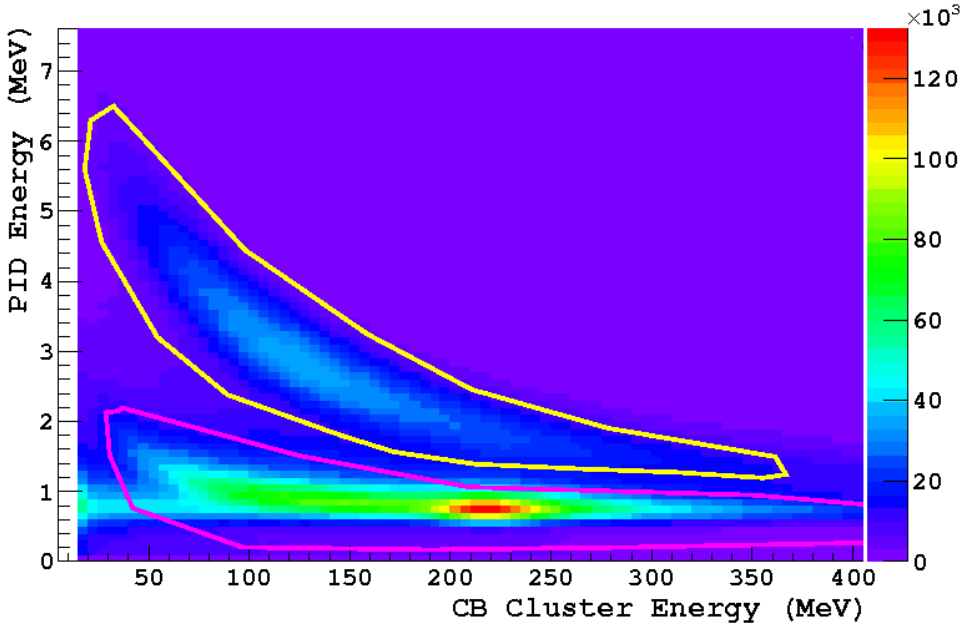

Figure 3.12: Energy deposited in the PID vs. CB cluster energy. The upper cut (yellow) selects protons and the lower cut (red) selects charged pions.

3.7 TAPS

The Crystal Ball was originally designed for colliding beam experiments; such experiments produce an isotropic distribution of particles. However, for experiments using a fixed target as installed in the A2 hall the reaction products are more forward focused, causing a significant loss of acceptance around the Crystal Ball front exit hole (0° - 20° polar angle). The TAPS detector [66], called so as it was originally split into several sections and operated as a Two/Three Arm Photon Spectrometer, has been rearranged as a forward wall and placed 1.5 m downstream of the target to cover the 5° - 20° polar angle region (as shown in figure 3.13).

3.7.1 TAPS Design

The TAPS hexagonal forward wall consists of 384 BaF_2 scintilators, each with an energy resolution of $\frac{\sigma}{E_\gamma} \sim 3.7\%/\mathrm{E}_\gamma(\mathrm{GeV})^{0.25}$. A diagram of a scintillator and associated components is shown in figure 3.14. Each crystal is 25 cm long, which cor-

responds to 12 radiation lengths, 0.83 nuclear interaction lengths and 0.68 charged pion interaction lengths. The cross section shape of the crystals is that of a hexagon on the side facing the incoming particles and a circle on the opposite side. UV proof PTFE with a thickness of 0.3 mm surrounds each crystal underneath a 15 μm thick layer of aluminum foil. Silicone grease is applied to the circular end of the scintillator and forms an optical coupling to a Hamamatsu R2059 photomultiplier tube, which in turn is attached to electronics that record charge and timing information (see section 3.8.5). BaF_2 has a lower scintillation light output than NaI(Tl) [67], however this is compensated for by its high density and higher atomic number. The scintillation light is produced in two components; fast and slow, with respective decay times of 0.6 ns and 620 ns and wavelengths of 220 nm and 620 nm. In front of each scintillator is a NE102A plastic scintillator charged particle veto detector [68]. A 5 mm thick optical fibre light guide connects each veto detector to an individual photomultiplier tube.

Although primarily designed as a photon spectrometer for neutral meson reconstruction TAPS can also be used for charged particle identification by one of a number of different methods. Due to the excellent timing response of the fast component of the scintillation light and the fact that TAPS is positioned 1.5 m downstream from the target, a time-of-flight technique can be used to differentiate light relativistic particles such as electrons and photons from heavier particles such as neutrons and protons. Furthermore, the scintillation response of the crystals allow pulse shape analysis to be performed. This is because different types of charged particle will deposit different amounts of energy in the scintillator's fast and slow components. It is then possible to select particles based on a ratio of charge in the slow and fast components. Finally, the plastic veto detectors produce a signal when a charged particle passes through and can be used simply to assign each particle as charged or neutral. It is also possible to compare the energy that the particle deposits in the veto to the energy in the BaF_2 scintillator using the E-ΔE technique previously described for the PID (section 3.6).

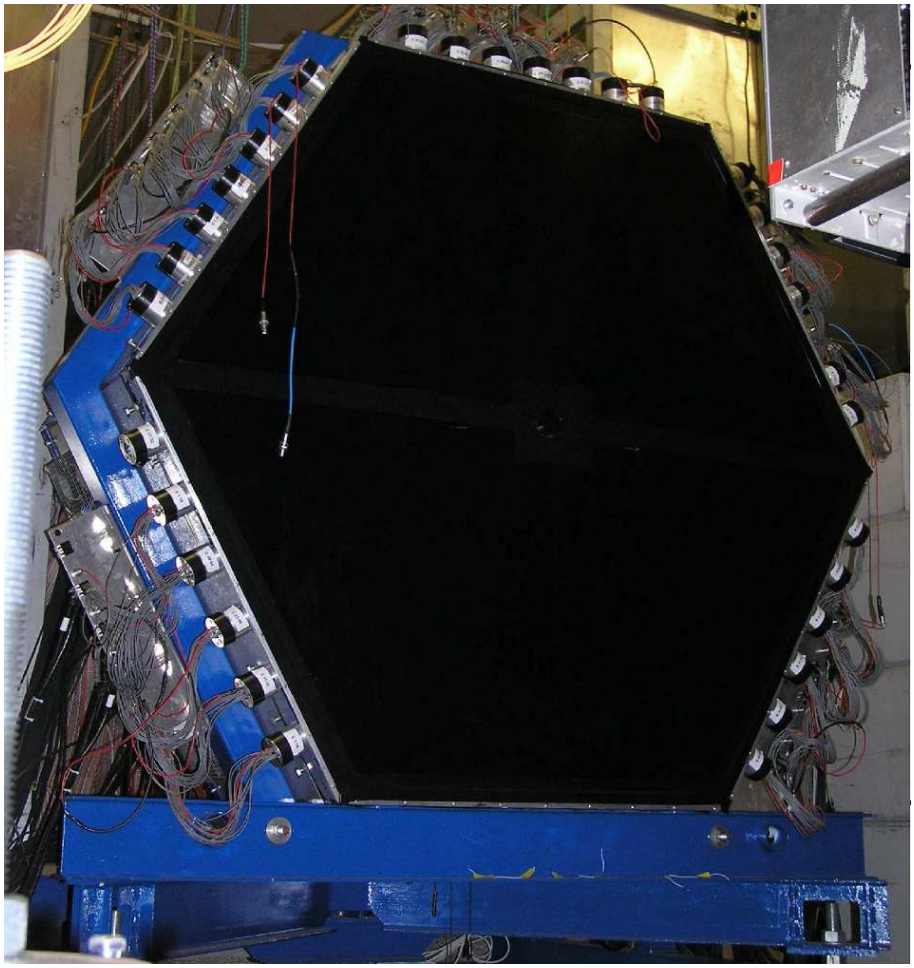

Figure 3.13: TAPS crystals arranged into a forward wall.

3.8 Data Acquisition System

The function of the data acquisition system is to record, process and filter the detector signals. This raw data can then be converted into kinematic information using the data calibrations described in chapter 4, from which the reaction products can be reconstructed. All the detector system PMTs produce an analogue signal which must be digitised. In the case of the energy deposited in each detector this is performed by a QDC (charge to digital converter). The signal from the PMT is integrated and the value assigned a QDC channel number, which is proportional to the energy deposited in the scintillator. If the analogue signal passes a discriminator threshold a TDC (time to digital converter) records a timing signal. TDCs require

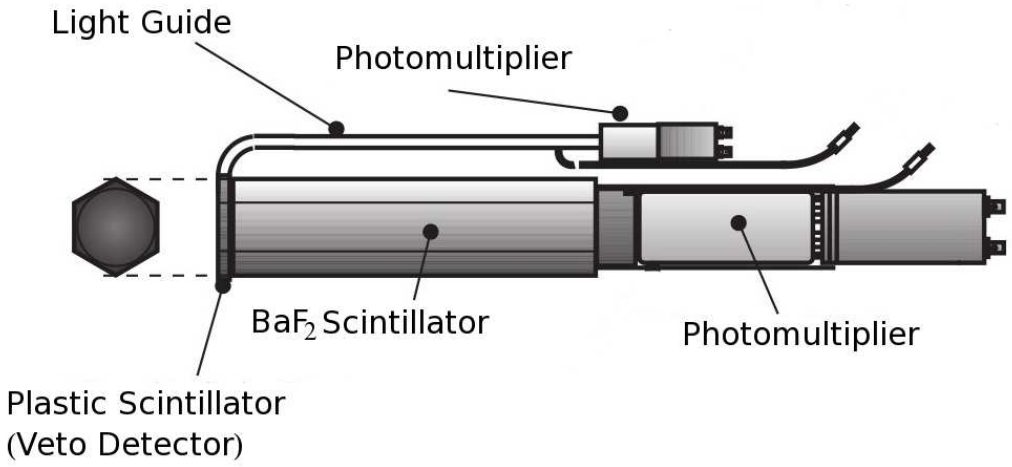

Figure 3.14: A diagram of a TAPS BaF_2 crystal and plastic Veto detector, each connected to an individual PMT.

both a start and a stop time and record this relative time difference rather than an absolute timestamp. Normally, the experimental trigger provides the start signal and the signal from the PMT provides the stop signal.

3.8.1 Crystal Ball Electronics

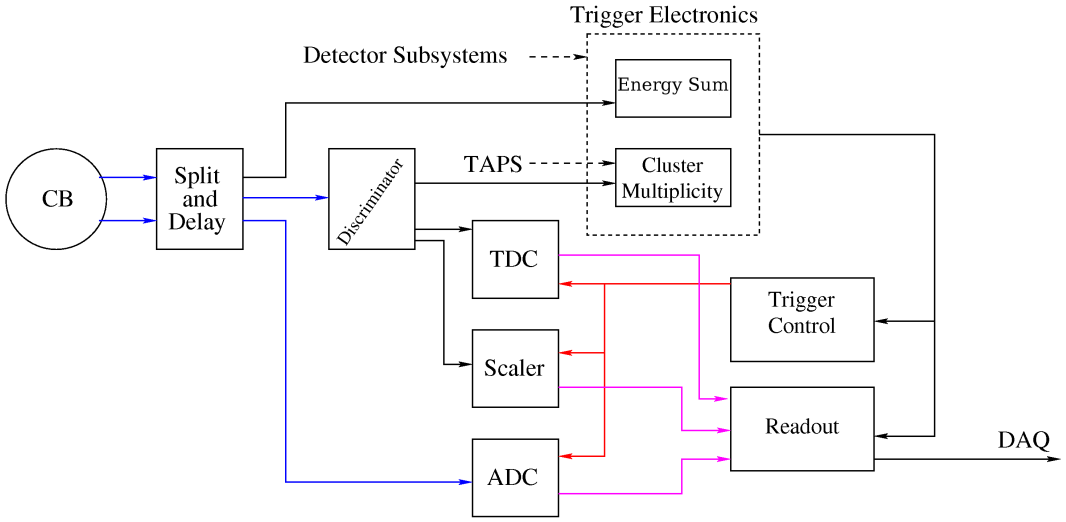

Figure 3.15: Crystal Ball electronics.

The diagram in figure 3.15 shows the layout of the Crystal Ball electronics. The

signal from each element's PMT is fed into a fan-in fan-out unit, with each unit handling 16 channels. The signal is then split into three: one signal is sent to a flash ADC (section 3.8.2) to measure the charge of the pulse [69]. The second signal is summed along with the other 15 signals within the fan-out unit and sent to the triggering electronics to measure the energy sum of all crystals (see section 3.8.6). The third signal is sent to a discriminator in which two separate thresholds may be set. If the low threshold is passed the signal continues to a CATCH TDC and scaler module. The high threshold is used to determine whether any of the crystals within the group of 16 contribute to the cluster multiplicity (detailed in section 3.8.6). If both of the trigger conditions are met the TDCs are stopped and both scalers and ADCs are read out and recorded by the DAQ.

3.8.2 Flash ADCs

Flash ADCs are used to convert the analogue signal from each PMT into a digital signal, from which the charge of the signal can be measured. This is done with a sampling frequency of 40 MHz. It is possible in principle with these devices to record the shape of the entire pulse. However, in order to reduce the dead-time of the system only the integral of the pulse is read out. The integral is measured over three different timing windows. The first window is set prior to the main pulse and records the residual charge in the ADC, which is known as the pedestal. Another two timing windows cover the signal and the tail region of the pulse. The pedestal value is dynamically subtracted from the signal on an event-by-event basis.

3.8.3 CATCH TDCs

Standard TDCs normally start counting on a signal from the experimental trigger and are stopped when a signal from the PMT passes a given trigger threshold. CATCH (Compass Accumulation, Transfer and Control Hardware) [70, 71] TDCs were developed to met the needs of the Compass experiment at CERN and operate using a slightly different technique. Each TDC has a free running continuous clock

which oscillates at a frequency of 10 GHz with a 117 ps/channel conversion rate. One TDC is set aside as a reference channel and is connected to the experimental trigger. When an event passes the experimental trigger conditions the oscillator value of the reference TDC is recorded. If any of the other TDCs record a hit the relevant oscillator value is stored. To obtain the timing information for each hit the reference TDC value is then subtracted from the oscillator value, and converted to a time using the 117 ps/channel conversion rate. The CATCH TDCs are able to record the oscillator values of several hits, with a timing resolution between two pulses of 20 ns, before the event is read out. The ability to handle multiple hits therefore reduces the dead-time of the system.

3.8.4 Tagger Electronics

The signal from each PMT of the tagger FPD is fed into an electronics card featuring an amplifier/discriminator and a coincidence unit, which produces an AND signal between neighbouring scintillators. If the signal is above the discriminator threshold it is then passed to a multi-hit CATCH TDC (see section 3.8.3) to record the hit timing. Additionally it is also sent to a FASTBUS scaler which records the total number of tagged electrons. This information is needed to normalise cross section measurements. The tagger microscope electronics use a similar setup. The signals from the PMTs are amplified before being fed through a QDC to a CFD, which if the threshold is met pass the signal to TDC and scaler modules.

3.8.5 TAPS Electronics

The TAPS electronics modules [72] are designed to each handle the output from four scintillator crystals. For each element the signal from the PMT is split into three. Two of these signals are sent to QDCs, with one measuring the charge of the fast component and the other the total charge. This allows pulse shape analysis to be performed as described in section 3.7.1. The third signal is passed to a constant fraction discriminator (CFD). If the threshold condition in this CFD is met a TDC

begins counting and is stopped by the experimental trigger. A CFD sets a threshold condition which is dependent on the size of the signal passing a certain fraction of the full pulse amplitude. This differs from the more common LEDs (leading edge discriminators), in which the threshold condition is based on an absolute value. Using a CFD eliminates any "timewalk"; meaning the timing of the pulse is no longer dependent on the pulse amplitude. This is important to fully take advantage of the excellent timing response of the fast scintillator component of BaF_2.

3.8.6 Experimental Trigger Electronics

When the charge and timing information from the detector systems are read by the DAQ and fed into the data-stream, the DAQ is unable to process any new detector signals leading to a period known as deadtime. In order to minimise this deadtime a series of trigger conditions are set. These depend on the reaction channels of interest and are used to pre-select suitable events at the hardware level. A pair of LeCroy LRS 4805 logic units are used to set two trigger conditions, both of which must be met for the DAQ to record the event. The energy sum of all 672 NaI scintillators in the Crystal Ball is determined. If this energy sum is greater than a certain value the first level trigger condition is passed. For the current experiment the energy sum threshold was set to 350 MeV. For the second level trigger the crystals of the CB are divided into regions of 16. If any crystal within a region has an energy greater than 20 MeV, the region is deemed to be hit. The number of such hits determines the multiplicity of the event. For the current experiment a trigger condition was set so as to only accept events with a multiplicity of three or higher (M3). It should be noted that the experimental trigger does not rely on information from the TAPS detector.

Chapter 4

Data Analysis: Calibrations and Event Selection

The previous chapter discussed the experimental run conditions, the detector setup and the associated readout electronics and data acquisition system. This chapter explains the stages involved in extracting events of a specific reaction channel from the raw data recorded by the acquisition system. Section 4.1 describes the simulation and analysis software. In order to convert the TDC and QDC values into meaningful timing and energy information the software must be provided with calibrations for the photon tagger, CB, PID and TAPS. These are detailed in sections 4.2, 4.4, 4.5 & 4.6 respectively. Sections 4.9 and 4.10 describe the two analysis methods used to select the $\gamma p \rightarrow \eta p$ reaction channel, the kinematic cut (KC) method and the kinematic fit (KF) method.

4.1 Analysis and Simulation Software

4.1.1 AcquRoot

Both data acquisition and analysis were performed using the AcquRoot software package developed by colleagues at the University of Glasgow [73]. AcquRoot, writ-

ten in the C^{++} programming language using the software libraries available in the ROOT toolkit [74], comprises of three parts: AcquDAQ, for data acquisition; AcquRoot, for online and offline data analysis; and AcquMC, a Monte Carlo event generator. AcquRoot processes the raw QDC and TDC data produced by AcquDAQ for each detector system, converting it into meaningful kinematic information of the detected particles. A user-specific physics reconstruction code is then used to perform analyses relating to specific reaction channels, such as the event selection techniques described in this chapter.

4.1.2 A2 Simulation

AcquMC creates pseudo-events to be used as an input for the Geant4 A2 simulation (section 4.1.2). The following reaction parameters can all be adjusted: the photon beam size, energy and distribution; the length, width and offset of the target and the type and number of reaction particles produced. The default setting uses a uniform beam energy distribution with a phase-space distribution of reaction products. It is however also possible to fold physics models into the distribution such as the photoproduction parametrisations from SAID (section 1.5).

A Monte Carlo simulation of the various detector systems in the A2 experimental hall, developed by colleagues at the University of Edinburgh [75], was written in C^{++} using the Geant4 software package [76]. Geant4 allows representations of the CB, PID, TAPS and target to be created, as shown in figure 4.1. The flight of particles generated in AcquMC are tracked, and as they pass through the detector materials, the physics interactions and decay processes are modelled. The response of the detectors is recorded and output files are produced containing the energy and timing information associated with each detector hit. The files can be input into AcquRoot and analysed using the same physics reconstruction software used for experimental data.

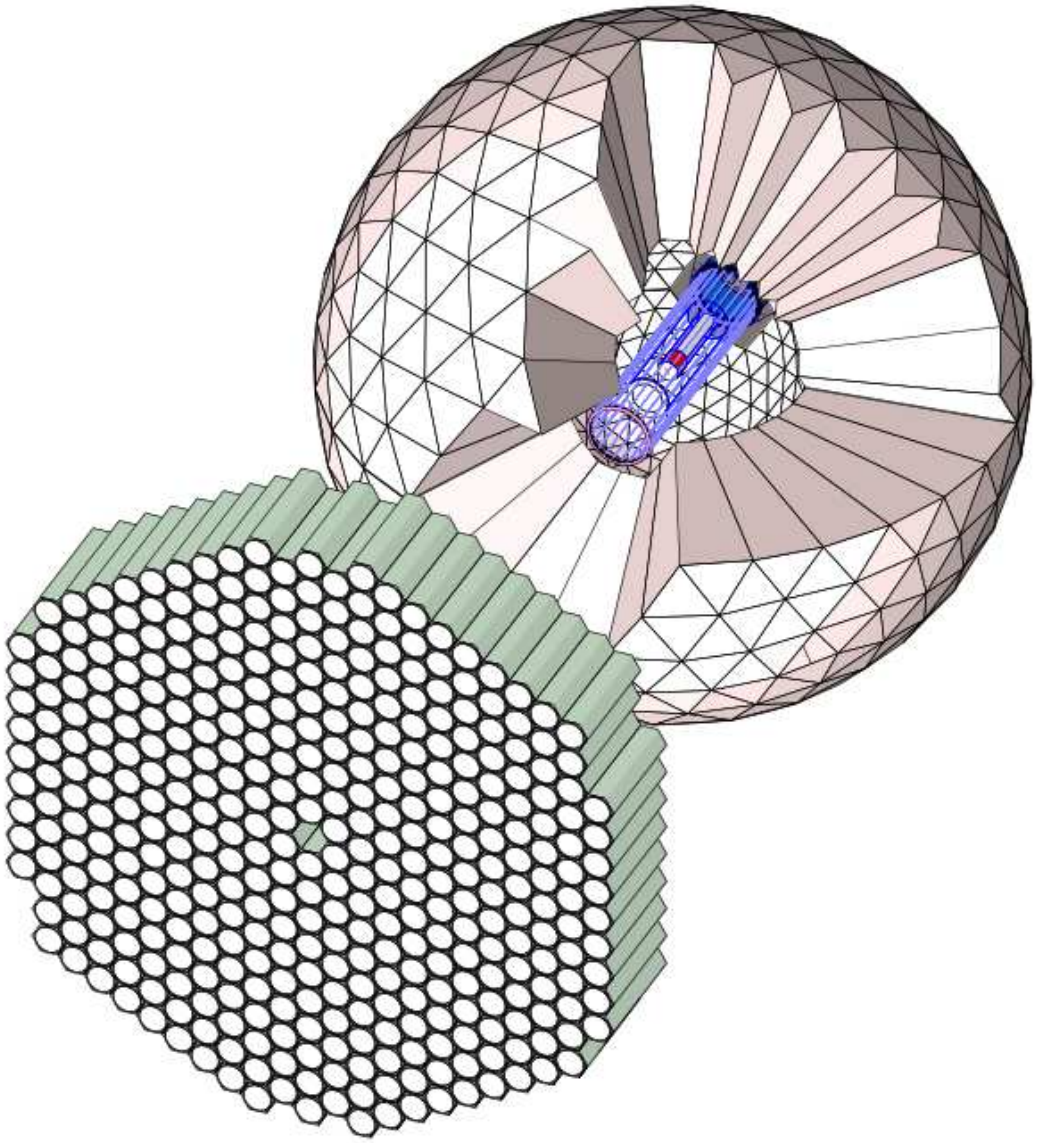

Figure 4.1: The detector setup within the A2 Geant4 simulation. The CB cut-out shows the PID and target inside.

4.2 Photon Tagger Calibrations

4.2.1 Energy Calibration

Extensive calibration measurements were performed after the tagger upgrade in 2007. The aim of the calibration is to convert tagger FPD channel number to electron energy, as described in detail by McGeorge *et al.* [58]. An accurate tool to use in calibration is the MAMI electron beam, as the energy is measured to an uncertainty of ±110 keV [50]. During these calibration measurements the radiator is removed and a low intensity electron beam is steered directly onto the focal plane detector elements. This was performed in 2007 for seven electron energies between 195.3 and 1307.8 MeV using the 1.834 T tagger field required to dump the beam at 1508 MeV. For each electron energy the beam is scanned through several tagger channels by varying the tagger field (by around ±5% of the dump field).

Using this technique it is possible to locate small triple overlap regions of three scintillators, the spatial positions of which are known very accurately. By plotting field strength against channel number it is possible to determine the fractional channel the electron would hit when using the standard dump field, the result of which is shown in the top of figure 4.2 for each of the seven electron energies. A computer program has been written in order to interpolate between the measured points [77]. The program assumes a uniform tagger field. This field is scaled based on the readings of the NMR probe from the specific experimental beamtime for which the calibration is being performed. The known dimensions and angles of the scintillators are used to produce the fitted line shown at the top of figure 4.2. However, there are small differences between the fitted line and the measured points, which are plotted in the lower part of figure 4.2. These differences are caused by non-uniformities in the tagger field due primarily to the effects of the pole shim mounting screws, added when the tagger was upgraded to cope with MAMI-C energies. A fit is performed to the points, the result of which is used as a phenomenological correction factor to the calibration.

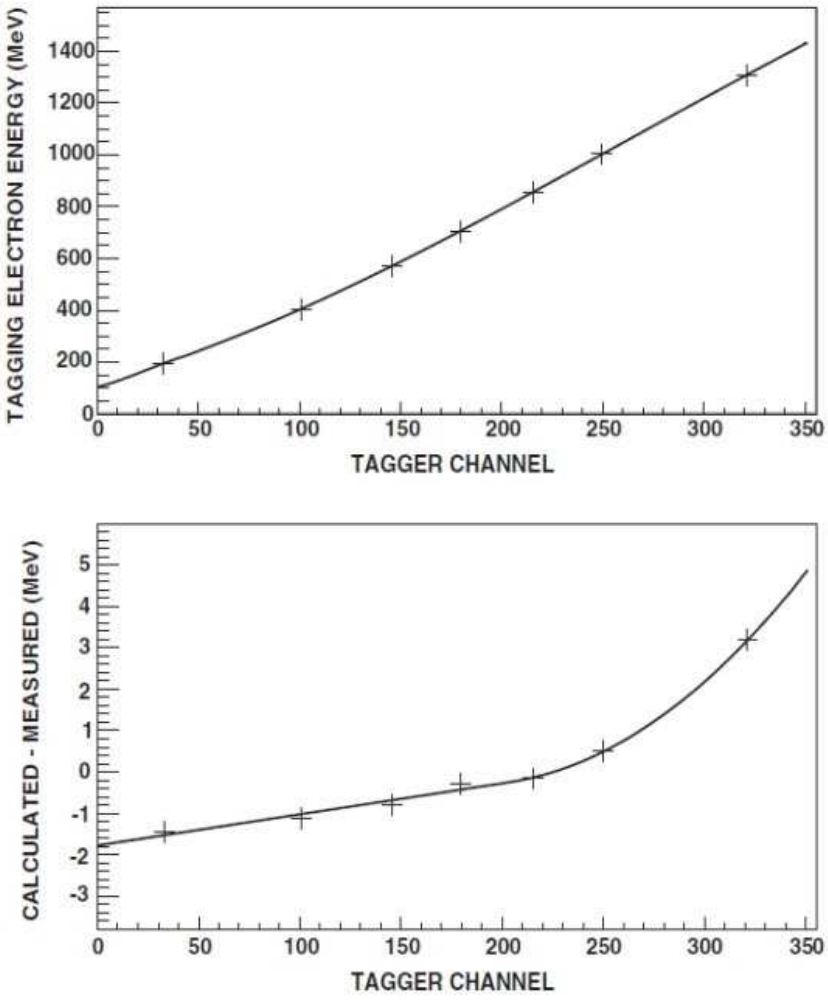

Figure 4.2: Tagger energy calibration plots, taken from reference [58]. Top: FPD channel hit positions for seven MAMI electron beam energies using a 1.834 T tagger field. Bottom: difference between measured values and fitted line due to field non-uniformities.

4.2.2 Random Coincidence Subtraction and Timing Alignment

It is advantageous to align all tagger TDC channels to a common value, thus enabling a single prompt peak cut to be applied to all tagger channels. This was performed using data from tagging efficiency runs, during which the CB was replaced as the experimental trigger by a near 100% efficient Pb-glass detector. At the low intensity

beam current used during the tagging efficiency runs, only a few random electrons are produced and the prompt peak dominates. This helps to simplify the alignment process, which a Gaussian fit is applied to the prompt peak for each channel. Adjustments are made to the timing calibration to align the mean of the Gaussian to the same TDC time for all tagger channels. Figure 4.3 shows a histogram of tagger hits against time for before and after the time alignment calibration. A similar timing alignment to the one described for the tagger was also performed on the CB, TAPS and PID TDCs.

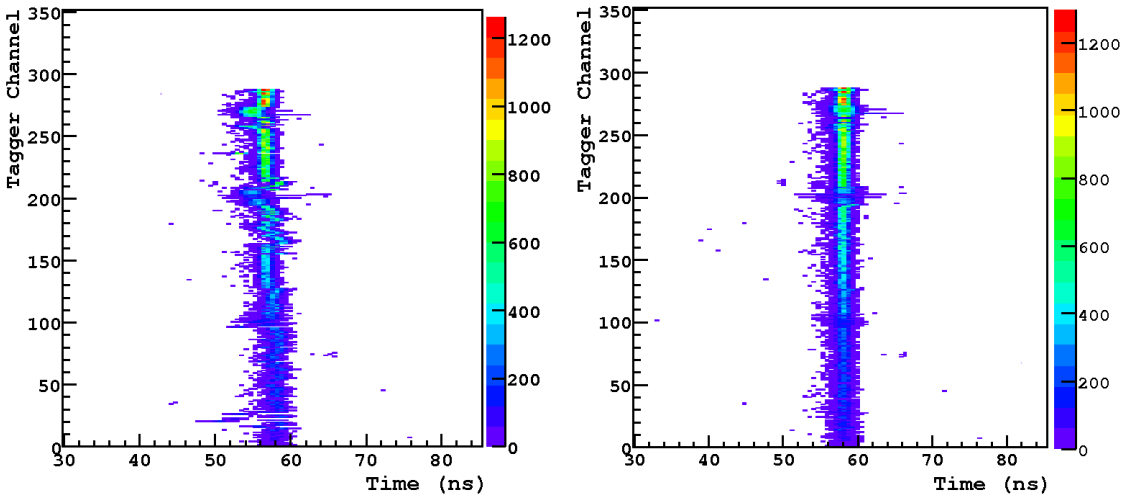

Figure 4.3: FPD hit distribution against time before timing alignment has been performed (left) and afterwards (right).

Not all electron hits recorded in the tagger will be associated with photons which induce a reaction in the target. This leads to the presence of a random background which includes contributions from photons lost due to the collimation of the beam, Møller scattering in the radiator and photons which passed through the target without interaction. In order to help select the electron hit that corresponds to the photon which induced the reaction detected downstream, the time difference between the experimental trigger and the TDC time of the detected electrons is plotted (figure 4.4). Photons which induce a reaction have a similar timing signal, which is associated with the time taken to travel from radiator to target and produce the detected reaction products. These events make up the prompt peak, which

sits on top of the flat random background. It is not possible to differentiate on an event-by-event basis whether a photon in the prompt region is a true prompt event that induced a reaction or simply a background event. Therefore, once all events in the data set have been analysed, a statistical random subtraction is performed. The kinematic variables which depend on photon momentum are reconstructed for all photons in the prompt region. In addition, a second sample is constructed using photons from the background region on either side of the prompt peak. In order to improve the statistical accuracy of the random sample, the region used is 4 times the time-width of the prompt sample. Distributions of variables created from the random sample are then scaled by a factor of 0.25 and subtracted from the distributions from the prompt region

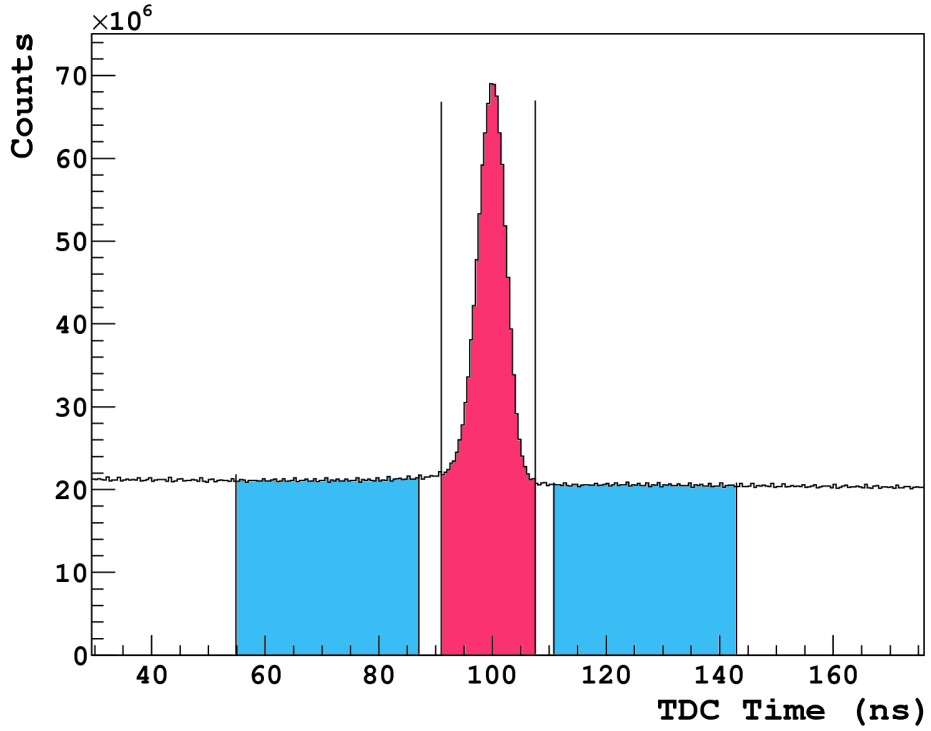

Figure 4.4: Time spectrum of the FPD TDCs. The central area shaded in red is the prompt region, whilst the blue shaded side bands represent the random regions.

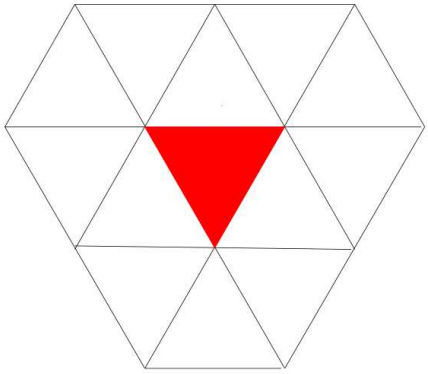

Figure 4.5: A typical photon cluster in the Crystal Ball, where each triangle represents a NaI crystal. The central red shaded crystal has the highest energy and is summed with the energy of each of the 12 neighbouring crystals to produce the total energy and mean position of the cluster.

4.3 Calorimeter Cluster Reconstruction

As a particle interacts with one of the A2 calorimeters it creates an electromagnetic shower of secondary particles. As both the CB and TAPS are highly segmented detector systems, the shower deposits energy into several neighbouring crystals. These groups of crystals are referred to as clusters. In order to identify clusters, the energy and position information of all crystals which fired in an event are passed through the clustering algorithm. This allows the energy and angular information of the incoming particle to be reconstructed in the analysis software. When a photon of around 100 MeV produces a shower in the CB, approximately 98% of the time the deposited energy is contained within a group of 13 NaI crystals, as shown in figure 4.5. In the clustering algorithm, the crystal with the highest energy is located and taken to be the central element of the cluster. The 12 neighbouring crystals are checked for any energy deposit above threshold, which is then added to that of the central crystal. The average photon energy resulting from $\eta \rightarrow 3\pi^0 \rightarrow 6\gamma$ decay for the current beamtime was approximately 100 MeV. Therefore any clusters with an energy less than 15 MeV are rejected as background events. The angular information of the photon can be determined from the reconstructed central cluster

position as defined by the weighted mean position:

$$\mathbf{r_m} = \frac{\sum_i \mathbf{r_i}\sqrt{E_i}}{\sum_i \sqrt{E_i}} \tag{4.1}$$

where $\mathbf{r_i}$ defines the Cartesian co-ordinate for the i-th crystal. For the range of photon energies in the current experiment the $\sqrt{E}$ weighting produces the most accurate position resolution, however in experiments with lower photon energies a log(E) weighting is used. The process is then repeated by searching for the next highest energy crystal not already included in a cluster, which is then selected to form the centre of the next cluster. This continues until all crystals have been analysed. The number of crystals per cluster for the CB and TAPS are shown in figures 4.6 and 4.7 respectively. Figure 4.8 shows the number of crystals per cluster in the CB as a function of the detected photon energy, whilst figure 4.9 shows the distribution of the number of clusters over all events.

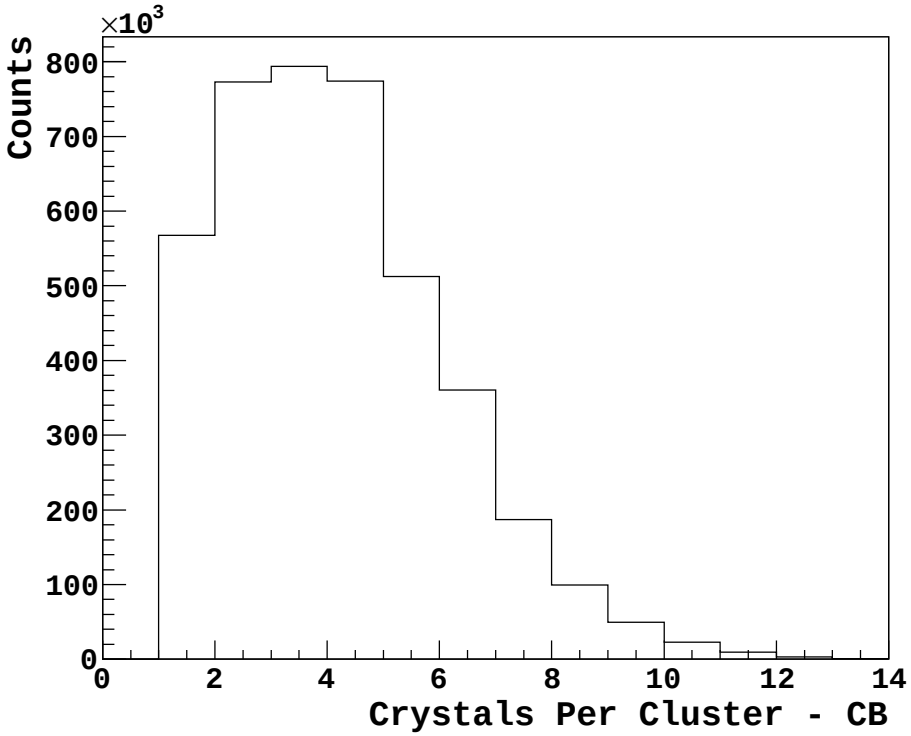

Figure 4.6: Number of crystals per Crystal Ball cluster.

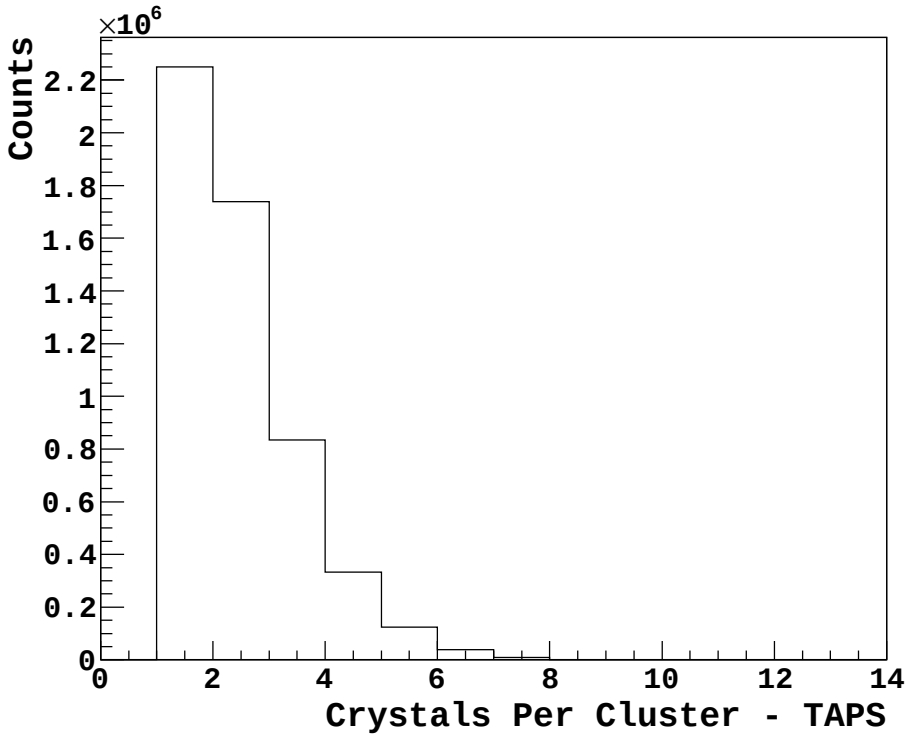

Figure 4.7: Number of crystals per TAPS cluster.

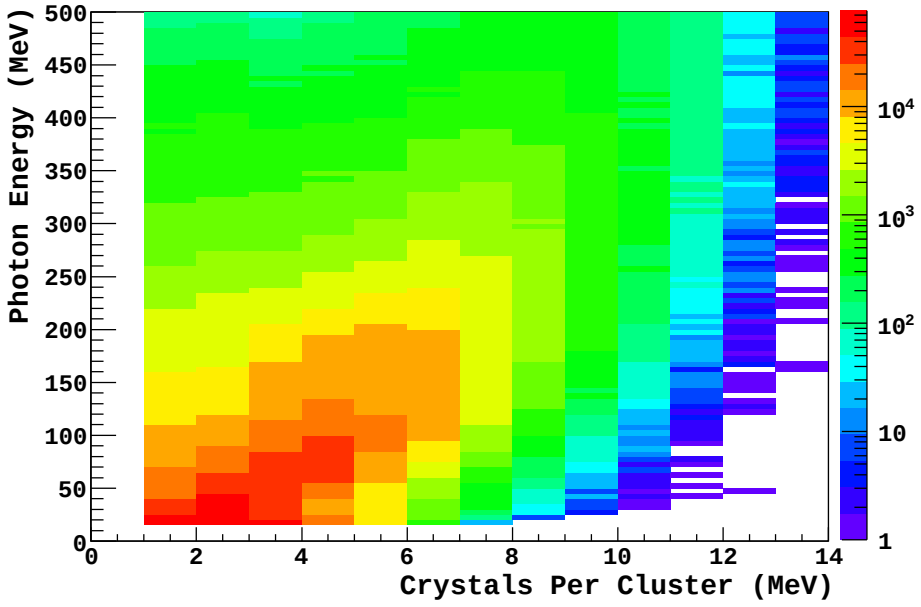

Figure 4.8: Crystals per CB cluster as a function of photon energy.

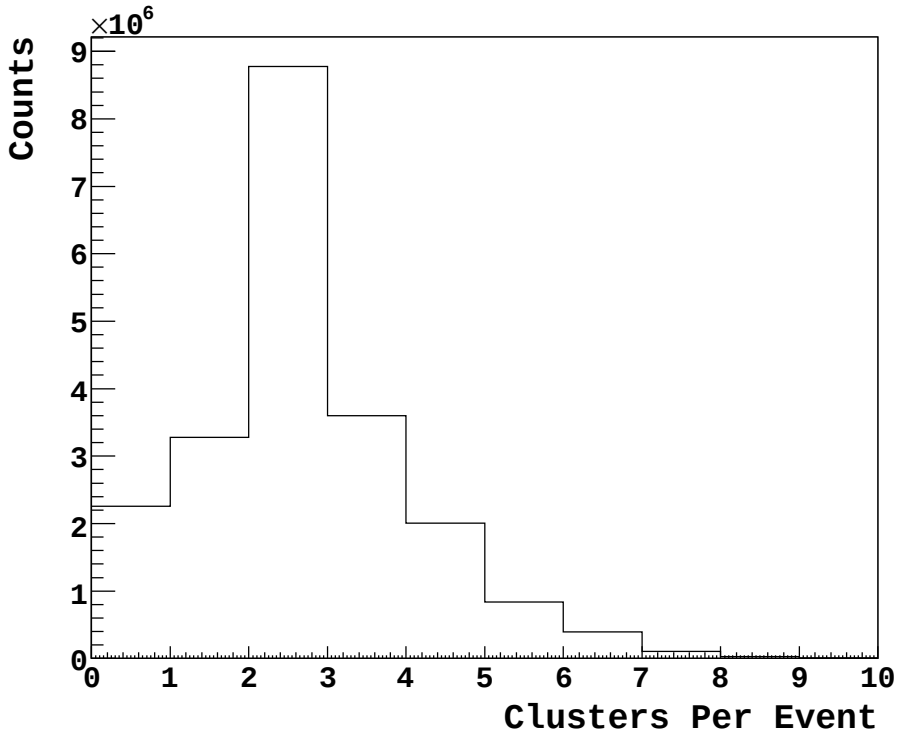

Figure 4.9: Number of clusters per event.

4.4 Crystal Ball Calibrations

A CB energy calibration is used to convert the recorded QDC value into the deposited energy for each crystal. In the energy range of the current experiment the scintillation light response for NaI(Tl) crystals is linear with energy, resulting in a simple linear relationship between QDC channel and energy. The energy calibration consists of two stages: a low energy hardware calibration performed before experimental running by collaborators at Mainz University and a high energy software calibration performed post-experiment by collaborators at UCLA [78].

4.4.1 Crystal Ball Low Energy Gain Calibration

During the gain calibration a mixed ^{241}Am/^{9}Be source is placed inside the CB. The americium decays via α-emission.

$$^{241}_{95}\mathrm{Am} \rightarrow ^{237}_{93}\mathrm{Np} + \alpha$$

The α particle interacts with the beryllium to produce an excited state of $^{13}C^{*}$, which in turn emits a neutron to leave an excited $^{12}C^{*}$ state. This decays to the ground-state of ^{12}C via the emission of a characteristic 4.44 MeV photon, which is then used as a common calibration point. The QDC spectrum for a typical crystal is shown in figure 4.10. The neutron background has been fitted with an exponential function and the photon peak with a Gaussian. The high voltage applied to each PMT is then adjusted to match the QDC position of the photon peak for all crystals.

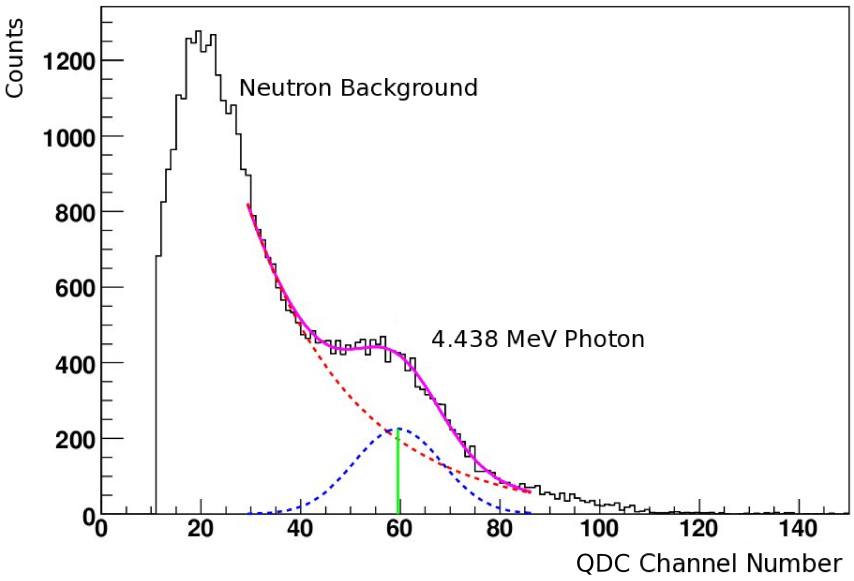

Figure 4.10: A typical QDC spectrum during CB PMT gain calibration. An exponential is fitted to the neutron background and a Gaussian to the photon peak, taken from reference [49].

4.4.2 Crystal Ball High Energy Calibration

Following an experimental run period, an offline high energy photon software calibration is performed based on analysing neutral pion photoproduction data. The pion decay, $\pi^0 \rightarrow \gamma\gamma$, provides a source of high energy photons that are suitable for calibration of the individual CB channels. Each photon produces an electromagnetic shower in the CB, depositing its energy in a cluster of crystals. For each event the

invariant mass of the two photons is reconstructed. The event is selected as suitable for use in the calibration if the following conditions are satisfied:

- The 2γ invariant mass must be within 30 MeV/c^2 of the π^0 mass (135 MeV/c^2).
- The incoming photon beam energy must be less than 180 MeV. This condition results in a large opening angle between the photon pair thus keeping the angular distribution as isotropic as possible to ensure an even sampling of crystals for the calibration.
- At least 70% of each photon's energy must be deposited in the central crystal of the cluster. This reduces the dependence of an individual channel calibration on the calibrations of neighbouring channels.

For each event where these conditions are met each CB channel software gain coefficient is adjusted to best match the 2γ invariant mass to the π^0 mass. As adjusting the gain on one crystal affects the calibration of many others, the process is performed several times until the results converge. For a more detailed description of both calibrations see reference [79].

4.5 Particle Identification Detector Calibrations

4.5.1 Particle Identification Detector Angular Calibration

The PID allows for the separation of charged and neutral particles in the CB by identifying angular correlations between charged PID element hits and CB clusters. It is therefore necessary to perform an azimuthal angular calibration, the details of which are now described. Initially events are selected in which clusters contain only one crystal, this helps ensure the clusters are the result of charged particles as larger cluster sizes are typically associated with photons. A further selection is applied to include events with only one hit in the PID, therefore reducing background contamination from events with multiple charged particles in the final state. Next, a 2D histogram of PID channel versus CB cluster azimuthal angle is plotted (left plot

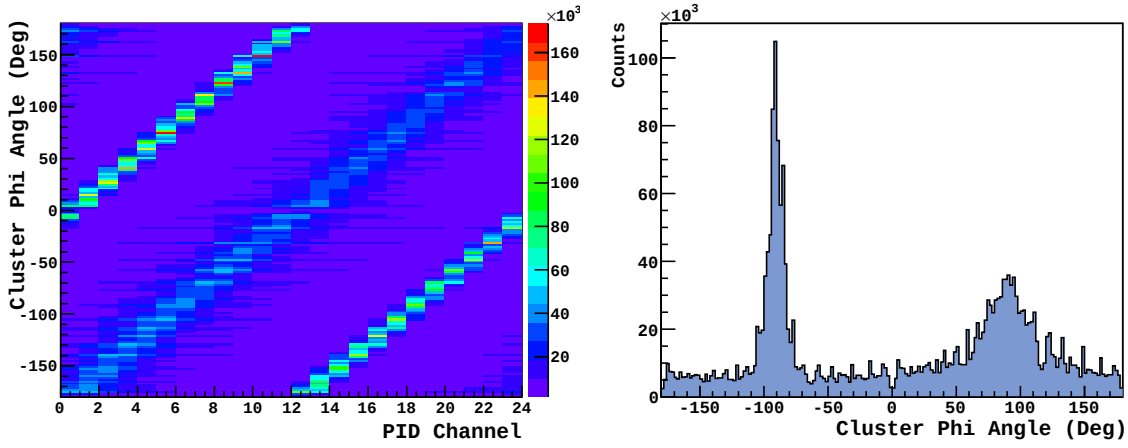

Figure 4.11: Left: PID channel hits versus coincident CB cluster ϕ angle. Right: projection of the CB ϕ angle for a single PID channel. The stronger peak represents the true correlation between the PID element and ϕ angle, while the weaker peak visible at 180° from the stronger peak represents background processes.

in figure 4.11). A projection of the CB azimuthal angle is then produced for each PID element (right plot in figure 4.11). The strong peak that is visible represents the true azimuthal coincidence between the PID channel and the CB azimuthal angle, with a weaker peak from background processes visible 180° from the strong peak. A Gaussian is fitted to the dominant peak for each of the PID elements, the mean of which defines the parameters used for the azimuthal calibration (figure 4.12).

4.5.2 Particle Identification Detector Energy Calibration

The PID can be used to differentiate between various charged particles using an E-ΔE technique, in which the energy deposited in a PID element is plotted against the energy deposited in the corresponding CB cluster. In order to calibrate the PID QDCs, the data from the current experiment were compared to results from the Geant4 A2 simulation. An example of an E-ΔE plot is shown in figure 3.12. Individual histograms are plotted for every PID element, with projections of the energy deposited in the PID taken using 10 MeV bins in CB cluster energy. Ex-

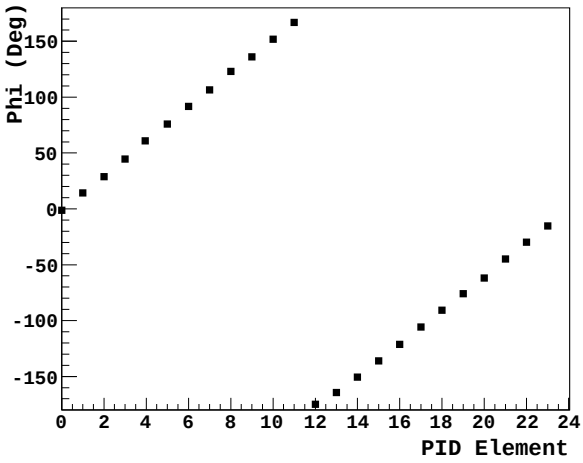

Figure 4.12: Results of PID azimuthal angular calibration. The position of each point is determined by the mean of a Gaussian fit to the peak on the right plot of figure 4.11.

amples of these projections are shown in the top and bottom right plots of figure 4.13 for simulated and experimental data respectively. The simulated plot clearly shows, from left to right, electron, pion and proton peaks. For each of these energy slices a Gaussian was fitted to the proton peak for both experimental and simulated data. The mean positions of the experimental and simulated Gaussians were plotted against each other as shown for a single PID element in the bottom left plot of figure 4.13. Losses in proton energy due to light attenuation in the NaI crystals are not modelled in the simulation. Therefore a correction must be applied to the simulated data (see reference [80] for a detailed description), which allows for a more accurate description of the linear correlation between experimental and simulated data. A linear fit is then applied to the graph of the Gaussian mean positions, the gradient of which gives the QDC energy calibration for that particular PID channel. Both PID calibrations were performed by colleagues at the University of Edinburgh [81].

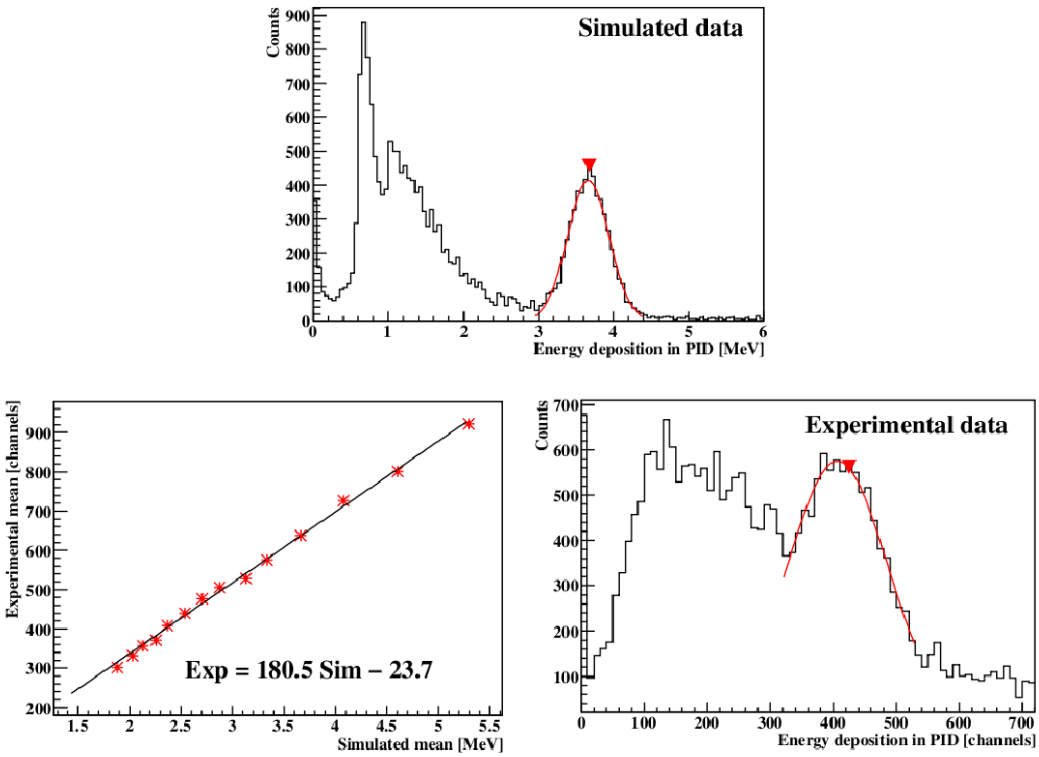

Figure 4.13: Example of energy calibration for a single PID element. Top and bottom right: energy deposited in the PID for the 70-80 MeV CB cluster energy projection. The right-most peak in these plots corresponds to protons, to which a Gaussian has been fitted to determine the mean position of the peak. Bottom left: Gaussian means are plotted against each other for each energy slice. A linear fit produces the energy calibration for the PID QDCs. Taken from reference [82].

4.6 TAPS Energy Calibration

The TAPS energy calibration was performed by colleagues at the University of Giessen [84]. As with the CB, the TAPS calibration also comprises a low energy PMT HV adjustment and a high energy software calibration. Cosmic rays provide an excellent low energy calibration reference point. The relativistic muons which make up the cosmic rays have an average ionising energy within a TAPS crystal of 37.7 MeV. A QDC spectrum for a typical crystal is shown in figure 4.14. The PMT

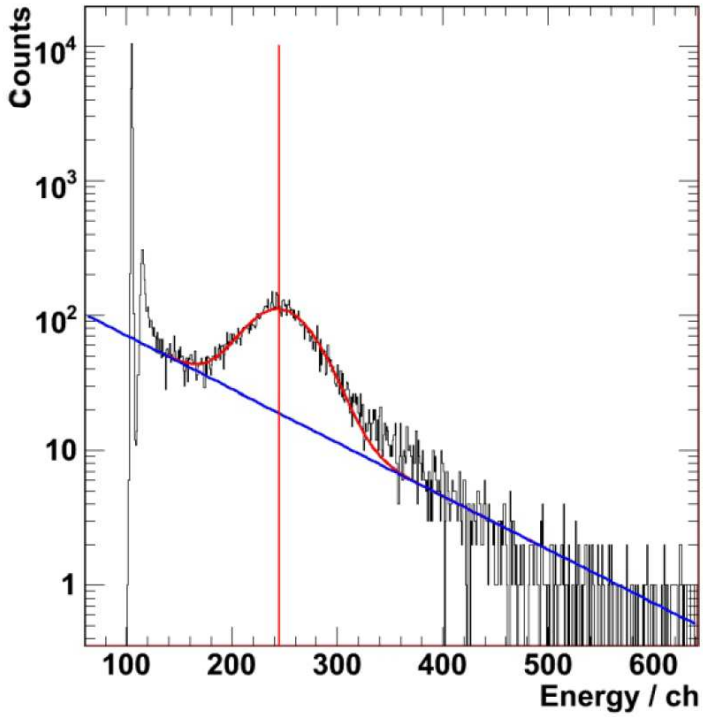

Figure 4.14: A typical QDC spectrum during low energy TAPS calibration. The red line marks the mean of the muon peak. Taken from reference [83].

gains were adjusted by changing their high voltages to match the mean position of this peak to a common QDC channel for all BaF_2 crystals.

The high energy software calibration for TAPS follows a similar process to that of the CB, as described in section 4.4.2. As before, the decay photons from neutral pion photoproduction are used in a software calibration procedure. Due to the limited angular coverage of TAPS, for which the polar angle range covers only 0 - 20°, events in which both decay photons strike TAPS are rare. Therefore events are used in which one photon hit is in TAPS and the other photon hit in the CB, meaning the TAPS calibration must be performed after the CB calibration. An in depth description is provided in reference [84].

4.7 Initial Particle ID

The first steps in the analysis procedure once all the above calibrations have been performed is the reconstruction of potential clusters in the CB and TAPS. The total energy, cluster size and reconstructed hit position of these clusters are determined using the clustering algorithm described in section 4.3. Before an attempt can be made to identify specific reaction channels, initial particle ID must be performed to assign a particle type to each cluster.

In front of each TAPS BaF_2 crystal sits a small plastic veto scintillator which registers a hit when a charged particle passes through. If the central crystal in the cluster has a corresponding veto hit the cluster is assigned as a charged particle, otherwise it is assigned as a photon. In order to differentiate between charged particles and photons in the CB, the ϕ angle of the clusters is compared to the ϕ angle of any PID hits. If the angles are comparable the cluster is assigned as a charged particle, otherwise it is assigned as a photon. Charged particles deposit a fraction of their energy in the PID before depositing the majority in the CB. If a histogram is plotted of CB cluster energy versus PID energy (the E-ΔE plot shown in figure 3.12) two characteristic regions can be seen. This is due to different particle types of the same kinetic energy depositing a different fraction of their energy in the PID depending on their mass. The upper curved region corresponds to protons whilst the lower region corresponds to charged pions.

4.8 Channel Identification Overview

In the reaction of interest, $\gamma p \rightarrow \eta p$, the two dominant neutral η decay modes are 2γ and $3\pi^0$. As the η and π^0 decay times are of the order of 10^{-19}s and 10^{-17}s, respectively, it is not possible to detect the η directly before it undergoes decay. Therefore, this experiment relies on selection of the η through the detection of the decay products of the $3\pi^0$ mode. As each π^0 decays via two photons this leads to a

six photon final state:

$$\gamma p \rightarrow \eta p \rightarrow 3\pi^0 p \rightarrow 6\gamma p$$

A preliminary analysis was performed using the $\eta \rightarrow 2\gamma$ decay mode, during which several advantages of using the alternative $3\pi^0$ mode were noted. Firstly, all six photon events pass the M3 multiplicity trigger used in this experiment thus eliminating the need for a simulation to correct for loss of detector efficiency due to trigger effects. Secondly, there is no software correction needed for the sizeable $\gamma p \rightarrow \pi^0 p$ background.

The reconstruction of particles used in the reaction channel identification relies heavily on several techniques in relativistic kinematics. For clarity the techniques specific to the present measurement are described in appendix A. Throughout the current analysis the invariant mass (IM) technique is frequently used to reconstruct and identify particles from their decay products. The invariant mass for a photon pair is shown below:

$$m_{2\gamma} = \sqrt{2E_1E_2(1 - cos\theta_{12})} \tag{4.2}$$

where E_1 and E_2 refer to the energy of the two photons and θ_{12} is the opening angle that the pair subtend. The IM distribution from two photons from the pion decay will therefore be centred on the pion mass, whilst the six photon IM from the η decay will be centred on the η mass.

The recoil proton is not detected directly by the calorimeter in the current analysis, but instead is reconstructed using the missing mass technique. The 4-vector of the η is determined from reconstructing the six decay photons, the incoming beam photon 4-vector is known from the corresponding tagger hit, and the target is at rest. This means that the 4-vector of the proton can be calculated according to

$$\mathbf{P_{proton}} = \mathbf{P_{target}} + \mathbf{P_{beam}} - \mathbf{P_{eta}} \tag{4.3}$$

Not all protons produced in reactions will be fully detected using the CB. This is due to the fact that high energy protons will punch through the NaI scintillators

without fully depositing their energy, whilst some low energy protons do not reach the CB due to energy losses in the PID and target. By using this missing mass technique the low proton detection efficiency is no longer a factor, thus allowing for an increase in the event sample for the analysis.

The next two sections describe in more detail the analysis procedures employed in the selection of $\gamma p \rightarrow \eta p$ events. Within the CB collaboration, collaborators from different institutions employ one of two distinct analysis techniques: the kinematic cut (KC) and the kinematic fit (KF) methods. In the KC method the kinematic properties of the reaction products are plotted and cuts are applied to select events whose properties fall within a given range. In the KF method the kinematic properties of the reaction products are compared using a least squares fit to a set of kinematic constraints which define the reaction channel. This fit additionally folds in the resolutions of the detector systems, leading to a single cut on the confidence level allowing events to be selected. A general mathematical description of a kinematic fitting is given in appendix B. As a check of self-consistency it was decided to perform the present analysis using both techniques.

4.9 Kinematic Cuts Analysis Method

A cut is made to select events containing six photon clusters in the CB and TAPS as possible $\eta \rightarrow 3\pi^0$ candidates. The six photon total invariant mass is shown in figure 4.15. There is a clear peak centred on the η mass of 548 MeV/c^2, although it sits on a significant background. In order to enhance the peak over the background, a sorting routine that uses more of the available kinematic information is used to loop over all combinations of possible photon pairs to select those which best reconstruct to a π^0. This sorting routine is performed as follows:

- Reconstruct 4-vectors for all six photon clusters
- Calculate the IM for each two photon combination involving these six 4-vectors
- Determine the mass difference between the π^0 PDG mass (135 MeV/c^2) and

the IM of each combination

- Order combinations from smallest to largest mass difference
- Select the best three combinations and assign them as pions only if mass difference is less than 20 MeV/c^2, otherwise reject the event

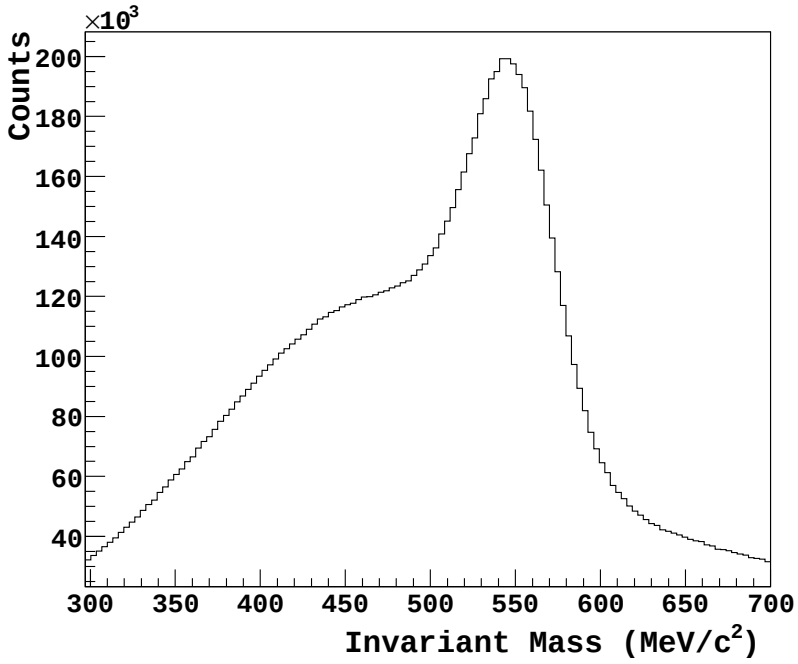

Figure 4.15: Total invariant mass of six photons. The peak around the η mass sits on a significant background.

The invariant mass of all three 2γ combinations is shown in figure 4.16. The three π^0 4-vectors are then summed together and the invariant mass of the summed 4-vector is determined, as shown in figure 4.17. The background under the η peak is now significantly reduced when compared to figure 4.15, allowing a 3σ cut to be applied to select η events.

Once the kinematic information of the η is determined it is possible to calculate the reaction missing mass for the event, as calculated from equation 4.3. The target proton is at rest in the lab frame and therefore its 4-vector is set as $P_{target} = (0, 0, 0, 938 MeV/_{c^2})$. E_γ is determined from the relevant photon tagger hit, allowing the beam photon 4-vector to be set as P_{beam} = (0,0,E_γ,E_γ). Because there are several

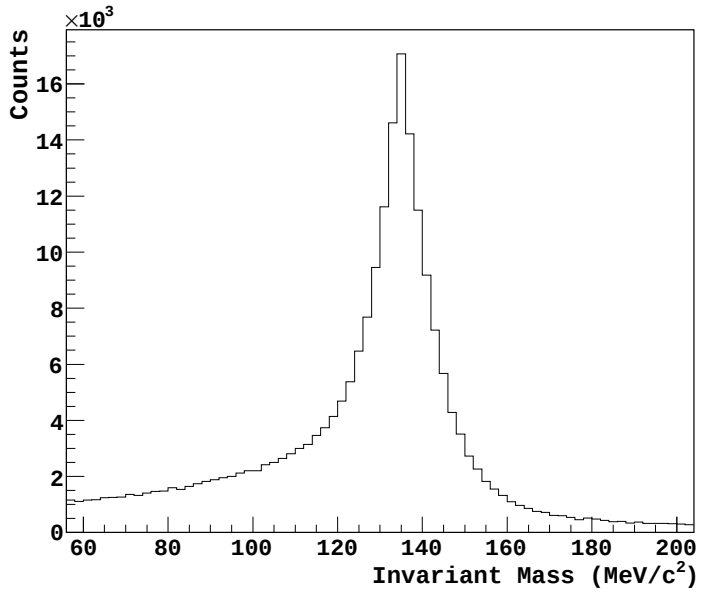

Figure 4.16: Invariant mass of all sorted 2γ combinations.

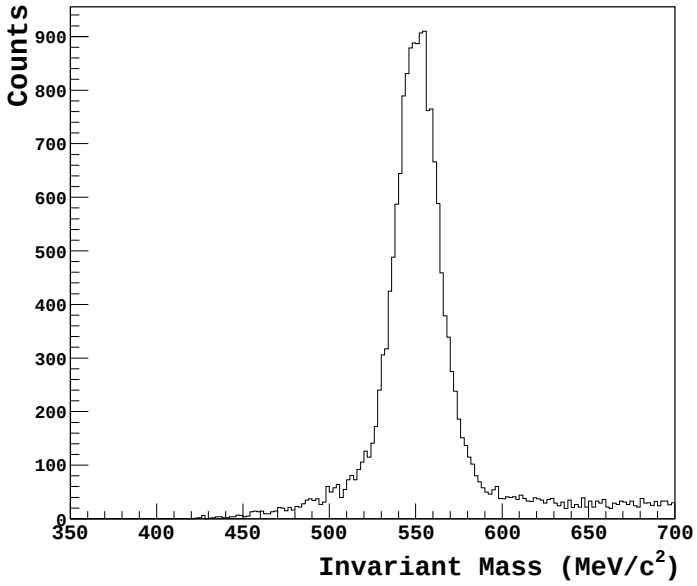

Figure 4.17: Total combined invariant mass of all three pion events. The background under the η peak is greatly reduced.

tagger hits in each event, the reaction missing mass must be calculated separately for the tagger hits that are defined as prompt and those defined as random (as described in section 4.2.2). Typical histograms of the missing mass for prompt and random

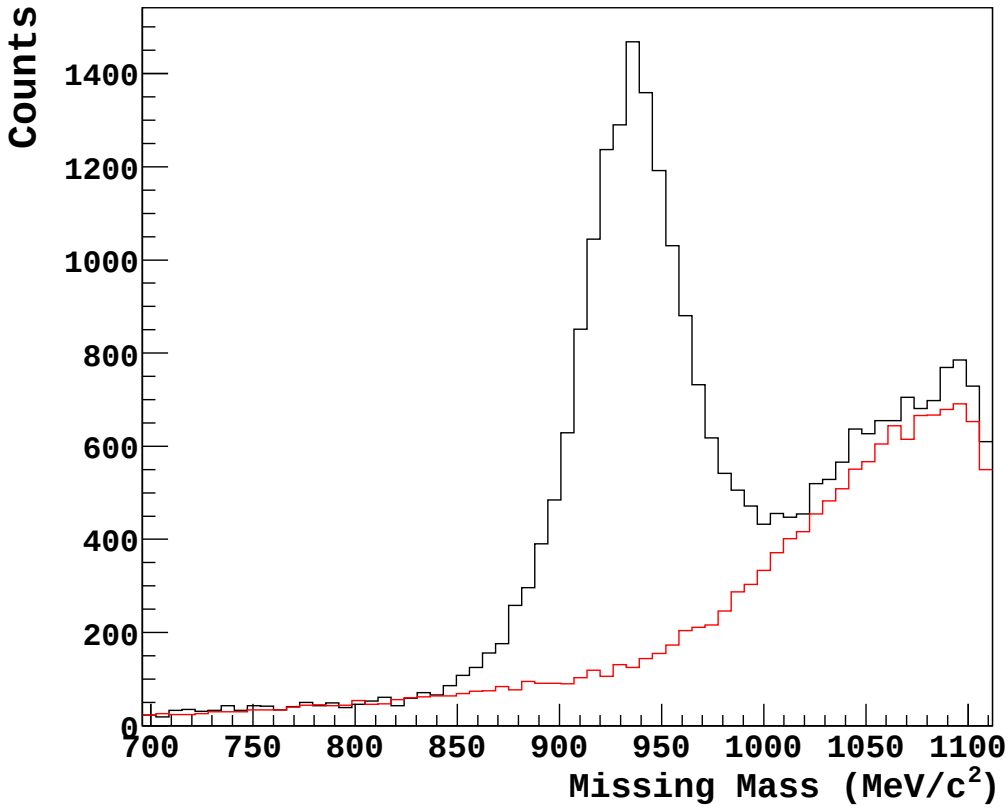

Figure 4.18: Missing mass ($E_\gamma = 1013$ MeV). Black: prompt events. Red: random events (scaled by 0.25).

tagger hits are shown in figure 4.18. A statistical correction based on the relative time-widths of the prompt and random regions is applied and subtracted. This leads to a corrected missing mass spectrum as shown in figure 4.19, in which a clear peak around the proton mass (938 MeV/c^2) can be seen. There remains, however, a background under this peak from other reaction channels (such as $\gamma p \rightarrow \eta p \pi^0$). In order to obtain a true reaction yield from these histograms, a 2nd order polynomial is fitted to the background and then subtracted from the peak. The effect of this final correction can be seen on the right plot of figure 4.19. The total integral of this corrected histogram then provides the experimental yield of the $\gamma p \rightarrow \eta p$ reaction.

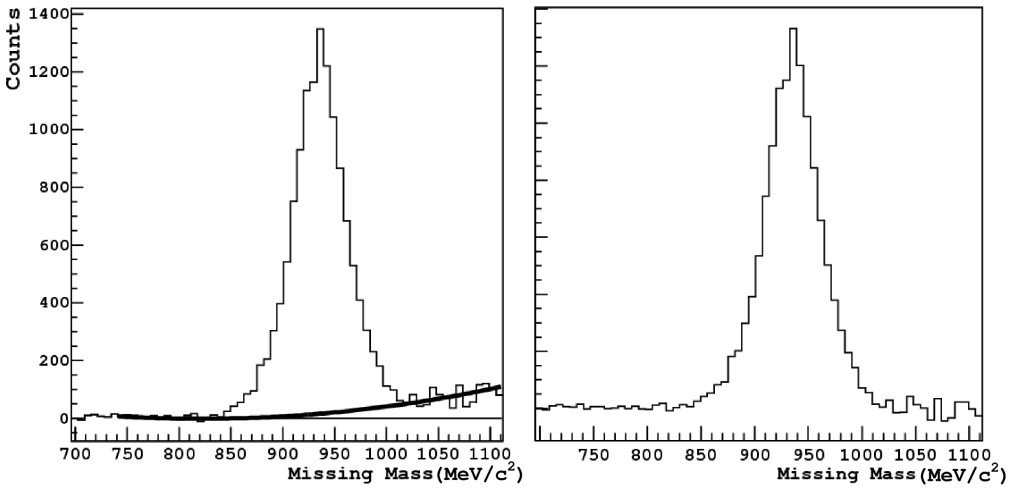

Figure 4.19: Missing mass background subtraction. Left: a 2nd order polynomial is fitted to the background. Right: background subtracted.

4.10 Kinematic Fit Analysis Method

In the kinematic fit analysis method a statistical fitting technique is used to compare the measured kinematic information of an event to a series of constraints while taking into account the uncertainties associated with the kinematic information. The kinematic fit analysis framework used in the present analysis was developed by colleagues at the University of Edinburgh [85]. It uses a method similar to the least squares minimisation of χ^2. The measured kinematic information is obtained from photon clusters detected in the CB and TAPS. The various constraints are defined by a series of equations: for example, the invariant mass of two photons must equal the π^0 mass. Finally, the uncertainties associated with the measured kinematic information are parametrised by the energy, θ and ϕ resolutions of the detector systems. A more rigorous mathematical description of the principles underlying kinematic fitting and the specific approach taken in the present analysis can be found in appendix B.

4.10.1 Generating KF Resolutions

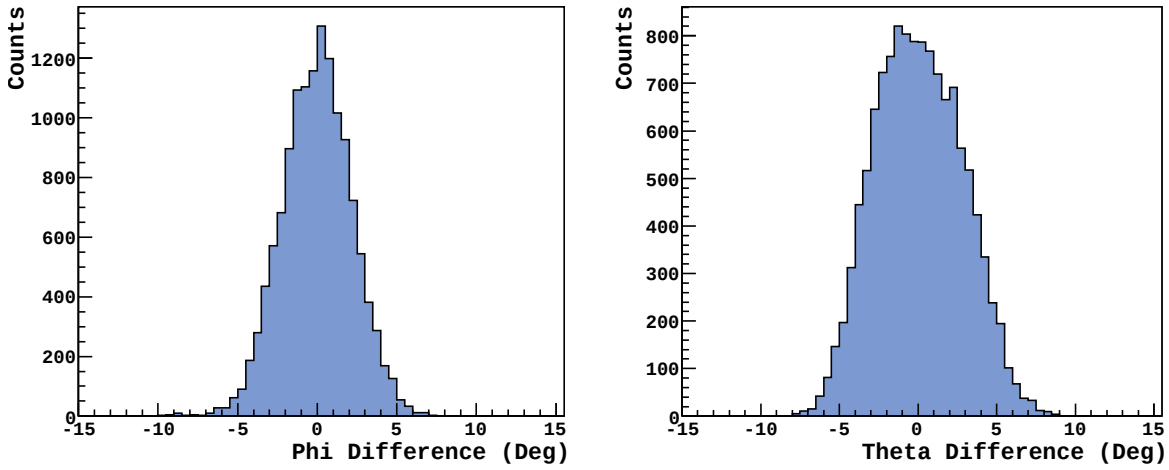

Figure 4.20: Difference in cluster angle between generated and analysed data for E = 280 MeV, $\theta = 60°$. Left: ϕ difference. Right: θ difference. The width of these distributions is a measure of the resolution.

The energy and angular resolutions of the CB and TAPS detectors were determined by generating single photon events over the full range of energies and angles then passing them through the A2 simulation, as described below. The difference between the generated and simulated energies and angles can then be used to determine the relevant resolutions. The resolutions have two contributing factors, the intrinsic resolution of the detectors and the experimental resolution. The intrinsic resolution is defined by the contributions from the photon's interaction in the Geant4 model of the detector systems and software reconstruction of the clusters. The experimental resolution is affected by several issues: pulse pile-ups, inefficient light collection in the scintillators, degradation in the PMT photo cathodes, PMT gain calibrations and pulse height to QDC channel conversion. As these latter factors are not taken into account in the simulation and vary with different experimental runs and beam conditions, an additional smearing correction factor must be applied to the energies extracted from the simulation. This is determined by matching the invariant mass widths of the production and simulated data.

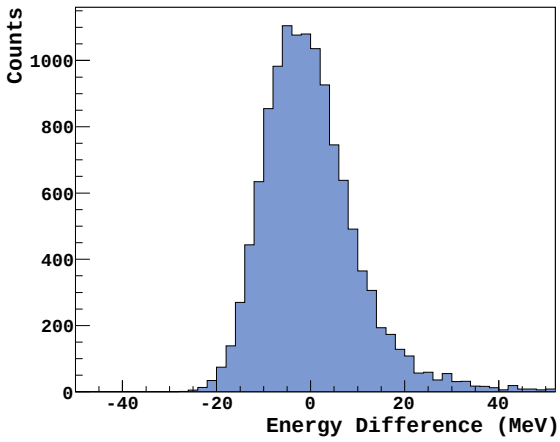

Figure 4.21: Difference in cluster energy between generated and analysed data. E = 200 MeV, $\theta = 80°$

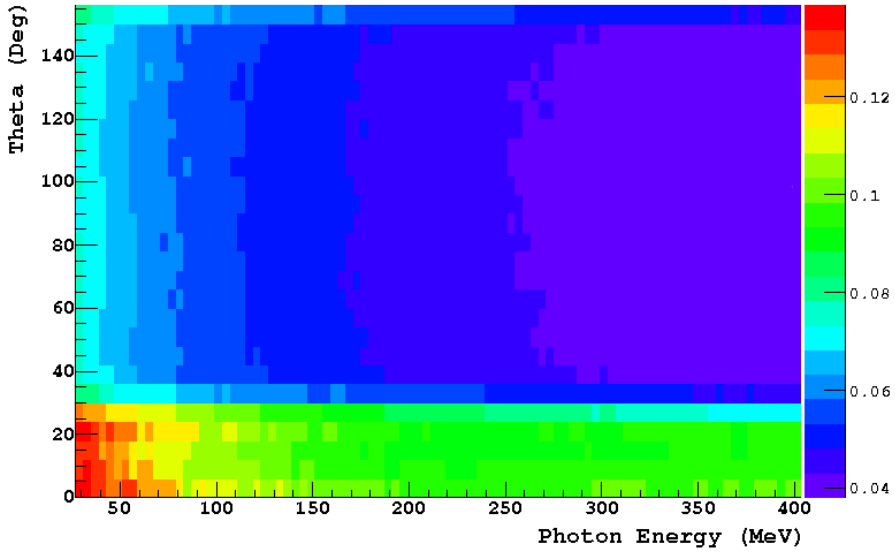

Figure 4.22: Energy resolution of the CB and TAPS as a function of energy and polar angle. The resolution is expressed as a fraction of photon energy.

In order to calculate the relevant resolutions, single photon events are generated with an isotropic angular distribution and a flat energy spectrum ranging from 5 to 1000 MeV. The vertex position of each event is assigned randomly within a volume representing the 10 cm long target cell. These events are then passed through the simulation, with the simulated detector hit information analysed in AcquRoot. For

each event the differences between the initial generated and final values of cluster energy, polar and azimuthal angles are calculated. All three resolutions vary with both polar angle and photon energy, though are independent of azimuthal angle. Examples of the angular and energy differences are shown in figures 4.20 and 4.21 respectively. In each (E, θ) bin the relevant difference distribution is fitted with a Gaussian, the width of which, characterised by the σ value, gives the resolution. These values are then used to assign the appropriate E, θ, and ϕ resolutions depending on the cluster hit information on an event-by-event basis when the kinematic fit is performed on the data.

Figures 4.22, 4.23 and 4.24 show the energy, polar angle and azimuthal angle resolutions and how they vary with E and θ. Each plot exhibits several features which are to be expected based on the nature of the CB and TAPS detector systems. The energy resolution is larger in the forward angle TAPS region, thus highlighting the better resolution achievable with NaI over BaF_2 as discussed in section 3.7. In both the TAPS and CB detectors a trend of improving resolution with increasing photon energy is observed. The θ dependence is most pronounced at the edge regions of the CB where the resolution worsens, but is broadly flat over the central region. This is to be expected due to the possible ambiguities in determining the cluster energy as photons in this region may not fully deposit their energy in the calorimeter.

In the case of the θ resolution one can see better resolution in TAPS compared with the CB due to the smaller TAPS crystals and its greater distance from the centre of the target. The CB θ resolution improves with increasing photon energy, due to the fact that the clusters spread over more crystals, making the determination of the shower centre more accurate. The cluster algorithm presumes the z-vertex for the interaction to be the centre of the target. This ambiguity has less of an effect on the calculation of θ for the forward and backward angles, which is confirmed in the plot by the improving of the resolution in these areas. Finally, the ϕ resolution plot shows the expected $1/sin(\theta)$ dependence for the CB, and an improving resolution with θ for TAPS.

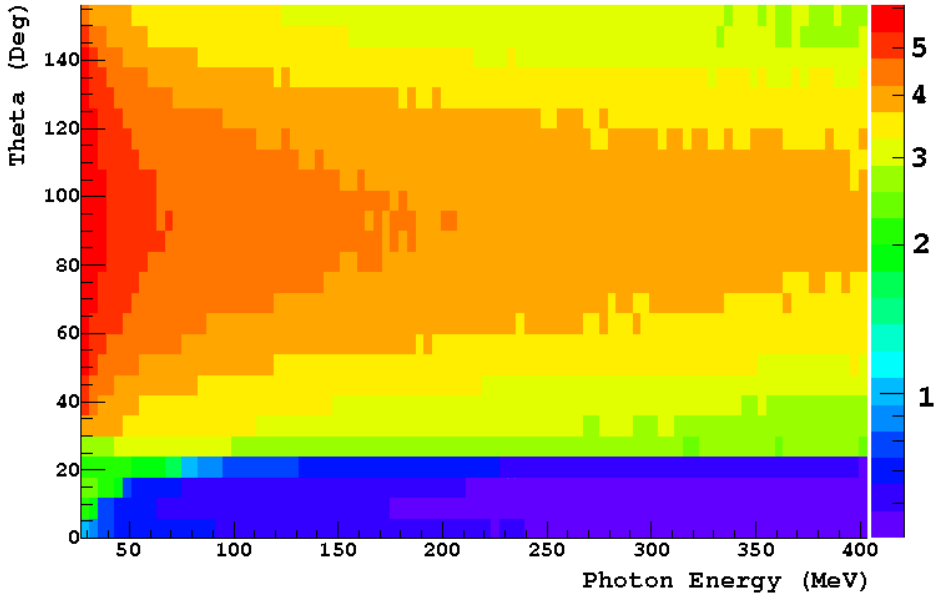

Figure 4.23: θ resolution (Deg) for the combined CB and TAPS detector systems.

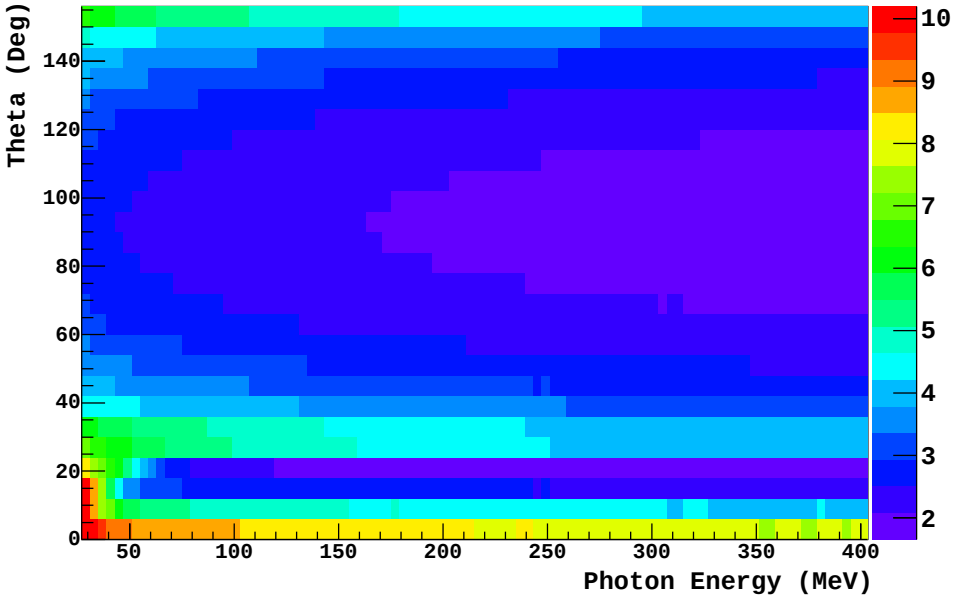

Figure 4.24: ϕ resolution for the combined CB and TAPS detector systems.

4.10.2 Kinematic Fit Event Selection

The kinematic fit analysis method follows much the same procedure as the KC method described in the previous section in terms of selecting and reconstructing six

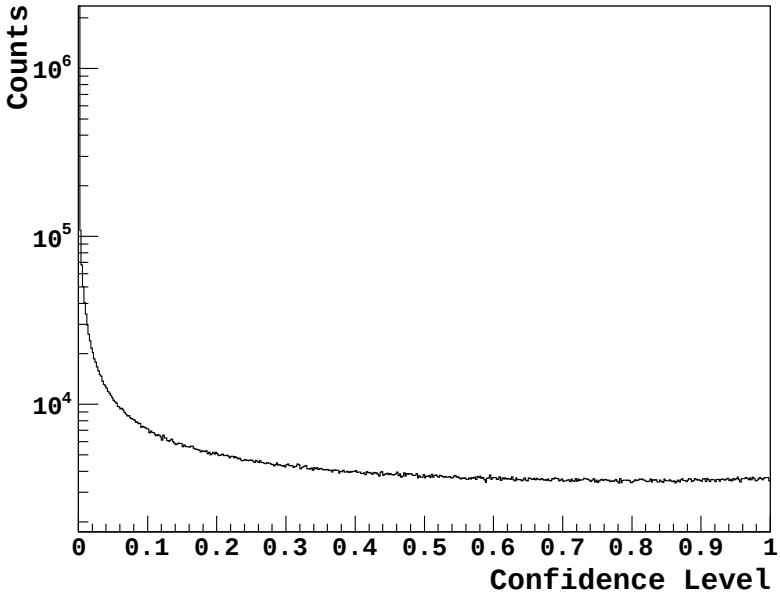

Figure 4.25: Confidence level of a six photon kinematic fit.

photon cluster events. The difference is that rather than perform cuts sequentially, a series of constraints to define the reaction channel are applied. This allows the $\gamma p \rightarrow \eta p \rightarrow 3\pi^0 p \rightarrow 6\gamma p$ reaction channel to be identified by performing this constrained fit and only accepting events that result in a good confidence level (CL) being returned from the fit. There are five Lagrange multiplier constraints applied in total:

- The IM of each of the possible permutations of three 2γ pairs is constrained to the π^0 mass
- The total IM of all six photons is constrained to the η mass
- The reaction missing mass is constrained to the proton mass

The kinematic fit can be split into two parts: the first associated with identification of an η, whilst the second is related to the missing mass constraint. Six photons arranged into three 2γ pairs results in 15 possible permutations, for each of which the π^0 constraint must be tested. First, each photon is assigned an uncertainty in θ, ϕ and energy based on the generated resolutions and reconstructed cluster parameters. The π^0 and η constraints are then applied and the fit performed for

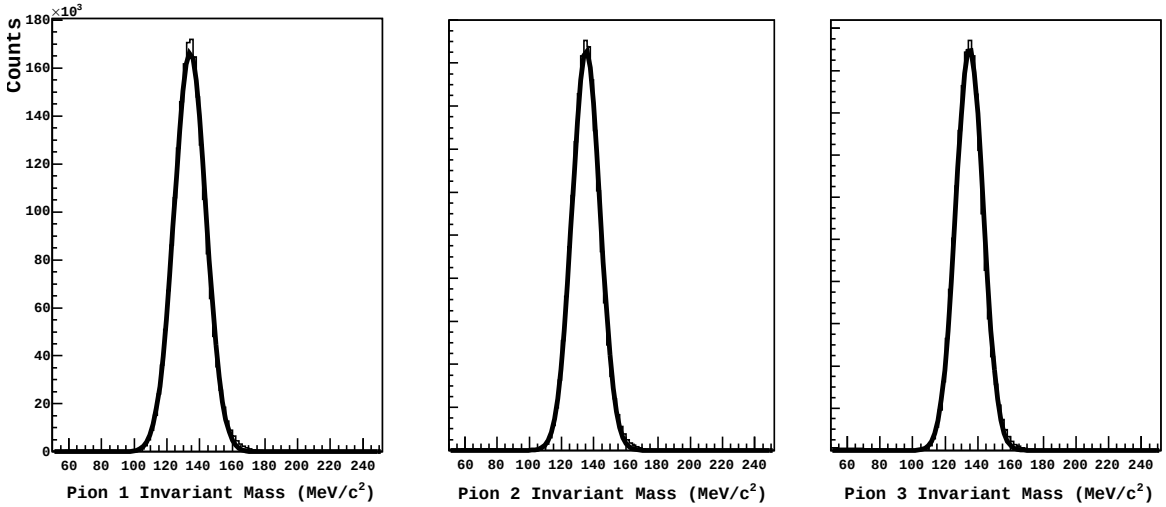

Figure 4.26: Invariant mass of three pions selected from the KF analysis method. Pion 1: $\bar{x} = 135.1$ MeV, $\sigma = 6.9$ MeV. Pion 2: $\bar{x} = 135.2$ MeV, $\sigma = 6.4$ MeV. Pion 3: $\bar{x} = 134.9$ MeV, $\sigma = 6.2$ MeV.

each pion permutation. If an event passes a 2% confidence level cut the event is selected as a possible η candidate, unless several permutations pass the CL test, in which case the candidate with the highest CL is chosen. A typical plot of the CL is shown in figure 4.25. After the CL cut has been applied it is possible to plot the invariant masses for each of the pion combinations (figure 4.26) and the total invariant mass of all six photons (figure 4.27). It should be clear from these figures that the KF method with a single CL cut provides a much cleaner selection of events than the KC method based of multiple cuts. It also results in a larger dataset as a result of considering all 2γ permutations in the KF method rather than just combinations in the KC method.

In addition to the π^0 and η constraints, a reaction missing mass constraint is also applied to the kinematic fit. As the missing mass is dependent on the beam photon 4-vector obtained from the tagger, it is necessary to perform the kinematic fit for every tagger hit in an event, applying a 2% confidence limit cut, and performing a random subtraction (as described in section 4.2.2). Two typical missing mass histograms, for different beam photon energies, obtained from the KF method are shown in figure

4.28. One can clearly see one of the main advantages of this method: there is no background subtraction necessary to extract the experimental yield. These events are then defined as arising from the $\gamma p \rightarrow \eta p$ reaction, allowing the reaction yield to be extracted by integrating the missing mass histograms.

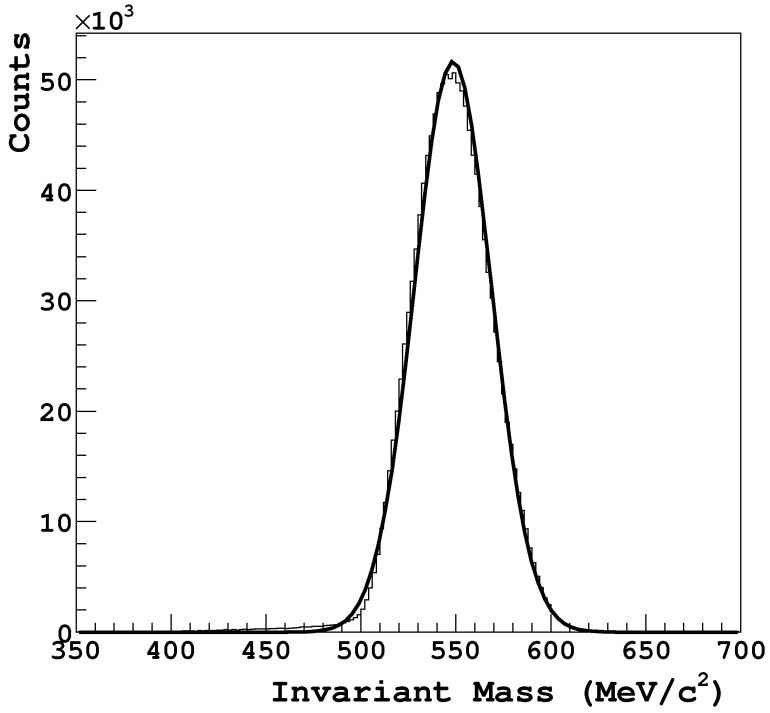

Figure 4.27: Invariant mass of all six photons after KF confidence limit cut. $\bar{x} = 548.3$ MeV, $\sigma = 20.2$ MeV.

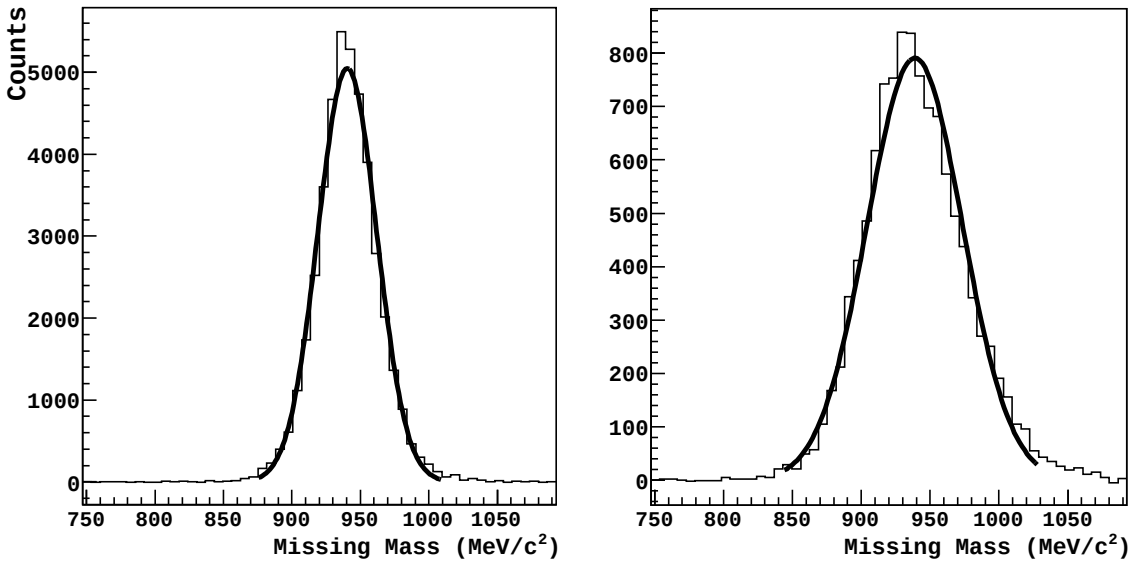

Figure 4.28: Two sample missing mass plots. Left: $E_\gamma = 933$ MeV, $\bar{x} = 939.1$ MeV, $\sigma = 21.3$ MeV. Right: $E_\gamma = 1189$ MeV, $\bar{x} = 938.8$ MeV, $\sigma = 34.5$ MeV.

Chapter 5

Data Analysis: Cross Section Extraction

This chapter presents the steps undertaken to produce a $\gamma p \rightarrow \eta p$ cross section measurement. First, the formalism of cross sections is introduced, and constant factors and η branching ratios presented. Next, the stages of η yield and photon flux extraction are presented in sections 5.2 and 5.3 respectively. The results of the acceptance calculation, which corrects for detector and software inefficiencies, are shown in section 5.4. The contributions from background processes, such as direct $3\pi^0$ events and ηp events not produced in the target, are then discussed in sections 5.5 and 5.6 respectively. Finally, section 5.7 describes the method of extracting the total cross section from the individual differential cross sections along with the angular information in the form of Legendre coefficients.

5.1 Cross Section Formalism

As introduced in section 1.3, a cross section is a measure of the probability of interaction and is expressed as an area, typically in units of barn (where 1 barn = $10^{-28}m^2$). Given the reaction $A + B \rightarrow C$, the general cross section is:

$$\sigma = \frac{N_C}{N_A \cdot \rho_B} \tag{5.1}$$

Where N_C is the yield of particle C, N_A is the total incoming flux of particle A and ρ_B is the number of particle B per unit area. For the reaction channel of interest $\gamma p \rightarrow \eta p$, N_C is the η yield, N_A is the photon beam flux and ρ_B is the liquid hydrogen target area density. A more specific formula for the differential cross section of the current measurement is given as:

$$\frac{d\sigma}{d\Omega} = \frac{N_{\eta\rightarrow n\gamma}}{A_{\eta\rightarrow n\gamma} \cdot N_\gamma \cdot \rho \cdot \Delta\Omega \cdot \frac{\Gamma_{\eta\rightarrow n\gamma}}{\Gamma_{total}} \cdot \varepsilon_{tagg}} \tag{5.2}$$

ρ	=	liquid hydrogen target area density
$\frac{\Gamma_{\eta\rightarrow n\gamma}}{\Gamma_{total}}$	=	η decay mode branching ratio
$\Delta\Omega$	=	2 $\pi\Delta$ (cos(θ_{cm})), solid angle interval
$N_{\eta\rightarrow n\gamma}$	=	η yield in $(E_\gamma, cos(\theta_{cm}))$ bin
N_γ	=	total photon flux in E_γ bin
ε_{tagg}	=	tagging efficiency in each E_γ bin
$A_{\eta\rightarrow n\gamma}$	=	acceptance in $(E_\gamma, cos(\theta_{cm}))$ bin

Given a target length of 10.03 cm the target area density was calculated to be $4.243\times10^{-7}\mu b^{-1}$. The branching ratio for the $\eta \rightarrow 3\pi$ decay mode is 32.56±0.23% with the resulting $\pi^0 \rightarrow 2\gamma$ decay mode given as 98.798±0.032%. Therefore the overall branching ratio for the 6γ final state is 31.39±0.22% [14]. The E_γ bins correspond to the width of each tagger channel, which at an electron beam energy of 1557 MeV, range from 2 MeV at the maximum tagged photon energy of 1447 MeV to 4 MeV at the ηp threshold of 707 MeV. However, in the field of nucleon resonances spectroscopy it is more useful to convert E_γ to the centre of mass energy, W.

$$W = \sqrt{(M_{proton} + E_\gamma)^2 - {E_\gamma}^2} \tag{5.3}$$

5.2 $\gamma p \rightarrow \eta p$ Yield Extraction

The ultimate goal of the calibration and analysis procedures outlined in the previous chapter is the determination of the experimental yield for the $\gamma p \rightarrow \eta p$ reaction. In

order to make meaningful comparisons with theoretical models, this yield must be first transformed into the centre-of-mass system and then extracted for different bins in W and $\cos(\theta_{CM})$. More details about the Lorentz boosts can be found in appendix A. Figure 5.1 shows the η polar angle (θ) distribution before and after this boost.

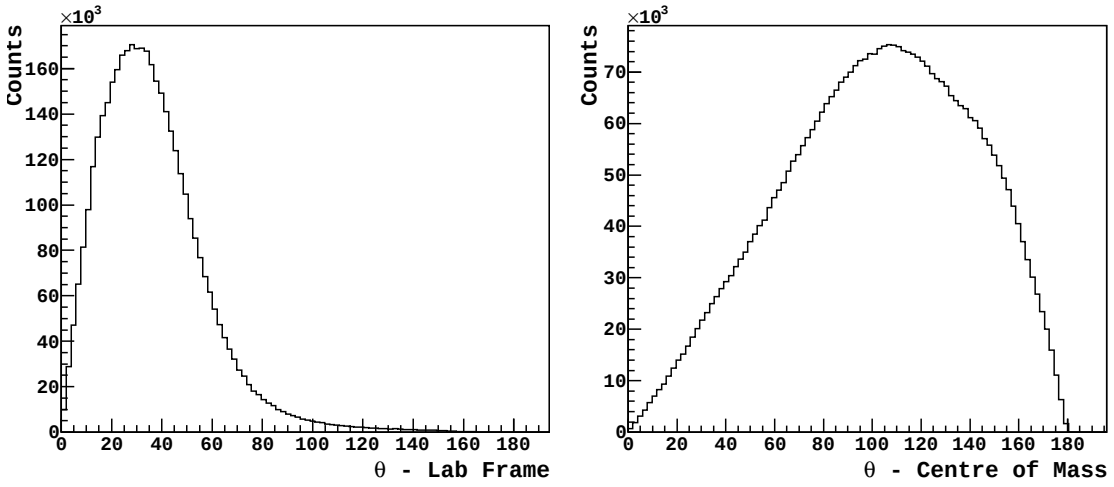

Figure 5.1: η polar angle (θ) distributions before and after Lorentz boost into centre of mass frame.

As detailed in sections 4.9 and 4.10, there is a key difference between the KC and KF methods in how the yield is extracted from the relevant missing mass histograms. The KC method requires a fit and subtraction of the background that sits under the $\gamma p \rightarrow \eta p$ peak. In the case of the KF method this type of background subtraction was not needed as the rigorous nature of the KF event selection means there exists virtually no background. There is however a small contribution remaining in the KF method from the $\gamma p \rightarrow 3\pi^0 p$ reaction. The direct $3\pi^0$ background subtraction is detailed in section 5.5.

Figure 5.2 shows the experimental η yield extracted in bins of E_γ which correspond to individual tagger focal plane detector (FPD) channels as a function of W integrated over all angular bins for both KC and KF analysis methods. The enhancement in the cross section due to the $S_{11}(1535)$ resonance is seen even in these raw yield plots. The uneven trend seen throughout the plots is not due to the effect of any resonances

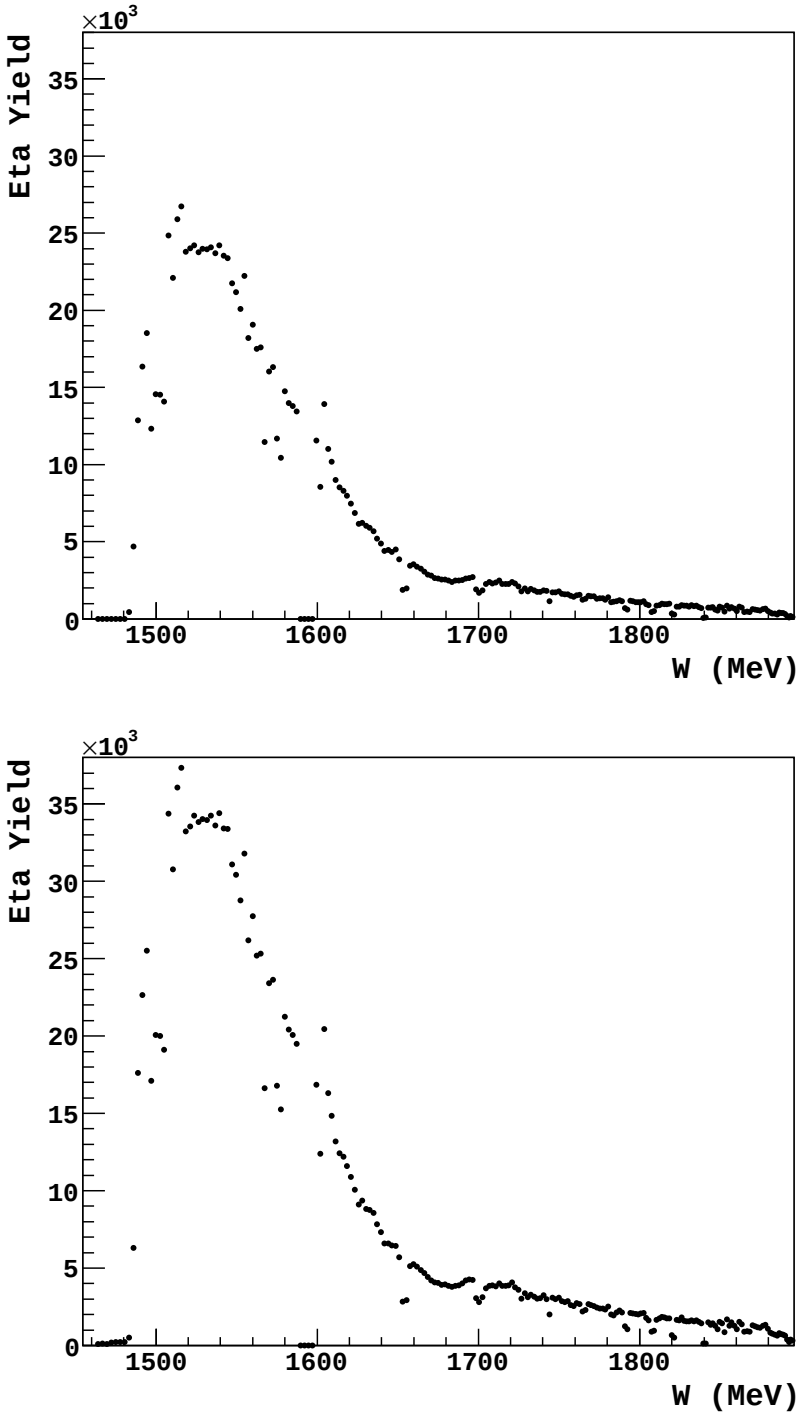

Figure 5.2: Total experimental η yield vs. W across all angles and binned in focal plane detector (FPD) channels. Top: KC method. Bottom: KF method.

but is caused by the varying counting efficiencies of the tagger scintillators. These efficiencies will be corrected in the photon flux calculations described in the following

section.

One key difference between the two plots in 5.2 is that the KF method results in a higher yield than the KC method, highlighting inefficiencies in the KC event selection technique. This is because in the KF method it is possible to consider all photon permutations before selecting the best combination of pions. This is not possible in the KC method due to the more linear nature of the pion sorting routine, where if one pion is mis-identified this will cause the event to be discarded.

In the region of interest around W = 1685 MeV/c^2, analysis of the tagger microscope data allows for a higher resolution study of the cross section. Figure 5.3 shows the η yield extracted in bins of E_γ which correspond to individual tagger microscope channels integrated over all angular bins. As in the FPD case, the uneven distribution of the raw η yield is a result of varying microscope channel efficiencies which will be corrected for.

5.3 Photon Flux

In order to calculate the cross section, the total photon beam flux must be determined. This is defined as the number of photons incident on the target over the course of the beamtime. When an electron hit is recorded in the photon tagger the scaler count for the relevant channel is increased by one. This corresponds to a photon being produced in the radiator. However, not all photons produced in the radiator will induce a reaction in the target. A proportion of beam photons are lost due to the effects of the collimator, whilst others might induce reactions which are not detected due to DAQ deadtime effects. Corrections to the raw scaler numbers as a result of these effects will be discussed in sections 5.3.1 and 5.3.2.

The raw scaler plots showing the total number of hits for both the FPD and microscope are shown in figure 5.4. The shape of the FPD spectrum exhibits the typical $\sim 1/E_\gamma$ behaviour of bremsstrahlung radiation. The low count rates in certain channels are either caused by the PMT high voltages being set too low or the discriminator thresholds being set too high. In the case of the microscope it is not possible to

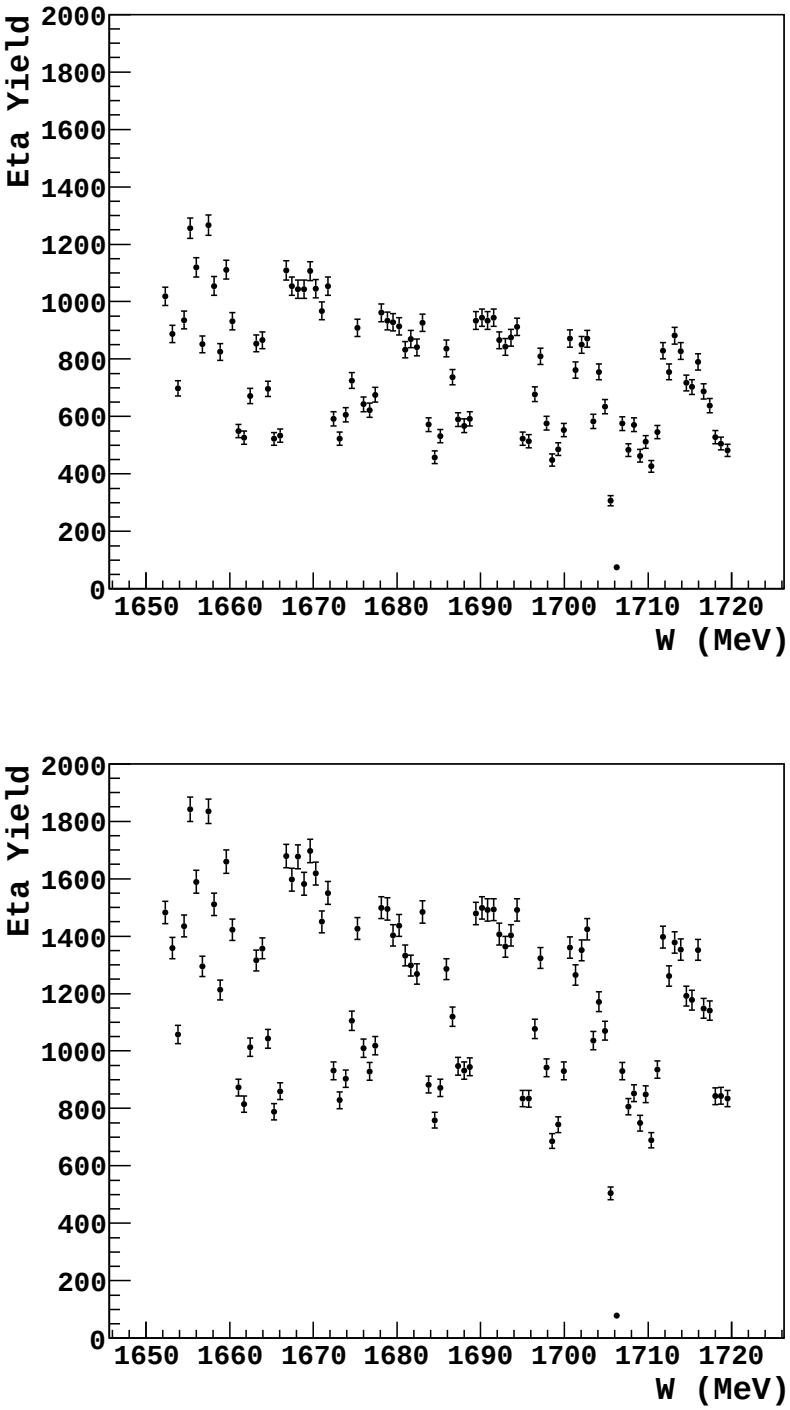

Figure 5.3: Total experimental η yield vs. W over all angles and binned in tagger microscope detector. Top, KC method. Bottom, KF method.

adjust the high voltages for each individual channel due to the use of multi-anode PMTs. The peaks and troughs observed in the scalers for both detectors are a result

of different channels having different intrinsic efficiencies. The top two sections of the tagger FPD corresponding to lower photon energies were turned off during the beamtime, which is the reason for zero scaler counts in channels 278 to 352. This allowed a higher beam current to be used in the experiment without increasing the dead time of the tagger acquisition system.

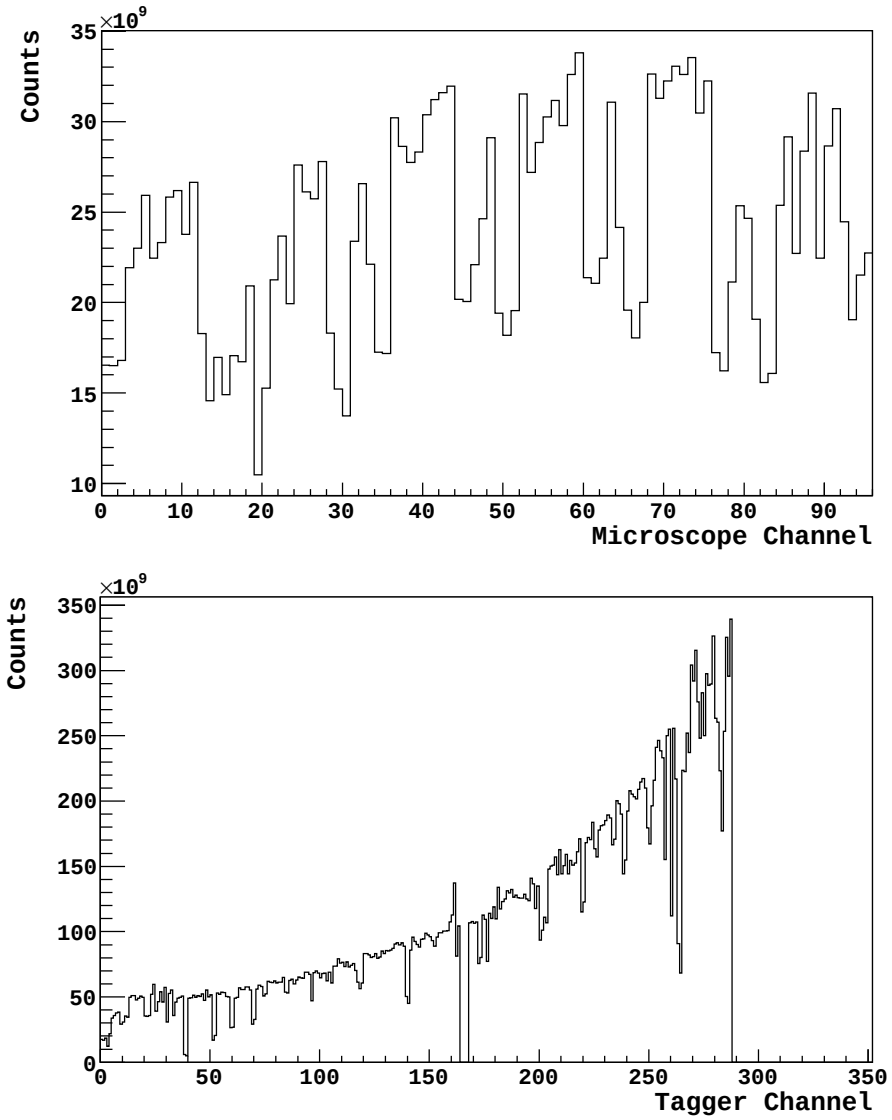

Figure 5.4: Plot showing the total scaler counts of each tagger channel for both the microscope and FPD detectors.

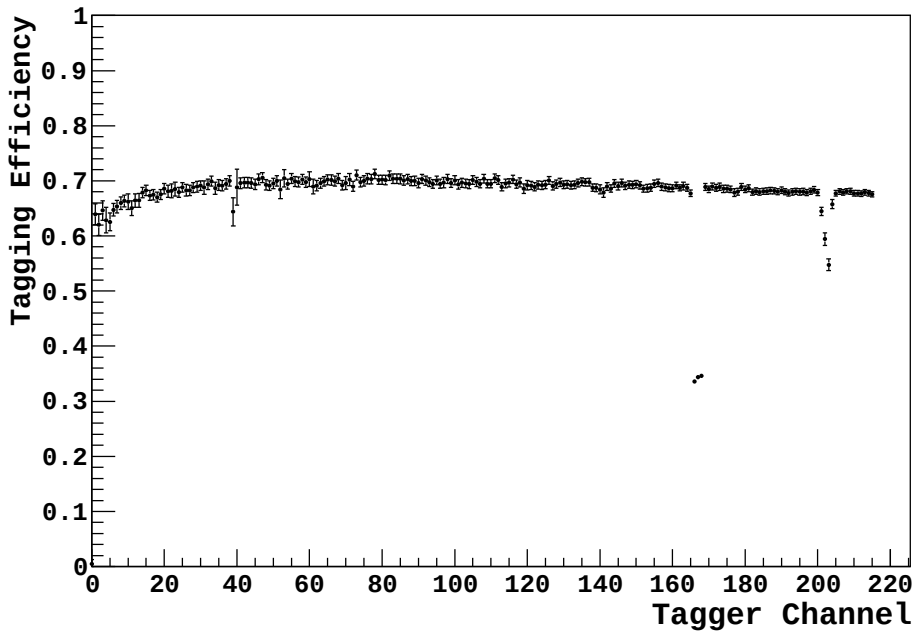

Figure 5.5: Tagging efficiency for each FPD channel.

5.3.1 Tagging Efficiency

The tagging efficiency is an important correction to the photon flux which accounts for photons being lost due to collimation of the photon beam at the exit of the tagger. It is defined as the ratio between the number of photons which pass through the collimator and the number of electron hits in the tagger TDCs. A detailed description of the technique used to determined the experimental tagging efficiency process was given in section 3.3.3. Dedicated tagging efficiency measurements were performed periodically throughout the beamtime.

A plot of the tagging efficiency for each FPD channel analysed over all tagging efficiency measurements is shown in figure 5.5. The tagging efficiency can be seen to be relatively flat, with a gradual dip at low tagger channels. An attempt was also made to measure the tagging efficiency using the microscope detector. At the low beam current needed to perform a tagging efficiency measurement the noise in the microscope detectors dominates the signal, thus the resulting tagging efficiency calculation did not produce a meaningful result. Therefore, the microscope photon

flux was corrected using the FPD tagging efficiency from the relevant tagger channel range.

5.3.2 Dead time correction

As discussed in section 3.8.6 there is a short period in which the DAQ is reading out and processing an event in which no further readout can take place. As the DAQ is effectively dead during these periods the corresponding photons which are incident on the target will not contribute to the yield and should therefore not be included in the total photon flux. Dedicated scalers are included in the DAQ in order to record the total deadtime for the CB, focal plane and microscope detectors.

The FPD hit scalers are intrinsically inhibited for the deadtime, meaning they will not count hits when the FPD DAQ is processing data. However, there is an additional effect which must be accounted for that is due to FPD hits being counted when the CB DAQ is dead. The relevant CB scalers were used to determine the percentage of FPD hits that should not be counted as a result of this CB effect, which was found to be 18%. The scalers used to record microscope hits were not intrinsically deadtime inhibited, so dedicated scalers were used to record the microscope deadtime which was found to be 42%.

5.3.3 Addition of multi-hit tagger TDCs

The CATCH TDCs that were described in section 3.8.3 to which each tagger FPD detector channel is connected are capable of recording multiple electron hits within the same event. The η yield will in principle have contributions from photons associated with the second or even third hits in these TDCs. The first electron hit in the CATCH TDC is labelled M0, the second labelled M1 and the third M2. The analysis procedures discussed in the previous chapter were performed for M0, M1 and M2 tagger data separately. It was found that the M1 tagger hits contribute an additional 8% to the total M0 yield, while the M2 hits did not contribute any additional yield. This distribution of hit multiplicities in the tagger TDCs is consistent

with expectations based on the FPD counting rates.

5.4 Acceptance Correction

By far the most complex analysis step after the yield extraction is the determination of the detector acceptance. It requires detailed models of the fundamental reaction process and the many particle interactions that contribute to hits in the detector systems. Its determination is therefore only possible with a robust software event generator and Monte Carlo simulation of the detector systems. AcquMC and the A2 Geant4 simulation that were introduced in section 4.1 were developed and refined specifically to allow for such an acceptance calculation.

Not all $\gamma p \rightarrow \eta p$ events induced in the target by the photon beam will result in the successful reconstruction of an η in the analysis software. This is due to a variety of different inefficiencies in the detector response and reconstruction software. Such inefficiencies include limits to the solid angle coverage of the detector systems, incomplete energy deposition at detector edges, cluster split-off effects in which some energy is deposited in a secondary satellite cluster and inadequacies in the clustering algorithm itself. All these effects will result in an overall detector acceptance which is less than 100%.

In order to accurately determine the cross section from the yield, target density and photon flux information, the fraction of good events lost due to acceptance effects as a function of W and $\cos(\theta_{CM})$ must be determined. In order to achieve this, $\gamma p \rightarrow \eta p$ events were generated using AcquMC to describe the phase space of the reaction, with a cross section parametrisation based on SAID model predictions (section 1.5). An iterative procedure was then performed during which these generated events were passed through the A2 simulation. The resulting simulated data were analysed using the same AcquRoot software as used for the experimental data, and parameters such as energy resolution were adjusted in order to achieve agreement with experimental distributions. Once these parameters have been tuned full analyses of the simulated data were performed using both KC and KF methods, with all cuts on kinematic

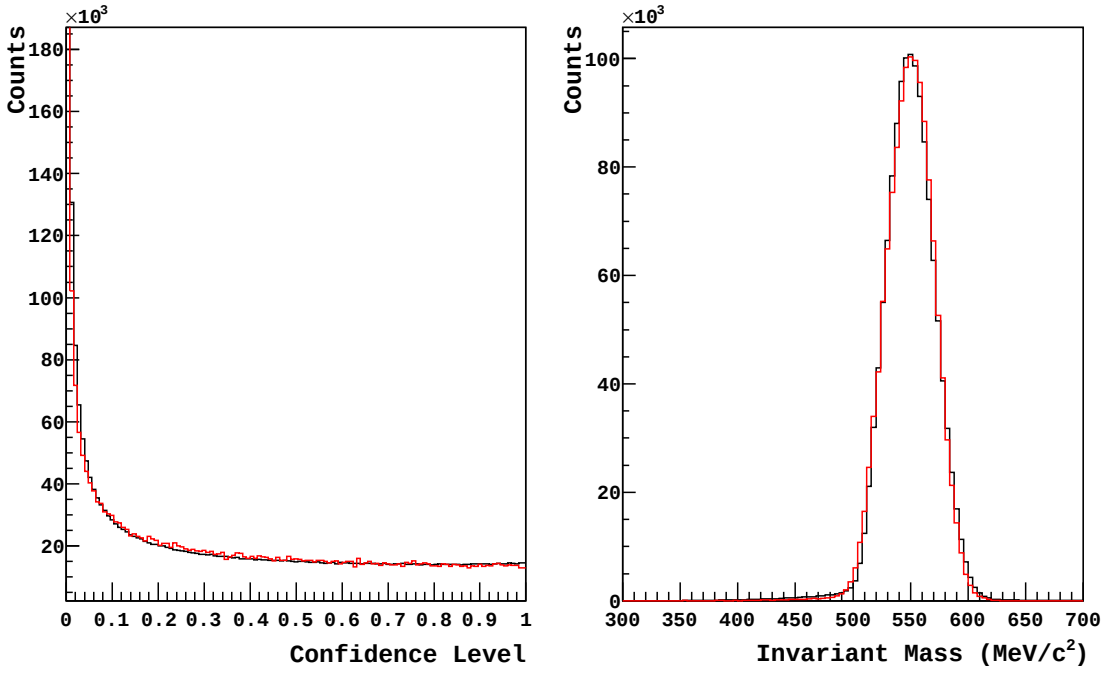

Figure 5.6: Left: confidence level of the kinematic fit. Right: invariant mass of all six photons after 2% CL cut. Experimental data is shown in black and simulated data in red.

quantities and confidence levels matched to those of the experimental data.

Comparisons between simulated and experimental data for the KF method are shown in figure 5.6. It can be seen from the plots that both the confidence level and 6γ invariant mass distributions exhibit good agreement between simulation and experiment. Figure 5.7 shows typical plots for the KC method. The widths of the 2γ and 6γ simulated invariant mass peaks match those of the experimental data thus ensuring that all cuts affect both simulated and experimental data in the same manner. Experimental background events from competing reaction channels are not reproduced in the simulated data. However, the excellent agreement in peak width demonstrated in both these figures is a sign that AcquMC and the A2 simulation allow for a rigorous and accurate understanding of the current measurement. Finally, the acceptance was determined by taking a ratio of the number of generated events and the extracted simulated yield. The acceptance as a function of W for both KC and KF methods is shown in figure 5.8. As expected from the raw yield

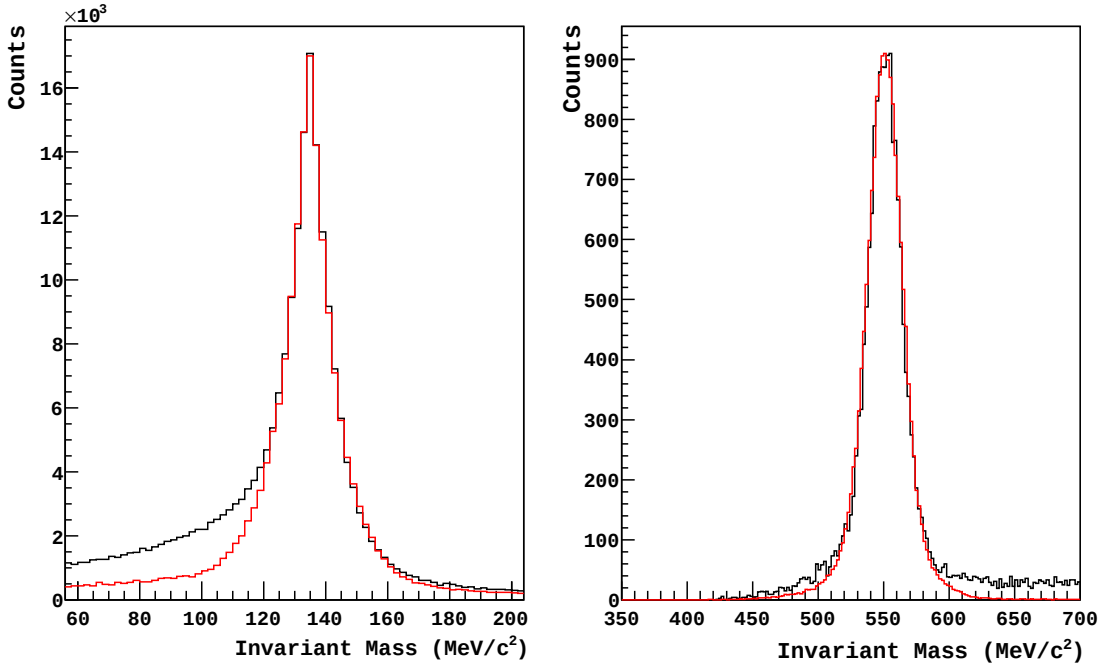

Figure 5.7: Left: invariant mass of all sorted 2γ combinations. Right: total invariant mass of all three pion events. Both plots are for the KC method, with experimental data shown in black and simulated data in red.

results in section 5.2, the KF analysis acceptance is significantly larger than for the KC method, highlighting once again that the former is a more efficient analysis technique.

5.5 Direct $3\pi^0$ Photoproduction Background Subtraction

One of the key advantages of relying on the three pion decay branch of the η is the resulting absence of significant background contributions from other photoproduction reactions. However, a potential source of background which remains is the direct photoproduction of three π^0s. Even though the phase space for both reactions is significantly different, a fraction of these direct $3\pi^0$ events will be kinematically indistinguishable from those originating from η decay. In order to determine the

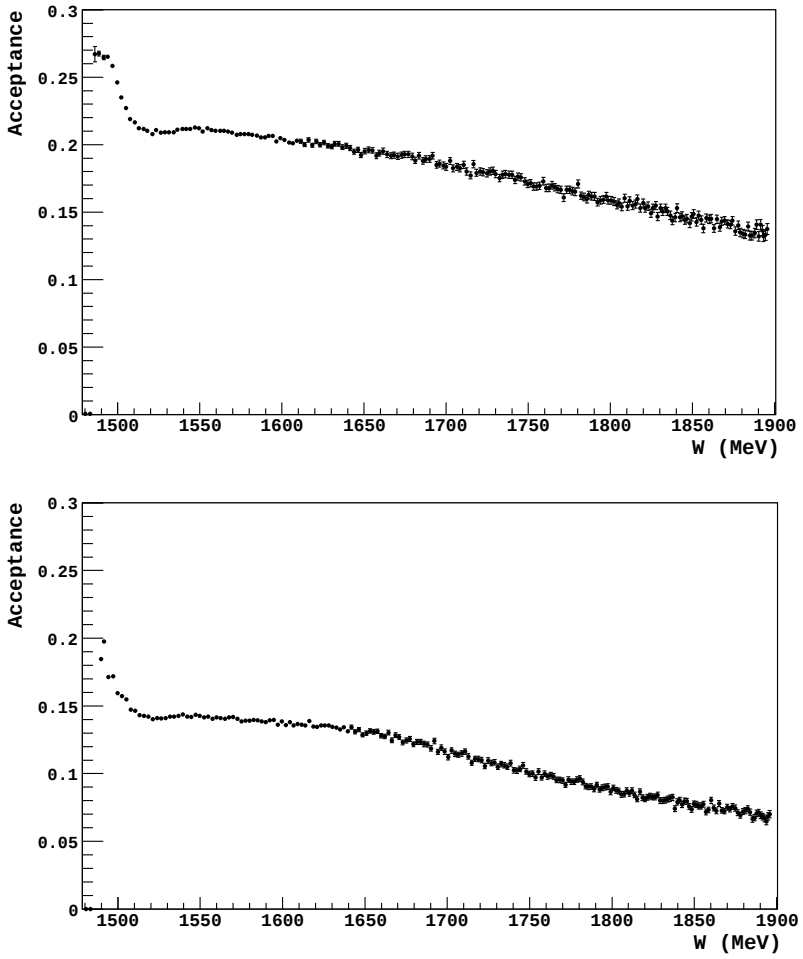

Figure 5.8: Acceptance vs. centre of mass energy. Top: KF method. Bottom: KC method.

$\gamma p \rightarrow \eta p$ cross section the number of mis-identified events must be accounted for. The only way to achieve this is by using a simulation to calculate the probability of mis-identification, combined with the known direct $3\pi^0$ cross section [86]. This is only true for the KF case because it is not possible with this technique to fit and subtract background contributions as in the KC case.

The AcquMC phase space generator was used to produce $\gamma p \rightarrow 3\pi^0 p$ events which were then passed through the A2 simulation. A KF analysis identical to that for the experimental ηp procedure was performed on these events, and the probability of mis-identification determined from the ratio of generated and accepted events after analysis. This probability as a function W is shown in figure 5.9. At the reaction threshold the probability is 27%, increases to its peak of 43% at 1520 MeV, before

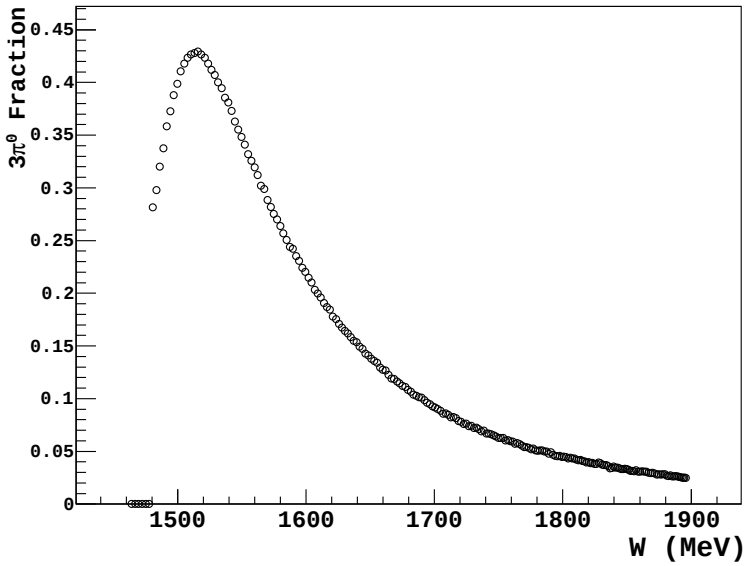

Figure 5.9: Fraction of direct $3\pi^0$ events that pass CL cuts.

decreasing to 2.5 % at 1896 MeV. Colleagues from UCLA have measured the direct $3\pi^0$ cross section using the same experimental setup as the current measurement, the result of which is shown in figure 5.10 [86]. Combing these two results gives an estimate of the direct $3\pi^0$ contribution to the measured total experimental yield, as can be seen in figure 5.11.

5.6 Empty Target Subtraction

As the entrance and exit windows of the target cell (section 3.4) are directly in the path of the photon beam, there exists a contribution to the $\gamma p \rightarrow \eta p$ yield from photoproduction reactions off protons in these windows. There can also be contributions from other target components in the beamline that are not liquid hydrogen. In order to calculate the contribution to the experimental yield as a result of these effects several runs were performed in which the target was emptied. These runs were analysed using the same techniques as the standard experimental data and the resulting η yield was normalised by the tagger scalers and the tagging efficiency. The contribution from target windows and other components as a percentage of the

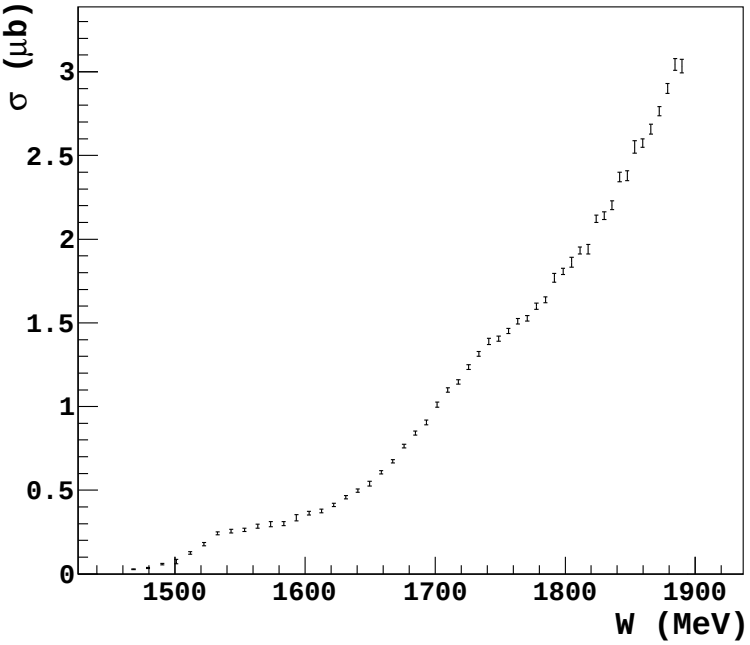

Figure 5.10: Direct $3\pi^0$ cross section [86].

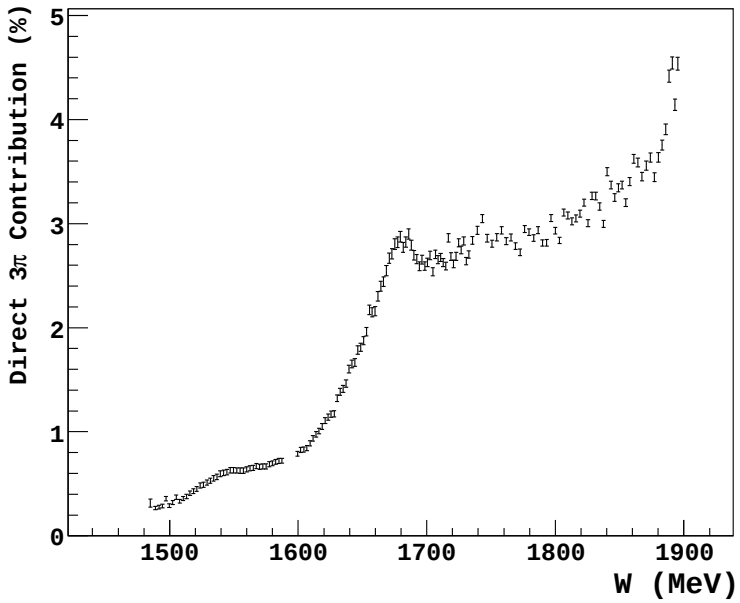

Figure 5.11: Direct $3\pi^0$ contribution as percentage of total experimental η yield vs centre of mass energy.

total measured experimental yield is shown in figure 5.12. It is clear that the KF method is much more efficient in rejecting these events than the KC method.

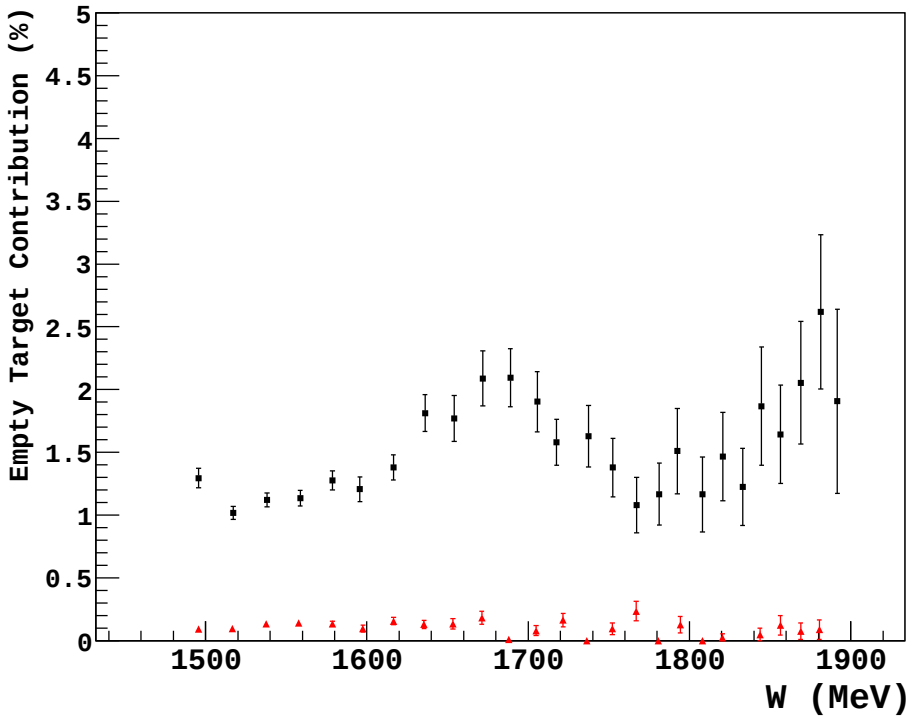

Figure 5.12: Empty target contribution as percentage of total experimental η yield vs centre of mass energy. Black points: KC method. Red points: KF method.

5.7 Legendre Polynomial Fits

The previous sections in this chapter detailed the steps necessary in order that formula 5.2 can be applied to determine the differential cross section for the $\gamma p \rightarrow \eta p$ reaction in bins of W and $\cos(\theta_{cm})$. Figure 5.13 shows a sample differential cross section result for a focal plane detector and tagger microscope energy bin. Six $\cos(\theta_{cm})$ bins were used in order to maximise the statistics in each W bin, whilst still enabling angular distributions of the differential cross section to be determined. In order to characterise these angular distributions it is possible to express the differential cross section as a sum of Legendre polynomials:

$$\frac{d\sigma}{d\Omega} = \sum_{l=0}^{\infty} A_l(W) P_l(cos(\theta)), \tag{5.4}$$

where A_l are the individual coefficients and $P_l(cos(\theta))$ the Legendre polynomials. Each differential cross section was fitted with a function including the first 5 Legendre polynomials (see table 5.1). This allowed the Legendre coefficients to be extracted for each bin, as shown by the results of the fit parameters in the inset boxes in figure 5.13. By studying the variation of these coefficients with energy it is possible to search for indications of resonant contributions. A total cross section for each energy bin can be calculated by integrating the differential cross section fit function over all angles.

l	$P_l(x)$
0	1
1	x
2	$\frac{1}{2}(3x^2 - 1)$
3	$\frac{1}{2}(5x^3 - 3x)$
4	$\frac{1}{8}(35x^4 - 30x^2 + 3)$

Table 5.1: First five Legendre polynomials.

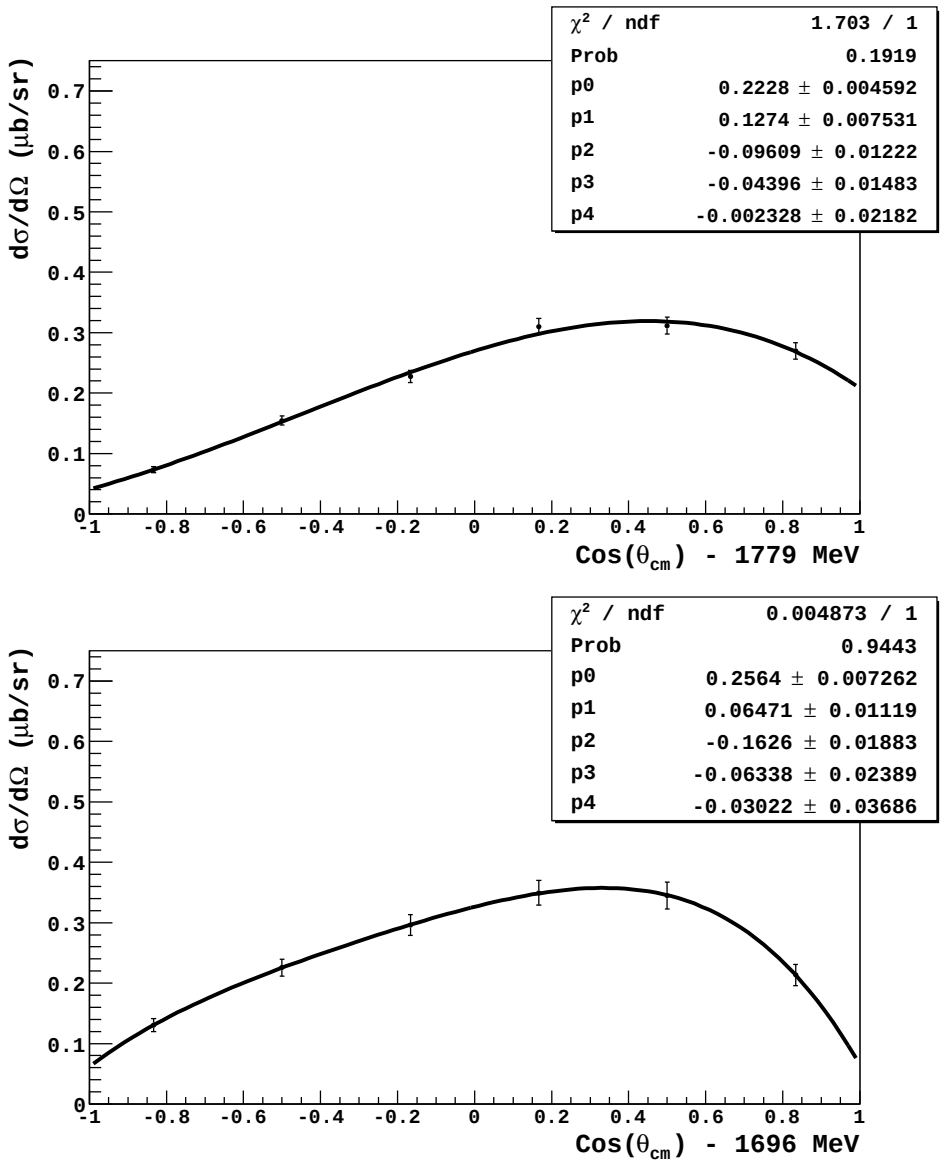

Figure 5.13: Legendre polynomial fits to differential cross sections. Top: a W bin defined by a single focal plane detector channel bin: Bottom: a W bin defined by two microscope channels. The fit function consisting of the first five Legendre polynomials has been applied. The parameters from the fit are shown in the inset box and are equal to the Legendre coefficients.

Chapter 6

Results and Discussions

This chapter presents results for the $\gamma p \rightarrow \eta p$ cross section. First, section 6.1 shows the cross section over the full available energy range using tagger focal plane detector (FPD) channel energy binning. This is presented for both Kinematic Cut (KC) and Kinematic Fit (KF) analysis methods, and SAID and MAID model predictions are compared to the results. Next, section 6.2 focuses on the energy region around 1685 MeV and in addition to the FPD energy bins, the microscope energy binning is also presented. This section also shows the total cross section in the energy range of interest for three angle regions. Section 6.3 displays the results of a more detailed study into the angular dependence of the cross section using Legendre polynomials. The systematic uncertainties associated with the KF analysis method measurement of the $\gamma p \rightarrow \eta p$ cross section is discussed in section 6.4. Finally, section 6.5 summarises the results of the measurement and discusses conclusions that can be drawn from the data.

6.1 Total Cross Section

The $\gamma p \rightarrow \eta p$ yield was determined using two different techniques for event reconstruction: the kinematic cut method and kinematic fit method. The η yield was subjected to a background subtraction in both cases, before being combined with

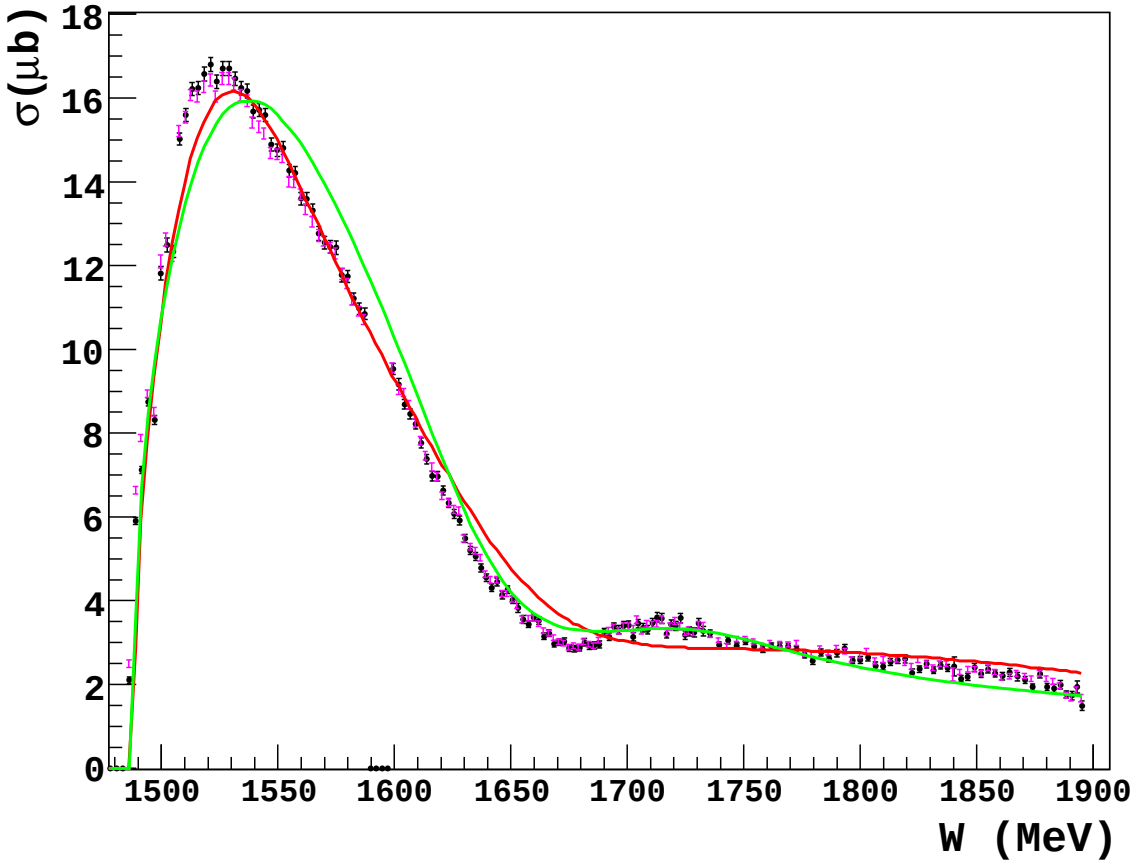

Figure 6.1: Comparison between total $\gamma p \rightarrow \eta p$ cross sections for KC (black) and KF (magenta) analysis methods. SAID (red line) and MAID (green line) model predictions are also displayed.

the acceptance of the detector systems, the corrected photon flux and target density to calculate differential cross sections in bins of centre of mass energy (W). These were then fitted with Legendre polynomials, which were subsequently integrated over the full angular range to determine the total cross section. Figure 6.1 shows the results for the total $\gamma p \rightarrow \eta p$ cross section from both the KC and KF methods as a function of centre of mass energy. Between 1486 MeV and 1732 MeV the bins correspond to one tagger focal plane detector (FPD) channel, whilst between 1735 MeV and 1896 MeV the W bins are two FPD channels wide in order to maintain a similar level of statistical precision in this region of reduced cross section. The gap in the cross section between 1590 and 1597 MeV is due to broken FPD scaler channels being removed from the analysis. There is very good agreement between the two methods, both in the overall magnitude of the cross section as well as the shape and trend. This agreement demonstrates the level of self-consistency between the two analysis methods and allows interpretation of the results with confidence. The statistical uncertainties are reduced in the case of the KF method due to the higher efficiency of the event selection, as discussed in the previous chapter.

It can be seen from the plot that the $S_{11}(1535)$ resonance dominates the cross section between threshold and 1650 MeV, and there is a clear dip in the cross section magnitude around 1675 MeV. Model predictions from SAID and MAID (see section 1.5) have been plotted with the results in figure 6.1. The SAID model is a partial wave fit of the world data-set for meson photoproduction, whilst the MAID model relies on parameters of the known 4* PDG resonances. The MAID prediction on the plot includes all the resonances available in the energy regime as well as background terms. It can be seen that around the S_{11} peak and up to approximately 1610 MeV the results are in better agreement with the SAID model. Neither model fully reproduces the dip in the cross section results at 1675 MeV, although the trend of the MAID prediction undergoes a similar oscillation around this energy.

6.2 Cross Section in the Region around 1685 MeV

The use of the tagger microscope in the region of interest around 1685 MeV allows for a higher resolution study of the total cross section. Figure 6.2 shows the microscope results for the total $\gamma p \to \eta p$ cross section section for both the KC and KF analysis methods as a function of centre of mass energy in the region around 1685 MeV. The results are binned in W so as to correspond to two tagger microscope channels, resulting in an improvement in the energy resolution over the focal plane detector by a factor of 1.5. As with the FPD results shown in the previous section, the magnitude and overall trend of the cross section results are in good agreement for the two analysis methods. It is also clear that the KF method results in better statistical precision for the microscope, leading to a smoother trend with energy particularly around the crucial 1670 to 1690 MeV region. As a result of the agreement between the analysis methods for both the FPD and microscope and the more efficient nature of the KF method, all subsequent analysis results are presented for the KF method alone.

Figure 6.3 shows a comparison of the results for the total $\gamma p \to \eta p$ cross section for the focal plane detector and microscope analyses. The trend and strength of the cross section is in good agreement for both detectors, providing a cross-check on the photon beam flux corrections which were performed separately for these detector systems.

Finally, figure 6.4 compares the results of the present measurement to previous $\gamma p \to \eta p$ cross section measurements performed on a liquid hydrogen target. There is good agreement between the data-sets, with the increased energy resolution and improved statistical precision of the present measurement clearly visible.

As previous results exhibiting an anomalous structure on the neutron channel were angle dependent, it is useful to divide the total cross section into forward, central and backwards polar angle regions. This is possible by integrating the Legendre fit functions for the differential cross sections over restricted $\cos(\theta_{cm})$ ranges. This was performed for three angular bins: forward ($\cos(\theta_{cm}) \geq 0.33$), central (-0.33 <

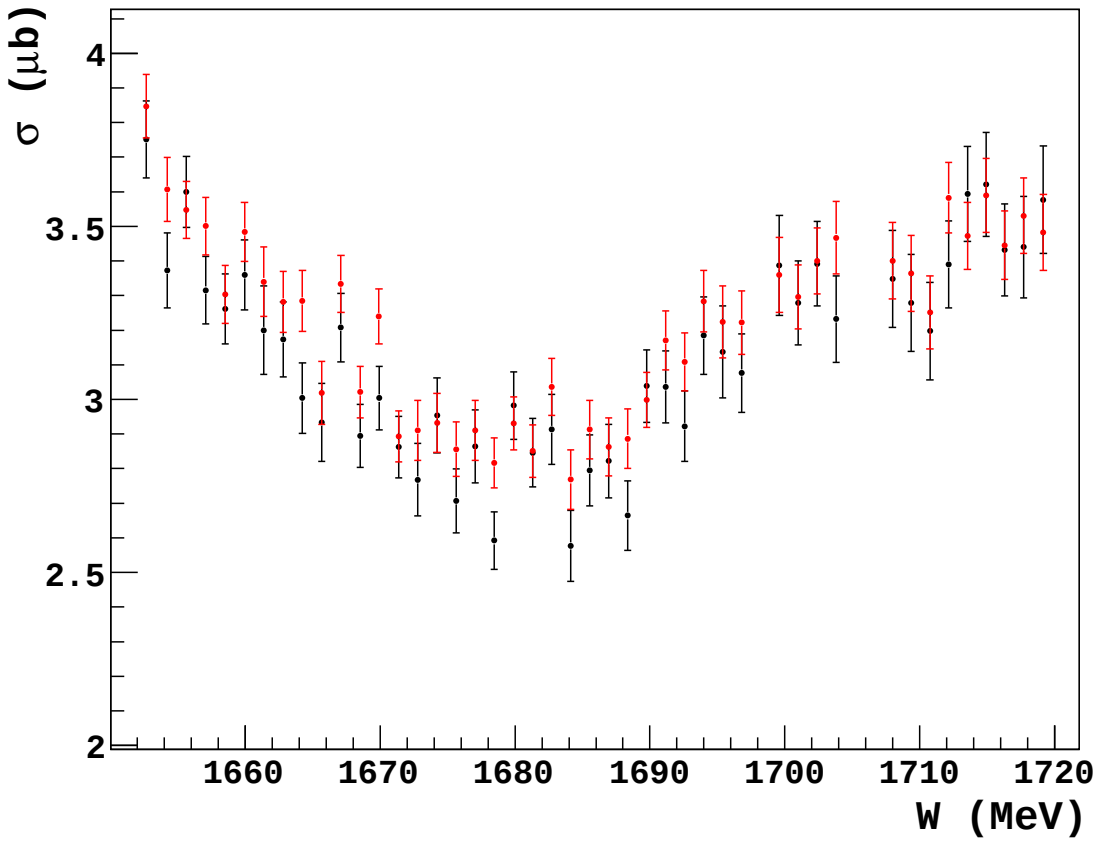

Figure 6.2: Total $\gamma p \rightarrow \eta p$ cross section binned in two tagger microscope channels as a function of centre of mass energy. Black: KC analysis method. Red: KF analysis method.

$\cos(\theta_{cm}) < 0.33$) and backward ($\cos(\theta_{cm}) \leq$ -0.33). Figure 6.5 shows the results of these calculations. It is obvious that between 1650 MeV and 1720 MeV there is a minimum followed by a maximum in the magnitude of the cross section in the forward angle region. This effect remains to a lesser extent in the central region, but is not observed at backward angles where the trend of the cross section is comparatively flat.

The corresponding MAID and SAID model predictions have again been included in the plot of results. As with the total cross section in this energy region the results show better agreement with the MAID model. In the forward angle region both model predictions describe the data reasonably well up to 1685 MeV, with

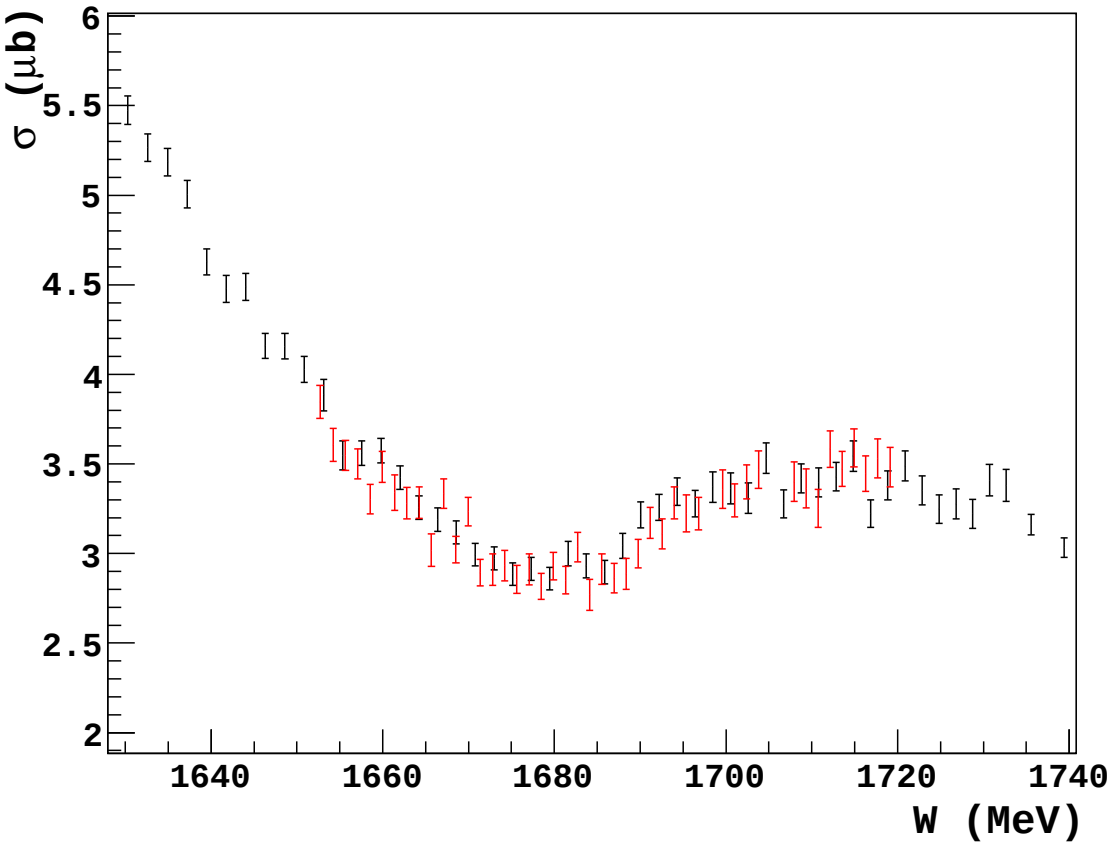

Figure 6.3: Total $\gamma p \rightarrow \eta p$ cross section as a function of centre of mass energy for both the tagger focal plane detector and microscope. Binning same as figures 6.1 and 6.2. Black points: Focal plane detector. Red points: Microscope.

the MAID prediction exhibiting a larger dip in cross section than SAID. However, at energies greater than 1685 MeV there is a discrepancy between the models and the data, with the model predictions failing to reproduce the rise in measured cross section although the trend of the MAID line does match the shape of the data if not its magnitude. In the central angle region there is agreement between MAID and the measured cross section in the energy range of 1620 to 1760 MeV. Again, the SAID line fails to replicate the oscillating trend in the data. The downward trend in the measured cross section at backward angles is smooth. This general shape is reproduced in both SAID and MAID although both predict a higher overall cross section than observed in the results.

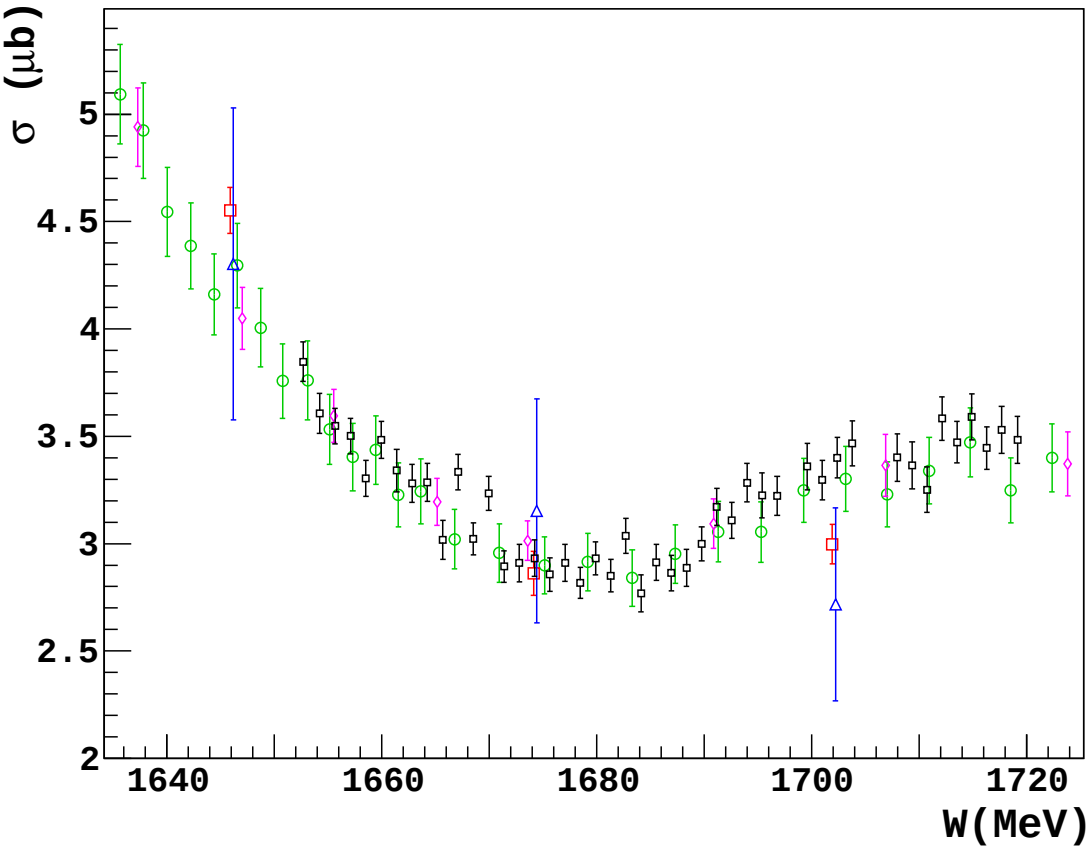

Figure 6.4: Total $\gamma p \rightarrow \eta p$ cross section binned in two tagger microscope channels as a function of centre of mass energy compared with previous results. Black squares: current measurement. Magenta diamonds: GRAAL [20]. Blue triangles: Bonn [47]. Red squares: JLab [46]. Green circles: Mainz [48].

6.3 Angular Distributions

The two of the three cross section plots shown in figure 6.5 exhibit a dip structure in the energy region of interest. The magnitude of the dip is dependent on polar angle. In order to investigate further this angular dependence it is necessary to study the differential cross sections in more detail. Figure 6.6 shows 12 differential cross sections with each plot consisting of data from two tagger microscope channels. The corresponding MAID and SAID model predictions have again been included in the result plots. The overall magnitude of the differential cross sections is lower

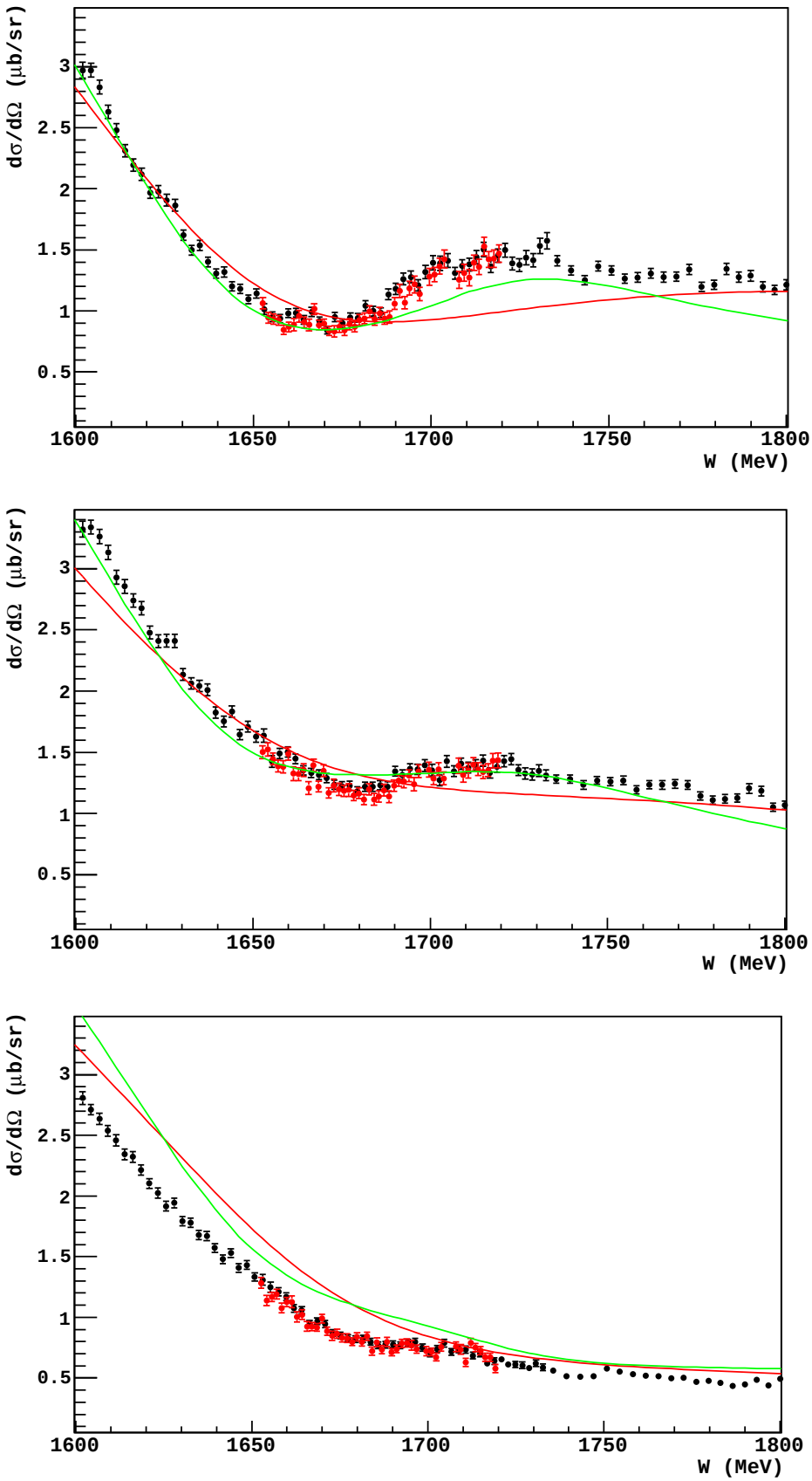

Figure 6.5: Angular cross sections for forward, central and backward regions, as defined in the text. Black points: focal plane detector. Red points: microscope detector. Red line: MAID model. Green line: SAID model.

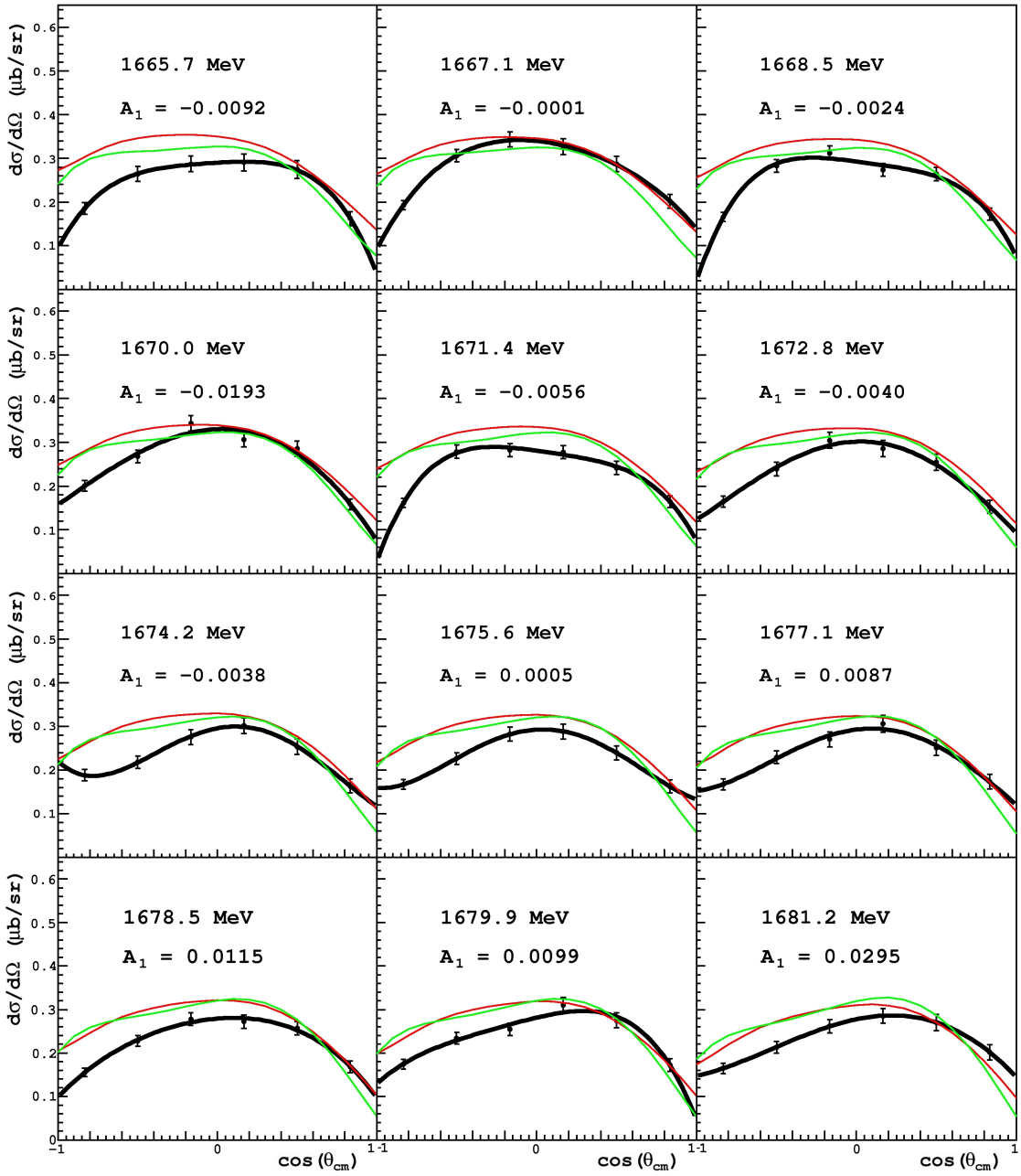

Figure 6.6: Sample of 12 differential cross sections results for the double tagger microscope detector channels. Each result is fitted with a function consisting of first five Legendre polynomials. MAID (green line) and SAID (red line) predictions are also shown.

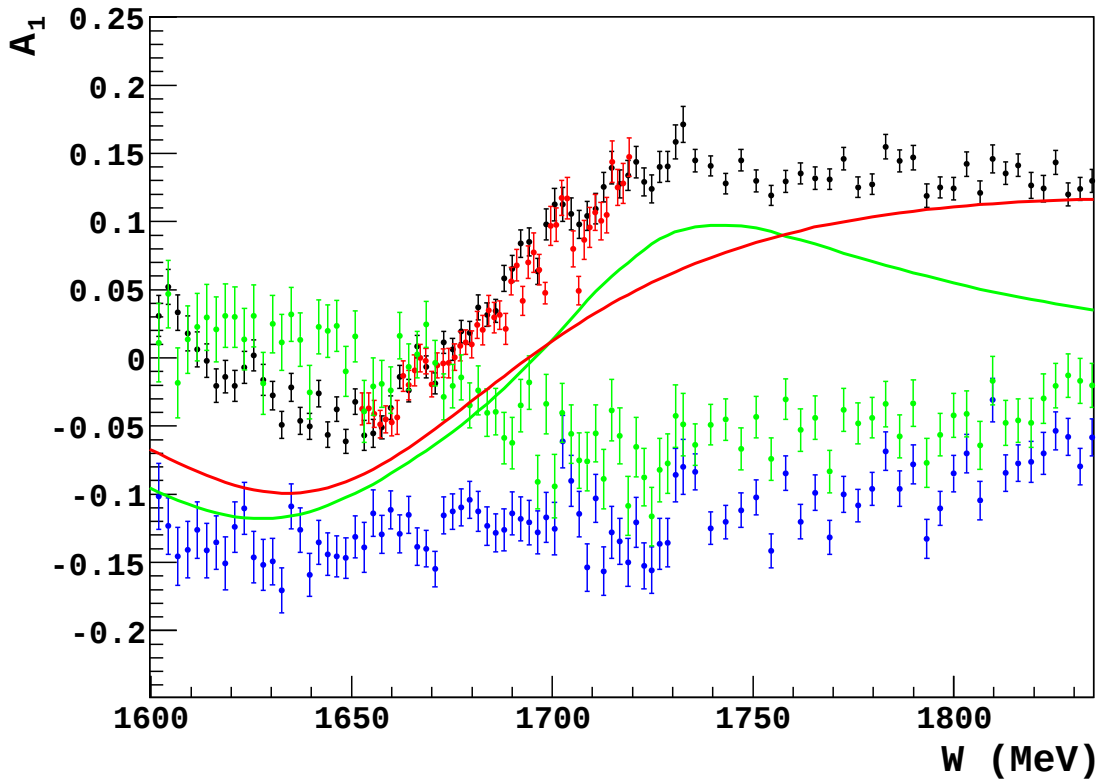

Figure 6.7: Legendre co-efficient A_1 (black FPD, red microscope), A_2 (blue) and A_3 (green) as a function of centre of mass energy. MAID (green line) and SAID (red line) predictions for A_1 are also shown.

than both SAID and MAID predictions, more so at backward angles. It is difficult to see subtle variations in the angular distributions from these plots. It is therefore more useful to examine the behaviour of the resulting Legendre coefficients from each fit.

Figure 6.7 plots the A_1, A_2 and A_3 Legendre coefficients as a function of centre of mass energy for the tagger focal plane detector, with the corresponding microscope results shown for A_1. The first Legendre coefficient A_0 is proportional to the total cross section and as such does not contain any angular information, it is therefore not of interest at this stage. As the degree of Legendre polynomial is increased the contribution of each polynomial decreases, which results in an increase in the associated error for higher coefficients. It is therefore difficult to draw any quantitative conclusions from the behaviour of A_2 and A_3. This is not true for the A_1 coefficient

which exhibits interesting behaviour in the energy range of interest. A minimum is observed at approximately 1650 MeV before A_1 increases via a sign change at 1675 MeV to a plateau at approximately 1730 MeV. The values obtained for A_1 in each of the fits in figure 6.6 have also been included. This clear sign change of A_1 occurs over the same energy region as the dip structure in the total cross section, giving an indication of resonance phenomena. The MAID and SAID model predictions for A_1 have also been included in the plot. Both model predictions exhibit a similar structure as seen in the experimental data. As with both the total cross section and the forward and central angle cross sections the MAID prediction produces a closer fit to the behaviour of the experimental data than the SAID prediction.

6.4 Systematic Uncertainties

All the components of equation 5.2 for the differential cross section will have an associated systematic error which will contribute to an overall systematic uncertainty on the results shown in the previous sections of this chapter. The two largest sources of systematic error are those associated with the acceptance calculation and the extraction of the ηp yield, which itself includes contributions from empty target and direct $3\pi^0$ events. There also exists small contributions to the overall systematic uncertainty from the errors associated with the length of the liquid hydrogen target, the decay branching ratio and the photon beam flux calculation.

The acceptance uncertainty is normally the largest error contribution in any cross section calculation, as is the case here. The reason for this sizeable uncertainty is the fact that the acceptance calculation requires the use of as detailed a simulation as possible, which will not reproduce the experiment fully. A sensible method of estimating the systematic uncertainty on the acceptance is to vary the kinematic distribution of generated events and observe how the acceptance changes. This was done by generating both a flat phase space distribution and a distribution weighted by the SAID η photoproduction cross section in AcquMC. The differences in the resulting acceptances from the A2 simulation were compared in order to calculate

the acceptance contribution to the overall systematic error on the $\gamma p \rightarrow \eta p$ cross section. This contribution ranged from 2.3% at the reaction threshold to 20% at W = 1896 MeV, with an average around the 1600 - 1800 MeV region of 4.6%.

The uncertainty in the η yield has significant contributions from the direct $3\pi^0$ and non liquid hydrogen target events. The empty target correction, shown in figure 5.12, was calculated to be on average less than 0.2%. As this is such a small effect the data was not corrected, with this correction instead included as a systematic uncertainty. The direct $3\pi^0$ correction dominates the systematic error associated with the η yield. Figure 5.11 shows that the correction is energy dependent. Several factors such as the use of a flat phase space simulation and the reliance on a cross section measurement with its own associated uncertainties make it necessary to estimate a systematic uncertainty associated with this correction. A conservative estimate as a result of these factors is 20%. This leads to a contribution to the overall systematic uncertainty for the $\gamma p \rightarrow \eta p$ cross section that ranges from 0.2% at threshold to 1% at the maximum beam energy.

Acceptance (threshold - max. beam energy)	2.3% - 20%
Acceptance (average 1600 - 1800 MeV)	4.6%
Eta Yield (threshold - max. beam energy)	0.2% - 1%
Branching Ratio	0.7%
Target Density	0.3%

Table 6.1: Systematic uncertainty contributions.

There is an error associated with the value used for the $\eta \rightarrow 3\pi^0 \rightarrow 6\gamma$ decay branch, which is taken from the error determined by the experimental measurements used to produce the branching ratio PDG values [14]. Its contribution to the overall cross section systematic error was calculated to be 0.7%. In addition, the length of the liquid hydrogen target used in the current experiment was measured to be 10.03 $\pm$ 0.03 cm [87], leading to an uncertainty in the calculation of the target area density. Its contribution to the overall systematic uncertainty was found to be 0.3%. The photon flux determination is dependent on the correction for the deadtime of the

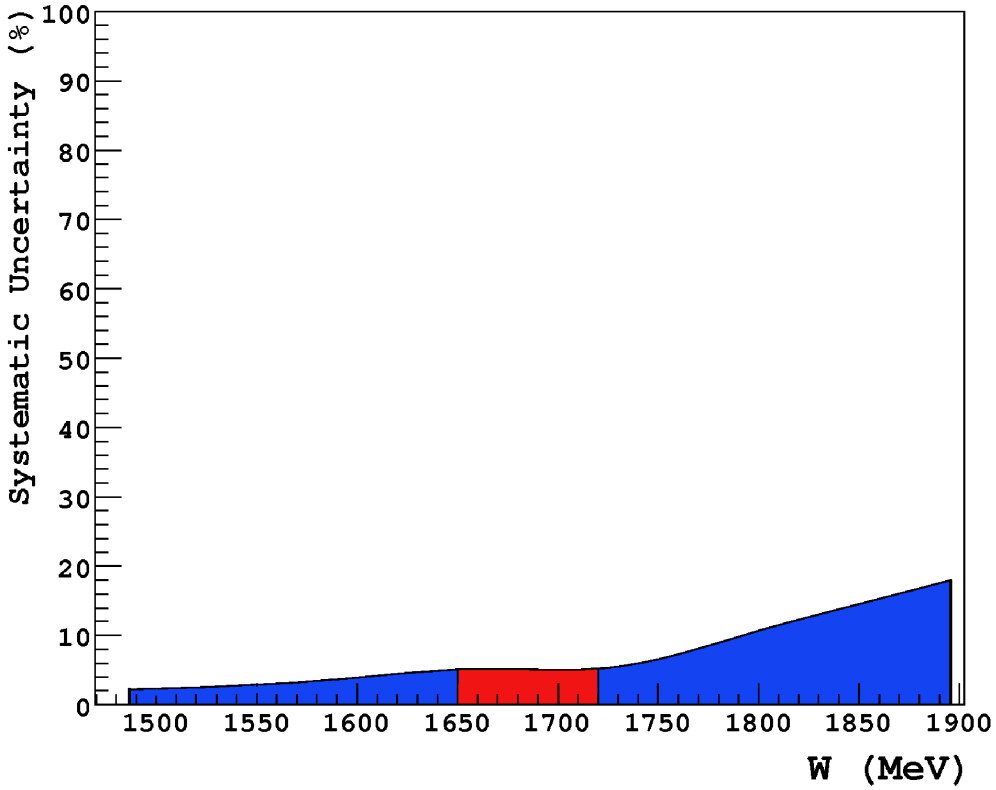

Figure 6.8: Overall systematic uncertainty for the $\gamma p \rightarrow \eta p$ cross section measurement as a function of centre of mass energy. The red shaded region represents the tagger microscope coverage.

data acquisition system. The deadtime is calculated from scalers which are known to a high precision, it is therefore assumed that the photon beam flux does not contribute significantly to the overall systematic uncertainty.

The individual contributions described above are added in quadrature to determine the final total systematic uncertainty in the $\gamma p \rightarrow \eta p$ cross section. The variation of the uncertainty as a function of W is shown in figure 6.8. The systematic uncertainty ranges from 2% at threshold to 18% at the maximum energy. The red shaded region in the figure represents the microscope detector coverage, the uncertainty for which is relatively flat with a value of 5%.

6.5 Summary and Conclusions

A high resolution, high precision measurement of the $\gamma p \rightarrow \eta p$ cross section has been performed within the A2 collaboration based at Johannes Gutenberg Universität in Mainz, Germany. This study on the proton was motivated by the controversial results from the $\gamma d \rightarrow \eta n$ measurements detailed in chapter 2. Additionally it provided the opportunity to contribute η photoproduction results to the world dataset in the centre of mass energy range of 1650 - 1720 MeV with an unprecedented energy resolution. There are several conclusions which can be drawn from the results presented in this thesis.

Given the topical nature of the present measurement, two different analysis techniques were employed in the extraction of the cross section whilst the standard tagged photon detector was supplemented by the use of the high resolution tagger microscope detector. The validity of the cross section results was confirmed by the consistency observed between both analysis techniques and both tagger photon detectors.

The results for the total $\gamma p \rightarrow \eta p$ cross section show no evidence for any anomalous peak structure around the centre of mass energy of 1685 MeV, such as was observed on the in the $\gamma d \rightarrow \eta n$ reaction. This does not preclude the existence of a possible N*(1685) resonance showing that if it were to exist, the photocoupling to the proton is such that its detection is not possible within the given precision of this measurement. In terms of the ongoing research of η photoproduction using the $\gamma d \rightarrow \eta n p$ reaction channel from deuteron targets, the high precision results of the present measurement can provide significant constraints to assist the deconvolution of the proton and neutron contributions.

The high precision, high resolution present measurement shows evidence for a minimum followed by a maximum in the magnitude of the total cross section around 1675 MeV. This structure is more pronounced than the prediction from the SAID and MAID models. A study of the cross section at different polar angles showed that this feature was more prominent at forward angles, and a more detailed study of the

cross section angular distributions was undertaken. The most significant outcome of this study was a clear change in sign in the second Legendre coefficient (A_1). This was again more pronounced than the SAID and MAID model predictions.

It should be noted that in both the total cross section and Legendre coefficient results the interesting features around 1670 MeV were broader than the width of the predictions of the N*(1685) narrow resonance. The variation in the change of sign in A_1 extends over an 80 MeV range, whereas the predictions for the N*(1685) width is < 30 MeV. The fact that the SAID and MAID models reproduce a similar trend to the current results, albeit at a reduced magnitude, suggests that these features are most likely due to interference between known resonances. The MAID model includes the following resonances located in the energy region of interest: $S_{11}(1650)$, $P_{11}(1710)$, $P_{13}(1720)$, $D_{13}(1700)$, $D_{15}(1675)$ and $F_{15}(1680)$. It should be noted that the latter three resonances are quoted as having approximately 0% η branching ratios. Within the models the contributions from each resonance should be re-evaluated in the 1650-1730 MeV energy region. These constraints from the current data will improve the models and in doing so will aid the understanding of the nucleon's resonance spectrum, thereby enhancing future meson photoproduction experiments. The results from the current experiment have proven the tagger microscope to be an excellent tool for a high resolution investigation of η photoproduction on a proton target. A possible extension to this work would be to reproduce the neutron channel cross section results of GRAAL [15], CB/ELSA [18] and LNS [19] using the tagger microscope at Mainz. This would allow the energy and width of the previously observed structure to be determined with greater accuracy.

Appendix A

Relativistic Kinematics

This appendix describes the various calculations performed on the particle Lorentz vectors in the present analysis. Natural units are employed through out this appendix ($\hbar = c = 1$).

The Lorentz vectors used are energy-momentum 4-vectors:

$$\mathbf{p} \;=\; (\; p_x,\; p_y,\; p_z,\; E\;)$$

First, photon 4-vectors are constructed using the kinematic information provided by the Crystal Ball and TAPS calorimeters. A sorting routine searches for three decay photon pairs, each of which reconstructs to a pion. Two photon 4-vectors,

$$\begin{aligned} \boldsymbol{p}_{\gamma_1} &= (\; p_{x\gamma_1},\; p_{y\gamma_1},\; p_{z\gamma_1},\; E_{\gamma_1}) \\ \boldsymbol{p}_{\gamma_2} &= (\; p_{x\gamma_2},\; p_{y\gamma_2},\; p_{z\gamma_2},\; E_{\gamma_2}) \end{aligned}$$

can be summed to form the first pion candidate 4-vector:

$$\begin{aligned} \boldsymbol{p}_{\pi_1} &= ((p_{x\gamma_1} + p_{x\gamma_2}), (p_{y\gamma_1} + p_{y\gamma_2}), (p_{z\gamma_1} + p_{z\gamma_2}), (E_{\gamma_1} + E_{\gamma_2})) \\ \boldsymbol{p}_{\pi_1} &= (p_{x\pi_1}, p_{y\pi_1}, p_{z\pi_1}, E_{\pi_1}) \end{aligned}$$

The invariant mass can be obtained by re-arranging the relativistic energy for-

mula:

$$E = \sqrt{(m_0c^2)^2 + (pc)^2} \quad \text{(A.1)}$$

$$m_0^2 = E^2 - p^2 \quad \text{(A.2)}$$

$$m_{0\pi} = \sqrt{E_{\pi_1}^2 - p_{x\pi_1}^2 - p_{y\pi_1}^2 - p_{z\pi_1}^2} \quad \text{(A.3)}$$

This is repeated for all pion candidates and the invariant mass is compared to the PDG neutral pion rest mass (135 MeV). The three most suitable combinations are selected. The three pions can then be combined to form an η candidate:

$$\begin{aligned} \boldsymbol{p}_\eta &= ((p_{x\pi_1} + p_{x\pi_2} + p_{x\pi_3}), \\ &\quad (p_{y\pi_1} + p_{y\pi_2} + p_{y\pi_3}), \\ &\quad (p_{z\pi_1} + p_{z\pi_2} + p_{z\pi_3}), \\ &\quad (E_{\pi_1} + E_{\pi_2} + E_{\pi_3})) \\ \boldsymbol{p}_\eta &= (\ p_{x\eta},\ p_{y\eta},\ p_{z\eta},\ E_\eta\ ) \end{aligned}$$

The invariant mass of this candidate η 4-vector can then be determined using formula A.2.

In order to compare the measured results to model predictions it is necessary to determine the centre-of-mass polar angle of the η. This is done via a Lorentz boost from the laboratory frame to the centre-of-mass frame. First the initial total energy and momentum of the system must be reconstructed. The kinematic information of the incoming beam photon is measured by the tagged photon spectrometer. With the direction of the beam defining the z axis, the beam photon 4-vector is given as:

$$\boldsymbol{p}_{beam} = (\ 0,\ 0,\ E_{beam},\ E_{beam}\ )$$

The target proton within the liquid hydrogen is at rest and therefore has the 4-vector:

$$\boldsymbol{p}_{prot} = (\ 0,\ 0,\ 0,\ m_{0prot}\ )$$

The total energy momentum 4-vector can then be calculated:

$$\begin{aligned} \boldsymbol{p}_t &= (\ p_{xt},\ p_{yt},\ p_{zt},\ E_t\ ) \\ \boldsymbol{p}_t &= (\ 0,\ 0,\ E_{beam},\ (m_{0prot} + E_{beam})\ ) \end{aligned}$$

To boost backwards along the z-axis the η 4-vector transforms in the following manner:

$$\begin{aligned} E'_\eta &= E_\eta\gamma - \beta\gamma p_\eta \\ p'_{x\eta} &= p_{x\eta} \\ p'_{y\eta} &= p_{y\eta} \\ p'_{z\eta} &= -\beta\gamma E_\eta + \gamma p_{z\eta} \end{aligned}$$

where

$$\beta = (\ p_t/E_t)\ ,\ \gamma = \frac{1}{\sqrt{1-\beta^2}}$$

Appendix B

Kinematic Fitting

The technique of kinematic fitting is based on the principle of χ^2 minimisation. In general the χ^2 is a measure of the difference between expected (y_e) and measured (y_m) values weighted by the uncertainty of the measurement:

$$\chi^2 \;=\; \sum_y \frac{(y_e \;-\; y_m)^2}{\sigma_y^2}$$

In a kinematic fit the expected values are defined by a series of constraint equations and the measured values are parameters defined by the kinematic information from the detector systems. The fit then adjusts (pulls) the values of the measured parameters within the limits of the uncertainties of the measurement in an attempt to match all the constraints. In the case of the present experiment the known kinematic information is defined by the photon Lorentz vectors $\boldsymbol{p}_\gamma = (\, p_{x\gamma},\, p_{y\gamma},\, p_{z\gamma},\, E_\gamma)$. Therefore each photon detected contributes four parameters to the kinematic fit.

The matrix of initial parameters, $\boldsymbol{\alpha}$, is shown below. N is defined as the total number of parameters whereas n is the total number of photons, which in the case of the current measurement is six.

$$\boldsymbol{\alpha_0} = \begin{pmatrix} \alpha_1 \\ \alpha_2 \\ \alpha_3 \\ \alpha_4 \\ \vdots \\ \vdots \\ \vdots \\ \vdots \\ \alpha_N \end{pmatrix} = \begin{pmatrix} p_{x\gamma_1} \\ p_{y\gamma_1} \\ p_{z\gamma_1} \\ E_{\gamma_1} \\ \vdots \\ p_{x\gamma_n} \\ p_{y\gamma_n} \\ p_{z\gamma_n} \\ E_{\gamma_n} \end{pmatrix}$$

Each detected photon is assigned an uncertainty as defined by the appropriate E, θ, and ϕ resolutions depending on the position and energy of the cluster hit in the calorimeter. These uncertainties are converted into Cartesian co-ordinates and calculated for each of the parameters. These are then added to the initial covariance matrix of the kinematic fit:

$$\mathbf{V_0} = \begin{pmatrix} \sigma_{11} & \sigma_{12} & \dots & \sigma_{1N} \\ \sigma_{21} & \sigma_{22} & \dots & \sigma_{2N} \\ \vdots & \vdots & \ddots & \vdots \\ \sigma_{N1} & \sigma_{N2} & \dots & \sigma_{NN} \end{pmatrix}$$

The next stage is to define the kinematic constraints which select the $\gamma p \rightarrow \eta p$ reaction channel. The present analysis uses two types of constraints, the invariant mass and the missing mass of the reaction. The constraint equation for the invariant mass of a pion is given as:

$$c(\alpha) = E^2 - p_x^2 - p_y^2 - p_z^2 - m_{\pi^0} \ = \ 0$$

In the case of an ideal measurement the difference between the measured and expected values would be zero. The partial derivatives with respect to each parameter of the constraint equation are then calculated, as shown below for the first four parameters:

$$\frac{\partial c(\alpha)}{\partial \alpha} = (-2p_{,}x - 2p_y, -2p_z, \ 2E \ )$$

The missing mass 4-vector ($\boldsymbol{p_{miss}}$) is defined as total energy momentum 4-vector ($\boldsymbol{p_t}$) subtracted by the total 4-vector of all detected photons which have been added to the kinematic fit ($\boldsymbol{p_{\gamma n}}$). The constraint equation for the reaction missing mass to equal the proton mass is given as:

$$c(\alpha) = E_t^2 - p_{xt}^2 - p_{yt}^2 - p_{zt}^2 - m_{prot} \;=\; 0$$

With the partial derivatives again defined as:

$$\frac{\partial c(\alpha)}{\partial \alpha} = (-2p_x, -2p_y, -2p_z,\ 2E\ )$$

The constraint equations are calculated using the measured parameters and each equation forms an element of the constraint matrix:

$$\boldsymbol{d_c(\alpha)} \;=\; \begin{pmatrix} c_1(\alpha) \\ \vdots \\ \vdots \\ c_m(\alpha) \end{pmatrix}$$

The partial derivatives of each constraint comprise the derivatives matrix:

$$\mathbf{D} = \begin{pmatrix} \frac{\partial c_1}{\partial \alpha_1} & \frac{\partial c_1}{\partial \alpha_2} & \cdots & \frac{\partial c_1}{\partial \alpha_N} \\ \frac{\partial c_2}{\partial \alpha_1} & \frac{\partial c_2}{\partial \alpha_2} & \cdots & \frac{\partial c_2}{\partial \alpha_N} \\ \vdots & \vdots & \ddots & \vdots \\ \frac{\partial c_m}{\partial \alpha_1} & \frac{\partial c_m}{\partial \alpha_2} & \cdots & \frac{\partial c_m}{\partial \alpha_N} \end{pmatrix}$$

Where m is the total number of constraints and N the total number of parameters.

Now the parameter, covariance, constraint and derivative matrices have been defined, the χ^2 equation can be constructed and minimised via the Lagrange multipliers technique, as described in reference [88, 89]. This results in a 1 x m matrix of Lagrange multipliers:

$$\begin{aligned} \boldsymbol{\lambda} &= (\boldsymbol{D}\ \boldsymbol{V_0}\ \boldsymbol{D}^T)^{-1}\ \boldsymbol{d_\alpha} \\ \boldsymbol{\lambda} &= \boldsymbol{V_D}\ \boldsymbol{d_\alpha} \end{aligned}$$

The new parameters which have been adjusted by the fit are defined by:

$$\boldsymbol{\alpha^f} \;=\; \boldsymbol{\alpha} \;-\; \boldsymbol{V_0}\; \boldsymbol{D}^T \boldsymbol{\lambda}$$

With the new covariance matrix defined as:

$$\boldsymbol{V^f} \;=\; \boldsymbol{V_0} \;-\; \boldsymbol{V_0}\; \boldsymbol{D}^T\; \boldsymbol{V_D}\; \boldsymbol{D}\; \boldsymbol{V_0}$$

The χ^2 of the fit is given as:

$$\chi^2 \;=\; \boldsymbol{\lambda}^T\; \boldsymbol{d_c}$$

The shape of the χ^2 distribution is defined by the number of degrees of freedom of the fit. In the case of the present analysis this is simply the number of constraints (5). The confidence level of the fit is calculated from the χ^2 and always ranges between 0-1. Events with a larger confidence level are more likely to satisfy the constraint equations.

A method of checking the validity of the fitting procedure is to examine the pull distributions for each parameter of the fit, as defined by:

$$pull_j \;=\; \frac{(\;\alpha_j \;-\; \alpha_j^f\;)}{\sqrt{\sigma_{jj} \;-\; \sigma_{jj}^f}}$$

The pulls should be normally distributed around zero with a standard deviation of approximately 1. However, if the photon uncertainties have been incorrectly calculated this will result in pull distributions which are either too wide or narrow. Additionally, if the mean of the pull distribution is non-zero this is an indication of systematic effect. Examples of the pull distributions for the current experiment are shown in figure B.1. The widths and means obtained from the Gaussian fits agree well with the expected values.

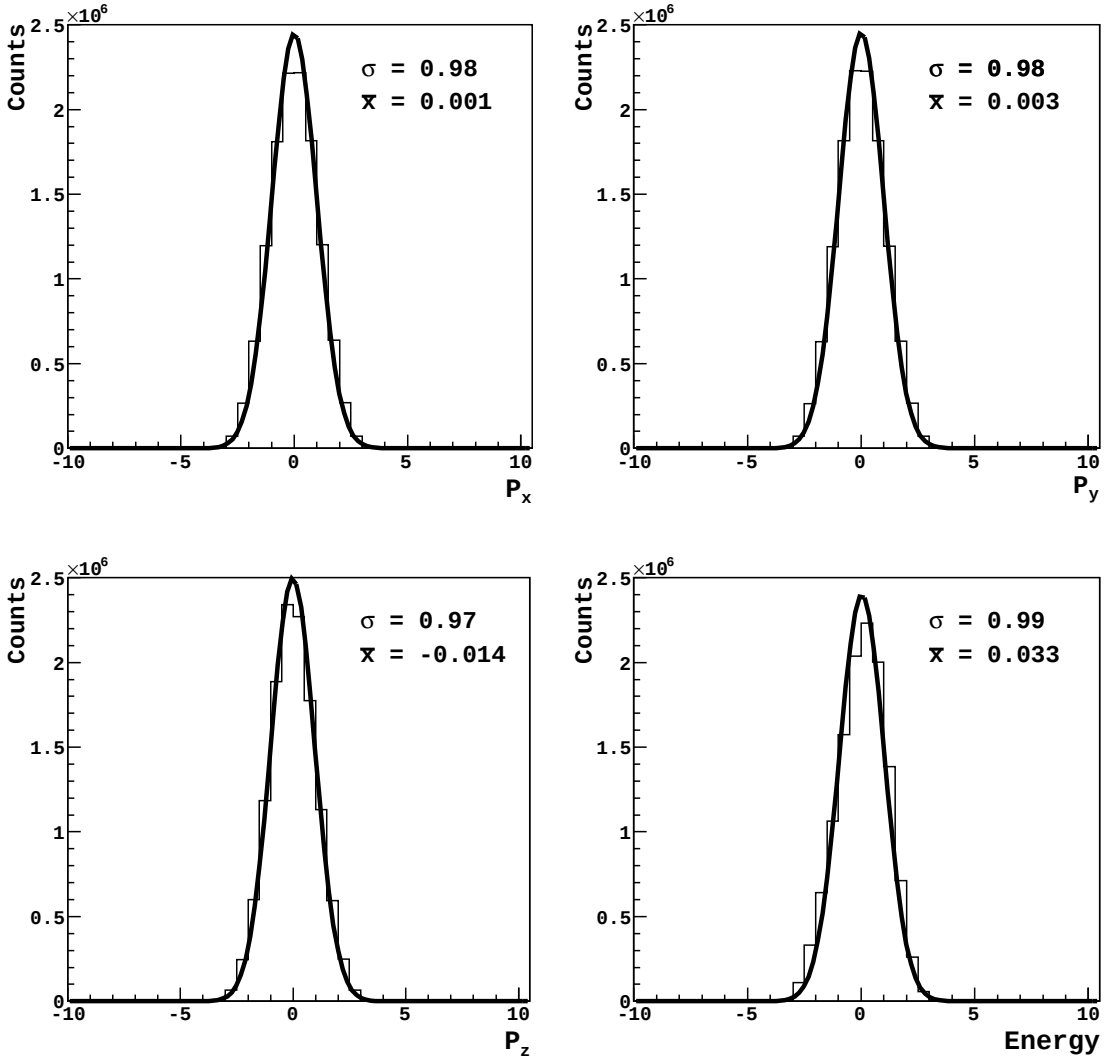

Figure B.1: Pull distributions for momentum and energy of all photons.

Appendix C

Glossary of Acronyms

ADC	-	Analogue to Digital Convertor
CB	-	Crystal Ball
CL	-	Confidence Level
ELSA	-	ELectron Stretcher Accelerator
DAQ	-	Data Acquisition System
KF	-	Kinematic Fit
KC	-	Kinematic Cut
FPD	-	Focal Plane Detector
FSI	-	Final State Interaction
GRAAL	-	GRenoble Anneau Accelerator Laser
HDSM	-	Harmonic Double Sided Microtron
LNS	-	Labratory of Nuclear Science
MAMI	-	MAinzer MIcrotron
PDG	-	Particle Data Group
PMT	-	PhotoMultiplier Tube
QCD	-	Quantum ChromoDynamics
QDC	-	Charge to Digital Convertor
RTM	-	Race Track Microtron
SAID	-	Scattering Analysis Interactive Dial-in
TAPS	-	Two/Three Arm Spectrometer
TDC	-	Time to Digital Converter

Acknowledgements

This work would not have been possible without the support of my friends, family and colleagues. I would like to thank everyone for their help, encouragement and advice over the past four years. In particular I would like to thank my supervisors Dr. David Hamilton and Dr. Douglas MacGregor, the head of group Prof. Dave Ireland as well as my fellow Mainz colleagues here in Glasgow: Ken, John, Cameron, Bob, Bryan, Eilidh, Jamie and Burger. I would also like to mention those in the A2 collaboration, in particular Derek, Dan, Tom, Mark and Pauline from the University of Edinburgh.

I wouldn't have made it to the end without friends to share a pint with and unwind at the end of the day. So to Sian, Monkey, Magnum, Burger, Moa Deep, Gary, Jen, Russell, Johan, Erin, Nicola and everyone else, thanks for all the good nights out.

Bibliography

[1] H. Yukawa. *On the Interaction of Elementary Particles. Proc. Phys.-Math. Soc. Jpn.* **17** (1935) 48.

[2] C. Lattes et al. *Processes Involving Charged Mesons. Nature* **159** (1947) 694.

[3] M. Gell-Mann and Y. Ne'eman. *The Eightfold Way.* W.A. Benjamin, 1964.

[4] V.E. Barnes et al. *Observation of a Hyperon with Strangeness Minus Three. Phys. Rev. Lett.* **12** (1964) 204.

[5] O.W Greenberg. *Spin and Unitary-Spin Independence in a Paraquark Model of Baryons and Mesons. Phys. Rev. Lett.* **13** (1964) 598.

[6] D. Politzer. *Reliable Perturbative Results for Strong Interactions? Phys. Rev. Lett.* **30** (1973) 1346.

[7] D. Gross and F. Wilczek. *Ultraviolet Behavior of Non-Abelian Gauge Theories. Phys. Rev. Lett.* **30** (1973) 1343.

[8] V. Bernard and U.-G. Meiner. *Chiral Perturbation Theory. Annu. Rev. Nucl. Part. Sci.* **53** (2007) 33.

[9] W. Roberts S. Capstick. *Quark Models of Baryon Masses and Decays. Prog. Part. Nucl. Phys.* **45** (2000) S241.

[10] W. Chiang et al. *An isobar model for η photo- and electroproduction on the nucleon. Nucl. Phys. A* **700** (2002) 429.

[11] R. A. Arndt et al. *Partial-wave analysis of pion photoproduction. Phys. Rev. C* **42** (1990) 1853.

[12] R. A. Arndt et al. *Extended partial-wave analysis of π N scattering data. Phys. Rev. C* **74** (2006) 045205.

[13] D. Drechsel et al. *A unitary isobar model for pion photo- and electroproduction on the proton up to 1 GeV. Nucl. Phys. A* **645** (1999) 145.

[14] C. Amsler et al. *Review of Particle Physics. Phys. Lett. B* **667** (2008) 1.

[15] V. Kuznetsov et al. *Evidence for a narrow structure at W = 1.68 GeV in η photoproduction off the neutron. Phys. Lett. B* **647** (2007) 23.

[16] V. Kuznetsov et al. *Evidence For A Narrow N*(1685) Resonance In η Photoproduction Off The Nucleon. Acta. Phys. Polon. B* **39** (2008) 1949.

[17] V. Kuznetsov. et al. *Evidence for a narrow N*(1685) resonance in quasifree Compton scattering on the neutron. Phys. Rev. C* **83** (2011) 022201.

[18] I. Jaegle et al. *Quasifree Photoproduction of Mesons off the Neutron. Phys. Rev. Lett.* **100** (2008) 252002.

[19] F. Miyahara. *Narrow Resonance at E_γ=1020 MeV in the D(γ,η)pn Reaction. Prog. Theor. Phys. Suppl* **168** (2007) 90.

[20] O. Bartalini et al. *Measurement of η-photoproduction on the Proton from Threshold to 1500 MeV. Eur. Phys. J. A* **33** (2007) 169.

[21] V. Kuznetsov and M. Polyakov. *Evidence for a narrow N*(1685) resonance in η photoproduction off the nucleon. Pis'ma v ZhETF.* **88** (2008)(6) 399.

[22] D. Elsner et al. *Measurement of the beam asymmetry in η-photoproduction off the proton. Eur. Phys. J. A* **33** (2007) 147.

[23] V. Shklyar, H. Lenske, and U. Mosel. *η photoproduction in the resonance energy region. Phys. Lett. B* **650** (2007) 172.

[24] T. Nakabayashi et al. *Photoproduction of η mesons off protons for $E_\gamma \leq$ 1.15 GeV. Phys. Rev. C* **74** (2006) 035202.

[25] T. H. R. Skyrme. *A unified field theory of mesons and baryons. Nucl. Phys.* **31** (1962) 556.

[26] D. Diakonov et al. *Exotic Anti-Decuplet of Baryons: Prediction from Chiral Solitons. Z. Phys. A* **359** (1997) 305.

[27] E. Witten. *Global Aspects of Current Algebra. Nucl. Phys. B* **223** (1983) 442.

[28] E. Witten. *Current Algebra, Baryons and Quark Confinement. Nucl. Phys. B* **223** (1983) 433.

[29] E. Guadagnini. *Baryons as Solitons and Mass Formulae. Nucl. Phys. B* **236** (1984) 35.

[30] D.I. Diakonov, V. Petrov, and P. Pobylitsa. *A chiral theory of nucleons. Nucl. Phys. B* **306** (1988) 809.

[31] A. Blotz et al. *The SU(3) Nambu-Jona-Lasinio soliton in the collective quantization formulation. Nucl. Phys. A* **555** (1993) 765.

[32] P. O. Mazur, M. A. Nowak, and M. Praszalowicz. *SU(3) extension of the skyrme model. Phys. Lett. B* **147** (1984) 137.

[33] S. Jain and S.R. Wadia. *Large-N baryons: Collective coordinates of the topological soliton in the SU(3) chiral model. Nucl. Phys. B* **258** (1985) 713.

[34] D. Diakonov. *Semiclassical Pion Radiation. Acta. Phys. Polon. B* **25** (1994) 17.

[35] J. P. Blaizot and G. Ripka. *Nonlinear distortions of rotating chiral solitons. Phys. Rev. D* **38** (1988) 1556.

[36] R. A. Arndt et al. *Nonstrange and other flavor partners of the exotic Z^+ baryon. Phys. Rev. C* **69** (2004) 035208.

[37] M. Polyakov and A. Rathke. *On photoexcitation of baryon antidecuplet. Eur. Phys. J. A* **18** (2003) 691.

[38] D. Diakonov and V. Petrov. *Where are the missing members of the baryon antidecuplet? Phys. Rev. D* **69** (2004) 094011.

[39] H. Kim. *Exotic and nonexotic magnetic transitions in the context of the SELEX and GRAAL experiments. Phys. Rev. D* **71** (2005).

[40] A.J.G. Hey and J. Weyers. *Quarks and the helicity structure of photoproduction amplitudes. Phys. Lett. B* **48** (1974) 69.

[41] V. D. Burkert et al. *Single quark transition model analysis of electromagnetic nucleon resonance excitations in the* $[70, 1^-]$ *supermultiplet. Phys. Rev. C* **67** (2003) 035204.

[42] A. V. Anisovich et al. *Photoproduction of η-mesons off neutrons from a deuteron target. Eur. Phys. J. A* **41** (2009) 13.

[43] X-H. Zhong and Q. Zhao. *η photoproduction on the quasi-free nucleons in the chiral quark model* (2011). ArXiv:1106.2892v2 [nucl-th].

[44] R. Shyam and O. Scholten. *Photoproduction of η mesons within a couple-channels K-matrix approach. Phys. Rev. C* **78** (2008) 065201.

[45] M. Doring and K. Nakayama. *On the cross section ratio $\sigma n/\sigma p$ in η photoproduction. Phys. Lett. B* **683** (2010)(2-3) 145.

[46] M. Dugger et al. *η Photoproduction on the Proton for Photon Energies from 0.75 to 1.95 GeV. Phys. Rev. Lett.* **89** (2002) 222002.

[47] V. Crede et al. *Photoproduction of η and η' mesons off protons. Phys. Rev. C* **80** (2009) 055202.

[48] E. McNicoll et al. *Experimental study of the $\gamma p \to \eta p$ reaction with the Crystal Ball detector at the Mainz Microtron (MAMI-C). Phys. Rev. C* **82** (2010) 035208.

[49] M. Unverzagt. *PhD Thesis* [2008]. Universitat Bonn.

[50] A. Jankowiak. *The Mainz Microtron MAMI–Past and future. Eur. Phys. J. A* **28** (2006) 149.

[51] H. Herminghaus et al. *The Design Of A Cascaded 800 MeV Normal Conducting C.W. Race Track Microtron. Nucl. Instrum. Meth.* **138** (1976) 1.

[52] K. Aulenbacher et al. *The MAMI source of polarized electrons. Nucl. Instrum. Meth. A* **391** (1997) 498.

[53] K.-H.Kaiser et al. *The 1.5 GeV harmonic double-sided microtron at Mainz University. Nucl. Instrum. Meth. A* **593** (2008) 159.

[54] A. Jankovic et al. *Design And Status Of The 1.5 GeV Harmonic Double Sided Microtron For MAMI.* In *Proceedings of EPAC*. 2002, 1085–1087.

[55] J.R.M. Annand. *The Glasgow/Mainz Bremsstrahlung Tagger Operations Manual.* Internal Report Univeristy of Glasgow (2008).

[56] I. Anthony et al. *Design of a tagged photon spectrometer for use with Mainz 840 MeV microtron. Nucl. Instrum. Meth. A* **301** (1991) 230.

[57] S.J. Hall et al. *A focal plane system for the 855 MeV tagged photon spectrometer at MAMI-B. Nucl. Instrum. Meth. A* **368** (1996) 698.

[58] J.C. McGeorge et al. *Upgrade of the Glasgow photon tagging spectrometer for Mainz MAMI-C. Eur. Phys. J. A* **37** (2008) 129.

[59] E. McNicoll. *PhD Thesis* [2009]. University of Glasgow.

[60] A. Reiter et al. *A microscope for the Glasgow photon tagging spectrometer in Mainz. Eur. Phys. J. A* **30** (2006) 461.

[61] A. Thomas. *Target Manual. Internal Report* For the A2 Collaboration.

[62] E. Bloom and C. Peck. *Physics With The Crystal Ball. Ann. Rev. Nucl. Sci.* **33** (1983) 143.

[63] M Oreglia et al. *Study of the reaction* $\psi' \rightarrow \gamma\gamma J\psi$. *Phys. Rev. D* **25** (1982) 2259.

[64] A. Starostin et al. *Measurement of* $K^- p \rightarrow \eta\Lambda$ *near threshold. Phys. Rev. C* **64** (2001) 055205.

[65] http://wwwa2.kph.uni mainz.de/cb. *Accessed 17/01/2012* .

[66] R. Novotny. *The BaF2 Photon Spectrometer TAPS. IEEE Trans. on Nucl. Sc.* **38** (1991) 379.

[67] M. Laval et al. *Barium fluoride - Inorganic scintillator for subnanosecond timing. Nucl. Instrum. Meth.* **206** (1983) 169.

[68] S. Janssen et al. *The New Charged-Particle Veto Detector for the Photon Spectrometer TAPS. IEEE Trans. on Nucl. Sc.* **47** (2000) 379.

[69] R. Beck et al. *Upgrade Of The Crystal Ball Electronics. Internal Report* (2002). For the A2 Collaboration.

[70] G. Braun et al. *TDC Chip and Readout Driver Developments for COMPASS and LHC-Experiments. Fourth Workshop on Electronics for LHC-Experiments* (1998). ArXiv:hep-ex/9810048.

[71] H. Fischer et al. *The COMPASS data acquisition system. IEEE Trans. on Nucl. Sc.* **49** (2002)(2) 443.

[72] P. Drexler et al. *The New Readout Electronics for the BaF2-Calorimeter TAPS. IEEE Trans. on Nucl. Sc.* **50** (2003) 969.

[73] J.R.M. Annand. *Data Analysis within an AcquRoot Framework.* University of Glasgow [2008]. AcquRoot Version 4v3.

[74] R. Brun and F. Rademakers. *ROOT - An Object Oriented Data Analysis Framework. Nucl. Instrum. Meth. A* **389** (1997) 81.

[75] D. Glazier. *A Geant4 simulation for the Crystal Ball@MAMI setup Internal Report.* Technical report, Univeristy of Edinburgh [2007].

[76] S. Agostinelli. *GEANT4 A simulation toolkit. Nucl. Instrum. Meth. A* **506** (2003) 250.

[77] J. C. McGeorge. *Private Communication* [2009].

[78] S. Prakhov. *Private Communication* [2009].

[79] J. Brudvik. *PhD Thesis* [2008]. University of California, Los Angeles.

[80] J. Robinson. *PhD Thesis* [2010]. University of Glasgow.

[81] P. Hall-Barrientos. *Private Communication* [2010].

[82] T. Jude. *PhD Thesis* [2010]. University of Edinburgh.

[83] H. Berghauser. *PhD Thesis* [2008]. Universität Giessen.

[84] B. Lemmer. *Diploma Thesis* [2007]. Universität Giessen.

[85] D. Glazier. *Private Communication* [2010].

[86] A. Starostin et al. *Measurement of $3\pi^0$ photoproduction on the proton from threshold to 1.4 GeV. Submitted to Phys. Rev. C* (2012).

[87] S. Prakhov. *Private Communication* [2010].

[88] P. Avery. *Fitting Theory I: General Least Squares Fitting Theory.* CLEO Collaboration internal document, CBX 91-72 [1998]. Available at http://www.phys.ufl.edu/ avery/fitting.html.

[89] P. Avery. *Applied Fitting Theory VI: Formulas for Kinematic Fitting.* CLEO Collaboration internal document, CBX 98-37 [1998]. Available at http://www.phys.ufl.edu/ avery/fitting.html.